UNIVERSIDADE FEDERAL DE MINAS GERAIS
ESCOLA DE ENGENHARIA
PROGRAMA DE PÓS-GRADUAÇÃO EM ENGENHARIA ELÉTRICA

Victor Magno Rodrigues de Jesus

Multifunctional Photovoltaic Inverters: Harmonic Current Support Effects and Operation Limits

Belo Horizonte

2023

Victor Magno Rodrigues de Jesus

Multifunctional Photovoltaic Inverters: Harmonic Current Support Effects and Operation Limits

Tese de doutorado apresentada a banca examinadora designada pelo Colegiado do Programa de Pós-Graduação em Engenharia Elétrica da Universidade Federal de Minas Gerais, como parte dos requisitos necessários para obtenção do título de Doutor em Engenharia elétrica.

Orientador: Prof. Dr Victor Flores Mendes
Coorientador: Prof. Dr Heverton Augusto Pereira

Belo Horizonte

2023

Jesus, Victor Magno Rodrigues de.
J58m Multifunctional photovoltaic inverters [recurso eletrônico] : harmonic current support effects and operation limits / Victor Magno Rodrigues de Jesus. – 2023.
1 recurso online (148 f. : il., color.) : pdf.

Orientador: Victor Flores Mendes.
Coorientador: Heverton Augusto Pereira.

Tese (doutorado) – Universidade Federal de Minas Gerais, Escola de Engenharia.

Apêndices: f. 138-148.

Bibliografia: f. 120-136.
Exigências do sistema: Adobe Acrobat Reader.

1. Engenharia elétrica – Teses. 2. Energia elétrica – Qualidade – Monitoramento – Teses. 3. Energia elétrica – Distribuição – Equipamentos e acessórios, etc. – Teses. 4. Filtros elétricos passivos – Teses. I. Mendes, Victor Flores. II. Pereira, Heverton Augusto. III. Universidade Federal de Minas Gerais. Escola de Engenharia. IV. Título.

CDU: 621.3(043)

Ficha catalográfica elaborada pelo Bibliotecário Marcio Anderson de Andrade Gomes CRB/6 2812
Biblioteca Prof. Mário Werneck, Escola de Engenharia da UFMG

UNIVERSIDADE FEDERAL DE MINAS GERAIS
ESCOLA DE ENGENHARIA
PROGRAMA DE PÓS-GRADUAÇÃO EM ENGENHARIA ELÉTRICA

FOLHA DE APROVAÇÃO

"MULTIFUNCTIONAL PHOTOVOLTAIC INVERTERS: HARMONIC CURRENT COMPENSATION EFFECTS AND OPERATION LIMITS"

VICTOR MAGNO RODRIGUES DE JESUS

Tese de Doutorado submetida à Banca Examinadora designada pelo Colegiado do Programa de Pós-Graduação em Engenharia Elétrica da Escola de Engenharia da Universidade Federal de Minas Gerais, como requisito para obtenção do grau de Doutor em Engenharia Elétrica. Aprovada em 13 de abril de 2023. Por:

Prof. Dr. Victor Flores Mendes
DEE (UFMG) - Orientador

Prof. Dr. Heverton Augusto Pereira
Universidade Federal de Viçosa - Coorientador

Prof. Dr. Danilo Iglesias Brandão
DEE (UFMG)

Prof. Dr. Thiago Ribeiro de Oliveira
DELT (UFMG)

Prof. Dr. Fernando Lessa Tofoli
Universidade Federal de São João Del Rey

Prof. Dr. Erick Matheus da Silveira Brito
Universidade Federal de Viçosa

Documento assinado eletronicamente por **Victor Flores Mendes**, **Professor do Magistério Superior**, em 13/04/2023, às 12:15, conforme horário oficial de Brasília, com fundamento no art. 5º do Decreto nº 10.543, de 13 de novembro de 2020.

Documento assinado eletronicamente por **Danilo Iglesias Brandao**, **Professor do Magistério Superior**, em 13/04/2023, às 13:11, conforme horário oficial de Brasília, com fundamento no art. 5º do Decreto nº 10.543, de 13 de novembro de 2020.

Documento assinado eletronicamente por **Fernando Lessa Tofoli**, **Usuário Externo**, em 13/04/2023, às 17:50, conforme horário oficial de Brasília, com fundamento no art. 5º do Decreto nº 10.543, de 13 de novembro de 2020.

Acknowledgements

É com grande alegria e gratidão que escrevo este texto de agradecimento para a minha tese de doutorado. Não há palavras suficientes para expressar a minha gratidão por todas as pessoas e instituições que contribuíram para a realização deste trabalho. Em primeiro lugar, quero agradecer a Deus por me dar a força e a sabedoria necessárias para concluir esta tese. A Ele, devo tudo o que sou e o que conquistei.

Aos meus pais, Sueli e Magno, e meus irmãos, Guilherme e Mylena, quero expressar minha profunda gratidão por todo o amor, apoio e incentivo que me deram ao longo de toda a minha jornada acadêmica. À Andreiva, minha esposa, que sempre esteve ao meu lado, me apoiando em todas as decisões e momentos difíceis, sem a qual não teria tomado os caminhos que tomei.

Aos meus orientadores, Victor e Heverton, que me guiaram com sabedoria, paciência e muito conhecimento, expresso minha profunda gratidão. Ao Allan, quero agradecer por todas as discussões e debates que tivemos durante o processo de pesquisa. Aos amigos do laboratório, que sempre estiveram dispostos a ajudar e a compartilhar conhecimento, sou muito grato. Vocês tornaram o trabalho mais leve e agradável.

Às instalações do LCCE-UFMG, Unifei e GESEP-UFV, que me proporcionaram todo o suporte necessário para a realização desta pesquisa, expresso minha gratidão. Por fim, quero agradecer aos membros da banca, que dedicaram seu tempo e conhecimento para avaliar meu trabalho. Agradeço por suas críticas e sugestões, que certamente contribuirão para o aprimoramento deste trabalho.

Muito obrigado.

Não há lugar para a sabedoria onde não há paciência.
(Santo Agostinho)

Resumo

As fontes renováveis têm contribuído significativamente para a nova forma de geração de energia conectada aos sistemas de distribuição e transmissão. A geração de energia distribuída por fontes renováveis tem recebido investimento crescente, especialmente a energia fotovoltaica (FV). Os inversores desempenham um papel fundamental nos sistemas de interligação à rede elétrica e sua operação multifuncional tem se tornado um foco para alcançar melhor custo-benefício. Os inversores multifuncionais são capazes de atender a diversas necessidades da rede elétrica, o que contribui para uma maior eficiência e otimização do sistema. O principal objetivo do inversor FV é injetar potência ativa na rede, mas devido às variações na irradiância solar, muitas vezes eles operam abaixo de sua corrente nominal. Essa margem de corrente pode ser usada para serviços ancilares, como suporte de potência reativa e corrente harmônica. A presente tese de doutorado tem o objetivo de investigar o impacto do suporte de correntes harmônicas (SCH) no projeto, operação e controle de sistemas FV conectados à rede. O trabalho se concentra na exploração dos efeitos dos serviços ancilares, que podem interferir no funcionamento correto dos sistemas de geração distribuída (GD). As principais contribuições desta tese incluem um algoritmo para determinar os limites do SCH, diretrizes para obter as curvas de capabilidade de tensão e corrente para inversores FV, análise do impacto de indutores não lineares nas curvas de capabilidade e recomendações para a seleção ótima de componentes do filtro LCL com base nas perdas totais do sistema e nos efeitos do SCH. A metodologia apresentada permite a avaliação de projetos de filtro passivo e tensão do barramento cc, fornecendo aos projetistas uma troca entre várias métricas de desempenho, como eficiência e volume. O trabalho demonstra que é possível alcançar um sistema FV com capabilidade aprimorada para SCH sem comprometer a eficiência do sistema. Em uma condição do estudo de caso, ao utilizar as mesmas condições de filtro passivo e frequência de comutação, a operação multifuncional resulta em uma diminuição de 0,11% na eficiência e 0,09 kW/dm^3 na densidade de potência. As descobertas e recomendações apresentadas nesta tese podem ajudar no projeto e otimização de sistemas FV conectados à rede, contribuindo, em última análise, para a integração eficiente e confiável de energia renovável na rede.

Palavras-chave: Curvas de Capabilidade; Filtros Passivos; Inversores Multifuncionais; Qualidade de Energia; Serviços Ancilares; Suporte de Correntes Harmônicas.

Abstract

Renewable energy sources have significantly contributed to the new form of power generation that is connected to distribution and transmission systems. The distributed energy generation provided by renewable sources has been receiving increased investment, particularly photovoltaic (PV) solar energy. Power inverters play a key role in these grid-tied systems and their multifunctional operation has become a focus for achieving better cost-benefit. Multifunctional inverters are capable of attend various needs of the electrical grid, which contributes to greater efficiency and system optimization. The main objective of a PV inverter is to inject active power into the ac-grid, however due to variations in solar irradiance, they often operate below their rated current. This current margin can be used for ancillary services, such as reactive power and harmonic current support (HCS). This thesis investigates the impact of HCS on the design, operation, and control of grid-tied PV systems. The work focuses on exploring the effects of ancillary services, which can interfere with the correct functioning of distributed generation (DG) systems. Key contributions of this thesis include an algorithm for determining the limits of HCS, guidelines to obtain the voltage and current capability curves for PV inverters, analysis of nonlinear inductors impact on capability curves, and recommendations for optimal LCL filter component selection based on total system losses and HCS effects. The presented methodology enables the evaluation of passive filter and dc-link voltage designs, providing designers with a trade-offs among various performance metrics, such as efficiency and volume. The work demonstrates that it is possible to achieve a PV system with enhanced capability for HCS without compromising system efficiency. In one condition of the study case, when employing the same passive filter conditions and switching frequency, the multifunctional operation results in a decrease of 0.11% in efficiency and 0.09 kW/dm^3 in power density. The findings and recommendations presented in this thesis can aid in the design and optimization of grid-tied PV systems, ultimately contributing to the efficient and reliable integration of renewable energy into the grid.

Keywords: Ancillary Services; Capability Curves; Harmonic Current Support; Multifunctional Inverters; Passive Filters; Power Quality.

List of Figures

List of Tables

List of abbreviations and acronyms

ABNT	Associação Brasileira de Normas Técnicas
ANEEL	Agência Nacional de Energia Elétrica
CEN	European Committee for Standardization
CIGRE	Congres Internationale des Grand Réseaux Électriques a Haute Tension
CPT	Conservative Power Theory
CSI	Current Source Inverter
CSPI	Cooling System Perform Index
DER	Distributed Energy Resource
DG	Distributed Generation
DFT	Discrete Fourier Transform
GSE	Generalized Steinmetz Equation
FFT	Fast Fourier Transform
HCL	Harmonic Current Limit
HCS	Harmonic Current Support
HPF	High-Pass Filter
IEC	International Electrotechnical Commission
IEEE	Institute of Electrical and Electronics Engineers
IGBT	Insulated-Gate Bipolar Transistor
iGSE	Improved Generalized Steinmetz Equation
IPT	Instantaneous Power Theory
MI	Multifunctional Inverter
MSE	Modified Steinmetz Equation
MPPT	Maximum Power Point Tracking

PCB	Printed Circuit Board
PCC	Point of Common Coupling
PF	Power Factor
PID	Proportional - Integral - Derivative
PLL	Phase-Locked Loop
PMR	Proportional Multi Resonant
PQ	Power Quality
Prodist	Procedimento de Distribuição de Energia Elétrica no Sistema Nacional
PR	Proportional Resonant
pu	Per Unit
PV	Photovoltaic
RES	Renewable Energy Source
RMS	Root-Mean-Square
SCH	Suporte de Correntes Harmônicas
SOGI	Second-Order Generalized Integrator
SVPWM	Space Vector Pulse Width Modulation
THD	Total Harmonic Distortion
VSI	Voltage Source Inverter
ZSI	Z-source inverter

List of symbols

A_e	Inductor cross-sectional area
B	Flux density
C	Dc-link capacitance
C_f	Filter capacitor
C_{min}	Minimum dc-link capacitance
C_{th}	Thermal capacitance
E_{max}	Inductor core maximum energy
$E_{on,off}$	IGBT switching on and off energies
E_{rec}	Diode recovery energy
FF	Fill factor
f_n	Nominal grid frequency
f_{min}	Minimum frequency
f_{max}	Maximum frequency
f_{sw}	Switching frequency
f_s	Sampling frequency
f_{res}	Resonance frequency
h	Harmonic order
H	Magnetic field
ΔV_{dch}	Dc-link voltage ripple
δ_{Ih}	Current phase angle of the harmonic order h
I_0	Dc-link capacitor current
I_{Sh}	Inverter synthesized current magnitude
$\hat{I}_S$	Inverter synthesized current peak value

I_b	Base current
i_a^b	Balanced active current
i_r^b	Balanced reactive current
i_a^u	Unbalance active current
i_r^r	Unbalance reactive current
i_v	Void current
i_c	IGBT collector current
i_f	Diode direct current
$I_{Sh}^{\pm}$	Current peak value for positive or negative sequence
i_{rms}	Rms current
I_{sc}	Short circuit current
I_L	Load current
I_{pv}	Photovoltaic modules current
i_s	Inverter synthesized current
$i_{s\alpha,s\beta}$	Inverter synthesized current in the stationary reference frame
$i_{sa,sb,sc}$	Inverter synthesized current in the natural reference frame
$i_{sd,sq}$	Inverter synthesized current in the synchronous reference frame
I_m	Inverter RMS peak current
K_e	Adjustable resonant control correction factor
k_p	Resonant control proportional gain
k_{ih}	Total inductance per unit
k_{pPI}	PI anti-windup proportional gain
k_{iPI}	PI anti-windup integral gain
l_e	Inductor magnetic path length
l_T	Total inductance per unit
L_{min}	Minimum inductor

L_{max}	Maximum inductor
L_f	Inverter-side inductor
L_g	Grid-side Inductor
m_i	Modulation index
N	Number of turns
n_s	Switching and fundamental frequency ratio
P_{max}	Inverter maximum power
P_{pv}	Photovoltaic modules power
P^*	Active power reference
P_Q	IGBT power loss
P_D	Diode power loss
P_{cap}	Capacitor power loss
P_{ind}	Inductor power loss
P_w	Inductor copper loss
P_c	Inductor core loss
P_v	Time-average power loss
$\bar{p}$	Oscillating active power
p	Instantaneous active power
$\tilde{p}$	Average active power
$\bar{q}$	Oscillating reactive power
q	Instantaneous reactive power
$\tilde{q}$	Oscillating reactive power
Q^*	Reactive power reference
R_f	Inverter-side inductor resistance
R_g	Grid-side inductor resistance
R_d	Damping resistor

R_{dc}	winding dc resistance
r_f	Ratio between resonance and switching frequency
r_l	Ratio between grid-side and inverter-side inductors
r_q	LCL Filter inductance and capacitance ratio
$R_{th,jc}$	Junction to case thermal resistance
$R_{th,ch}$	Case to heatsink thermal resistance
$R_{th,ha}$	Heatsink to ambient thermal resistance
S_b	Base power
$T_{vj(max)}$	Maximum junction temperature
T_a	Ambient temperature
T	Waveform period
v_g	Grid voltage
V_{dc}^*	Dc-link voltage reference
V_{pv}	Photovoltaic modules voltage
v_s^*	Inverter synthesized voltage reference
v_s	Inverter synthesized voltage
v_g	Instantaneous grid voltage
V_g	RMS line-to-line grid voltage
V_c	Capacitor voltage
V_{pcc}	Point of common coupling voltage
$v_{s\alpha,s\beta}$	Inverter synthesized voltage in stationary reference frame
$v_{sa,sb,sc}$	Inverter synthesized voltage in natural reference frame
$v_{sd,sq}$	Inverter synthesized voltage in synchronous reference frame
V_{cap}	Capacitors volume
V_{ind}	Inductors volume
V_{CS}	Cooling system volume

v_f	Diode direct voltage
v_{ce}	IGBT emitter collector voltage
V_{PCCh}	Point of common coupling voltage for the harmonic order h
$\hat{V}_S$	Inverter synthesized peak voltage
V_{dc_est}	Estimated dc-link voltage value
V_b	Base voltage
Z_{LCL}	Filter impedance
Z_th	Transient Thermal Impedance
δ_{Vh}	Voltage Phase Angle of the Harmonic order h
ΔV_{dch}	Dc-link voltage ripple
ΔT_i	Inductor temperature rise
$\Delta_{I,max}$	Current ripple
ω_f	Angular fundamental frequency
δ_p	Depth of Penetration
τ_i	Thermal time constant

Contents

1 Introduction

1.1 Context and relevance

Power quality (PQ) has been an important topic within the power system, as it impacts system loads such as motors, transformers, cables, etc. PQ problems can cause technical issues such as excess heating, false tripping, early aging of devices, and equipment malfunction (LUMBRERAS et al., 2020). Ideally, the power system should supply safe, reliable, and uninterrupted energy that is purely sinusoidal in terms of magnitude and frequency according to the terms of the energy supplier contract. PQ problems are quantified in terms of supply system voltage, current or frequency deviation, which may cause equipment malfunction in industrial, commercial, and end-consumer settings (IEEE, 2014). Due to the increased use of electronic devices and nonlinear and unbalanced loads, PQ problems have been exacerbated, which may compromise the operation and stability of the power system (SALEM et al., 2022).

Regulatory improvements for PQ are constantly being discussed. A technical regulation refers to a document approved by government agencies that includes mandatory administrative regulations. In Brazil, PQ regulation established by ANEEL (Agência Nacional de Energia Elétrica) is contained in Module 8 of the Procedimentos de Distribuição de Energia Elétrica no Sistema Elétrico Nacional - Prodist. Other standards include: IEC 61000 - IEC (International Electrotechnical Commission); CIGRE C4.07/CIRED - Cigré (Congres Internationale des Grand Réseaux Électriques a Haute Tension); and EN 50160 - CEN (European Committee for Standardization). Fig. 1 presents common PQ problems addressed in the standards above, highlighting the main causes and effects.

In the current power system scenario, interest in renewable energy sources (RESs) and its integration with the power grid have grown significantly as a result of increasing power demand, environmental problems, and governmental policies (RAY; RAY; DASH, 2022).

Distributed energy resources (DREs) consist of several components, including the energy source, energy storage, power management and inverter. The inverter is utilized to match the voltage and frequency conditions of the electricity generated by the RES with those required by the final consumer. However, a high penetration of inverters in the electrical grid can lead to PQ issues in electrical systems. Harmonic distortion on power lines is one of the most significant contributors to poor PQ.

Maintaining PQ within the limits imposed by regulations is not only the responsibility of consumers, but also that of energy suppliers and manufacturers of electrical and electronic equipment. In general, energy utilities must maintain voltage quality at the point of common coupling (PCC) (ANEEL, 2011; IEEE, 2014), while manufacturers must design equipment that

Source: Own authorship.

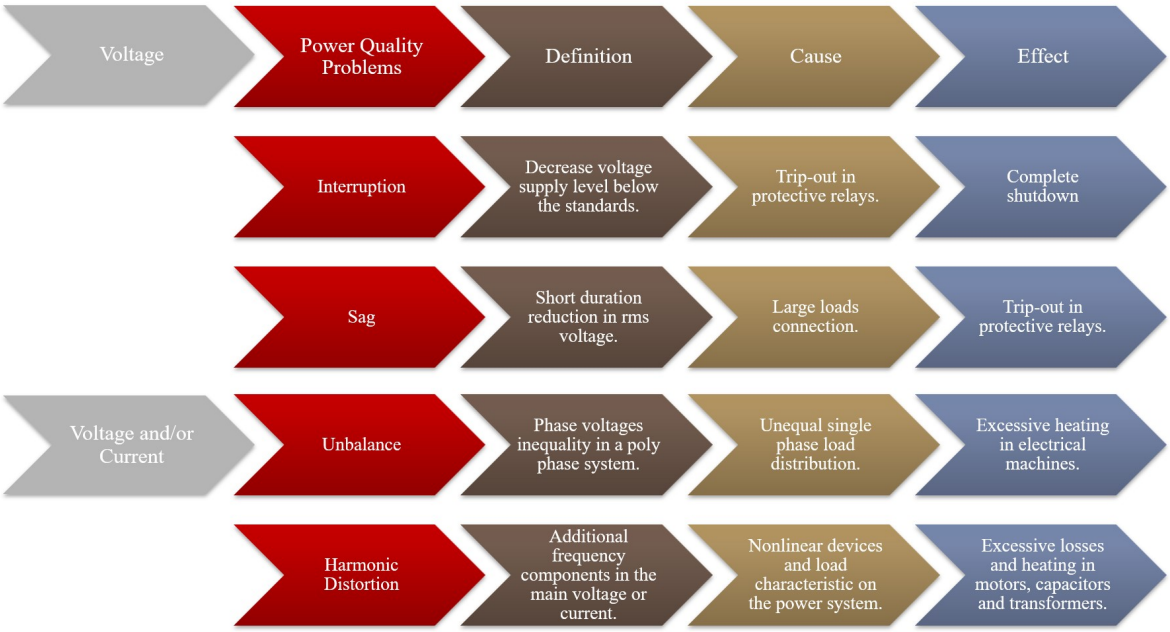

Figure 1 – PQ problems cause and effect examples.

does not degrade PQ beyond the standards limits (IEC, 2014).

In summary, IEEE 519-2014 states that the power distribution company must be able to provide voltage with defined power quality characteristics. However, to ensure a grid-oriented PQ for their installations, end-consumers must also fulfill certain requirements. Tables 1 and 2 present the recommended harmonic voltage limits and the maximum current distortion according to IEEE (2014), respectively.

Table 1 – Voltage distortion limits.

Bus voltage V	Individual harmonic (%)	Total Harmonic distortion (%)
$V \leq 1.0$ kV	5	8.0
1 kV $< V \leq 69.0$ kV	3	5.0
69.0 kV $< V \leq 161.0$ kV	1.5	2.5
161 kV $< V$	1.0	1.5

Source: IEEE (2014).

Note in Table 2 that the short-circuit current (I_{sc}) is taken into account alongside the load current (I_L). The two values are compared as a ratio I_{sc}/I_L, which provides some insight into the electrical source impedance and the ability to handle harmonics. The greater the difference between I_{sc} and I_L, less likely the circuit will be affected by the presence of harmonics. Additionally, only odd harmonic orders are presented in the table; even harmonics are limited to 25%

Table 2 – Current distortion limits for systems rated 120 V through 69 kV.

Maximum harmonic current distortion. (% of maximum demand load)					
	Individual harmonic order (odd harmonics)				
I_{SC}/I_L	$3 \leq h < 11$	$11 \leq h < 17$	$17 \leq h < 23$	$23 \leq h < 35$	TDD
< 20	4.0	2.0	1.5	0.6	5.0
$20 < 50$	7.0	3.5	2.5	1.0	8.0
$50 < 100$	10.0	4.5	4.0	1.5	12.0
$100 < 1000$	12.0	5.5	5.0	2.0	15.0
> 1000	15.0	7.0	6.0	2.5	20.0

Source: IEEE (2014).

of the odd harmonic limits presented.

When the distortion on the PCC exceeds the limits imposed, consumers must adopt corrective measures. Otherwise, it can affect the grid at the transmission and distribution levels (LI; WANG; XU, 2019; IEEE, 2021). In the literature, it is possible to find a great diversity of filters and devices for harmonic current mitigation.

Harmonic mitigation technologies for power systems can be broadly divided into two categories: passive and active techniques. Passive techniques include the use of passive filters, which are composed of capacitors, inductors and/or resistors connected in parallel with the harmonic load, tuned to specific frequencies to provide low-impedance paths and prevent harmonic currents from flowing out of the load (GONZALEZ; MCCALL, 1987). The main advantage of passive filters is their low cost and almost maintenance-free service, but they can have limitations such as dependence on system conditions and the need for elaborate investigations into harmonic resonance and overloading (DAS, 2004).

Active techniques include the use of active filters, which have a higher filtering performance capability, smaller size, and more adjustable operation compared to passive filters (AKAGI, 2006). They consist of a voltage-source inverter equipped with a dc-link capacitor. Active filters have higher cost of installation and maintenance, but they can overcome some of the limitations of passive filters. Hybrid filters, which combine active and passive components, are also used to reduce the inverter rated power and allow high power applications with reduced costs (ANTUNES; PIRES; SILVA, 2019).

Nowadays, there is a growing emphasis on devices that can perform a variety of different functions using the same hardware configuration. This is commonly referred to as multifunctional operation (RAY; RAY; DASH, 2022). The reason for this shift in focus is the increasing demand for devices that are more versatile and efficient. Fig. 2 presents the main ancillary services that have been extensively discussed and documented in various academic literature sources. These services play a crucial role in supporting the reliable and efficient operation of power systems

and maintaining their stability.

Source: Own authorship.

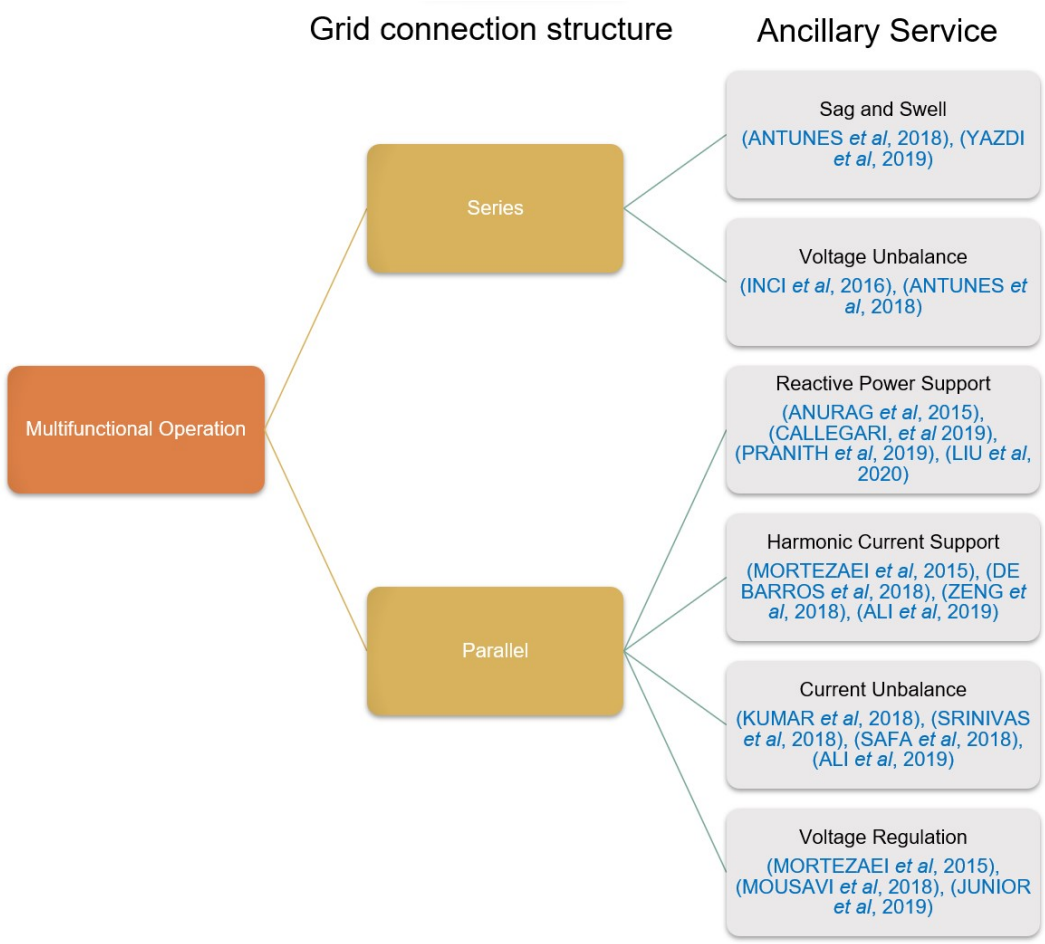

Figure 2 – Ancillary services in distributed generation units

Although there are regulations that set limits on harmonic distortion in the power system, currently, there is no requirement for inverters connected to the grid to mitigate harmonic currents and voltage at the PCC. Due to the increasing adoption of RES such as photovoltaics (PV) solar energy, could lead to a future scenario where regulatory agencies require distributed generation (DG) systems connected to the grid to contribute to harmonic mitigation.

In Brazil, Art. 23o da Lei nº 14.300, de 06 de janeiro de 2022 (BRASIL, 2022) already permits the contract of ancillary services with the objective of improving efficiency and capacity, as well as deferring investments by the power distribution company. Although it does not explicitly mention harmonic mitigation, it provides an opportunity for addressing such issues, as distortions can adversely affect the electrical system. Also, regulatory agencies have already established requirements for addressing other grid-related issues, such as reactive power injection. These regulations vary by region, but they demonstrate a trend towards assigning specific responsibilities to grid-connected inverters. In the United States, IEEE 1547 requires at least 20% of rated power, in Europe IEC 62116 requires -0.2 to +0.8 pu, and in Brazil ANEEL's Normative

Resolution complies with the requirements of the IEC standard. These requirements are put in place to support the grid in terms of stability and voltage regulation. Drawing parallels to these existing regulations, it is reasonable to expect that similar measures may be implemented for harmonic mitigation in the future.

These indicators demonstrate the growing importance of addressing harmonic distortion in power systems and the need for inverters to play a role in mitigating these harmonics. Alternatively, DG systems could be designed with harmonic mitigation services to assist or replace existing technologies such as passive and active filters. Therefore, as motivators of this thesis are to continue advancing research in this specific area and help fill the current knowledge gaps that exist. It is important to take steps that will lead to a deeper understanding of the effects of ancillary services in the PV systems. The current study is within the context of multifunctional operation, with a specific focus on PV inverters providing harmonic current support (HCS).

1.2 Multifunctional PV inverter realization

Among the promising RESs, PV solar energy has been increasing rapidly, mainly due to the abundance of energy that reaches the surface of the earth and the cost-effective residential installation. The stochastic nature of solar irradiance can be seen as an opportunity to optimize the use of PV inverters (SHAFIULLAH; AHMED; AL-SULAIMAN, 2022). It is possible to use inverters in the PV systems, whose main function is to inject active power into the grid, for PQ improvement(ALONSO, A. M. d. S. et al., 2020; RAY; RAY; DASH, 2022). These are called multifunctional inverters (MI).

PV grid-connected inverters and shunt active power filters share some similarities regarding its power structure and control techniques (ALONSO, A. M. et al., 2021). Fig. 3 shows the basic structure and generic control techniques of distributed generators and active power filters. Also, both are viewed by the power grid as a controlled current source and must be synchronized with the power grid. However, despite technical similarities, additional control and/or hardware improvements may be necessary in the PV system (CALLEGARI; SILVA, et al., 2019; SHAFIULLAH; AHMED; AL-SULAIMAN, 2022).

In MI, it is possible to implement ancillary services beyond basic energy conversion that can provide support to the electrical grid. PV inverters can provide several ancillary services, including: Harmonic support, reactive support, frequency regulation, voltage regulation and ride-through capability (SHAFIULLAH; AHMED; AL-SULAIMAN, 2022). Reference Munir and Li (2013) explores using residential DG-grid interfacing inverters as virtual harmonic resistances to mitigate the harmonics and improve PQ in a typical residence. Authors in Bighash et al. (2018) also described a strategy for compensating harmonics in the residential distribution grid using grid-connected roof-top PV inverters. The compensation method is based on analyzing the PCC voltage harmonics and using an adaptive-harmonic compensator to individually compensate each

Source: Own authorship.

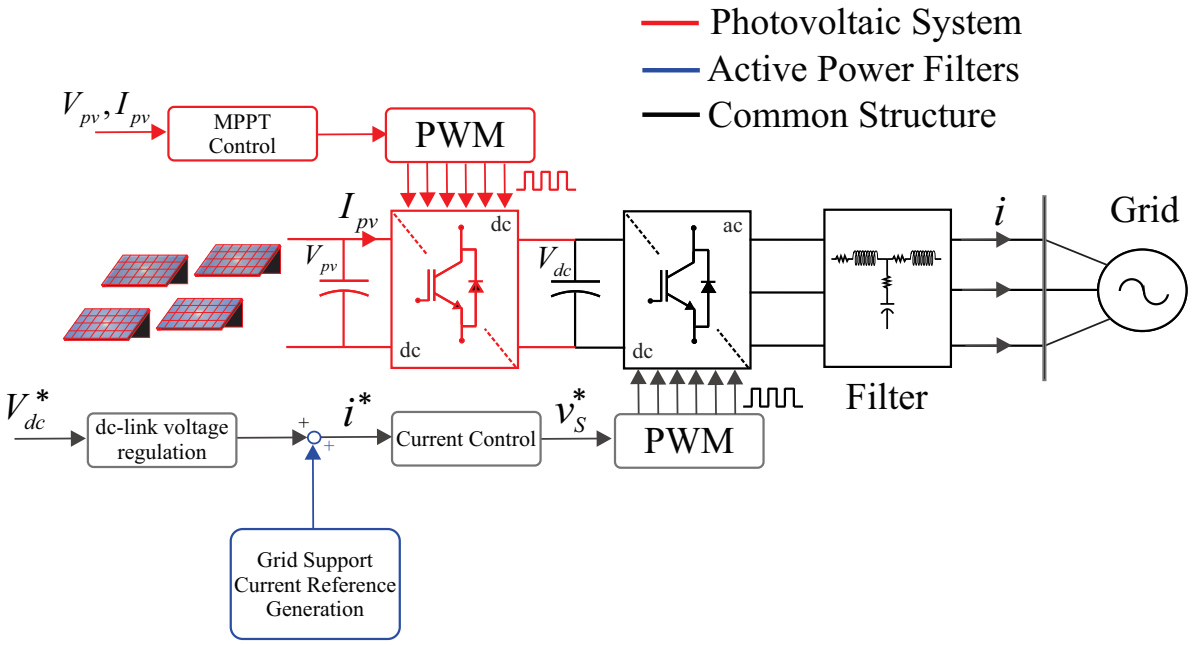

Figure 3 – Active power filter and distributed generators basic power structure and generic control technique.

harmonic. In Campanhol et al. (2017) it is proposed a grid-connected PV system with a dual compensating strategy and feedforward control loop, working as a unified PQ conditioner.

However, the necessary implementations bring new challenges that opened up new research topics, such as detecting (ZENG; LI; SHAO, 2018; ASHRAF; KHAN; CHOI, 2021) and controlling harmonic currents (SILVA JUNIOR et al., 2019; MISHRA; LAL, 2023) and limiting current in the system (XAVIER; CUPERTINO; PEREIRA, et al., 2019; ALONSO, A. M. et al., 2021). Reference Xavier, Cupertino, Pereira, et al. (2019) proposed two current dynamic saturation techniques for PV inverters during HCS to improve PQ. The open-loop technique is less susceptible to instability, while the closed-loop has a less complex algorithm, requiring more computational power.

Additionally to the challenges encountered during implementation, HCS changes some PV structures' behavior, such as the dc-link (DE JESUS et al., 2019) and passive filter (DE JESUS et al., 2021), presenting new research opportunities in this field. de Jesus et al. (2019) discussed the effect of HCS on the efficiency of maximum power point tracking (MPPT) algorithms in PV inverters. A mathematical model was developed to relate HCS and the oscillation in the dc-link capacitor voltage, and simulations and experiments were performed to validate the model. The results showed that all MPPT strategies experienced a degradation in efficiency due to HCS. Also, ancillary services such as reactive power and harmonic support cause additional losses in the switching devices, leading to an increase in their temperature (CALLEGARI; SILVA, et al., 2019). Since the lifetime of these devices is reduced by to thermal stress (ANURAG;

YANG; BLAABJERG, 2015; DE BARROS et al., 2018; YUNTING et al., 2020), it is crucial to analyze the impact caused by multifunctional operation. In Yunting et al. (2020) it is explained that the thermal stress caused by the power losses of semiconductors and capacitors is a major contributor to the short lifetime of inverters. Additionally, the provision of ancillary services, such as reactive power support, may further increase the thermal stress and negatively impact the lifetime of inverters (CALLEGARI; SILVA, et al., 2019).

1.3 Objectives

1.3.1 Main objective

The primary objective of this thesis is to investigate the impact of HCS on the functioning of grid-tied PV systems. The study aims to accomplish this by analyzing the effects of HCS on system operation, specifically examining the operating limits during HCS and their effect on system losses, as well as exploring how the LCL filter passive elements and dc-link voltage contribute to these effects. Additionally, the research will identify any variances from normal system operation and offer guidelines for assessing the operational status of multifunctional PV systems.

1.3.2 Specific objectives

The following specific objectives will be approached in this work:

1. *MI modeling, control, and design*: A comprehensive review of renewable generation systems with HCS capability will be conducted.

2. *Defining the MI capability curves*: Capability curves define the boundaries within which the equipment can operate safely. Thus, it is proposed to develop an algorithm to create MI capability curves based on the inverter's limits. To validate the proposed algorithm, simulations will be conducted in PLECS software and experiments will be performed on a test bench.

3. *MI filter design and analysis*: This topic proposes the definition and comparison of passive filter designs for HCS capability based on losses and power density using Pareto optimization analyses.

4. *Grid-connected inverter with ancillary services*: Conclusions will be drawn from comparisons between a system designed to provide HCS and a system whose only function is active power injection into the grid.

1.4 Contributions

The main contributions of this work are expected to expand the understanding of the topic and provide new solutions and recommendations for future research. In summary the most important findings, conclusions, and recommendations are:

1. Guidelines to obtain the voltage and current capability curves for PV inverters.
2. Impact of LCL passive elements and dc-link voltage on capability curves.
3. Influence of inductors nonlinearities on PV inverter capability curves.
4. Discussion of resonant control with adjustable proportional gain to mitigate the effects of inductors saturation in inverter current control.
5. Analysis of current control sensitivity due to the impact of nonlinear inductors.
6. Recommendations for optimal LCL filter component selection based on total system losses and HCS effects.

To achieve the proposed contributions, this thesis makes use of algorithms developed in MATLAB environment. These algorithms are responsible for generating the inverter capability curves. Moreover, electrical and thermal simulations on PLECS environments are used to analyze the HCS effects on the inverter. Finally, experimental results for the capability curves are obtained in a representative setup.

1.5 List of publications

From a scientific production point of view, this PhD. resulted in the production of the following journal articles:

- V. M. Rodrigues de Jesus, A. F. Cupertino, L. S. Xavier, H. A. Pereira and V. F. Mendes, "Operation Limits of Grid-Tied Photovoltaic Inverters With Harmonic Current Compensation Based on Capability Curves," in IEEE Transactions on Energy Conversion, vol. 36, no. 3, pp. 2088-2098, Sept. 2021, doi: 10.1109/TEC.2021.3050312.
- V. M. R. de Jesus, A. F. Cupertino, L. S. Xavier, H. A. Pereira and V. F. Mendes, "Comparison of MPPT Strategies in Three-Phase Photovoltaic Inverters Applied for Harmonic Compensation," in IEEE Transactions on Industry Applications, vol. 55, no. 5, pp. 5141-5152, Sept.-Oct. 2019, doi: 10.1109/TIA.2019.2927924.

1.6 Text organization

This PhD. thesis is organized into six chapters. Chapter 1 presents the motivations, objectives, and methodology of the research. Chapter 2 contains a MI literature review and discusses the suitable topology selection and implementation for MI application. Chapter 3 defines the MI capability curves and presents an algorithm proposed to determine the limits of HCS. Chapter 4 examines the impact of nonlinear inductors on the capability curves and evaluates the control system's susceptibility to nonlinearities. Chapter 5 discusses the LCL filter design implications considering HCS capability based on Pareto optimization analysis. Finally, chapter 6 states the conclusions obtained from this research and a proposal of future development works.

2 DG with power quality enhancement

2.1 Classification of multifunctional inverters

MI can be classified into different categories based on its power structure and control techniques, as described in Teke and Latran (2014). These categories include: power processing stages; power supply type; inverter topology; control techniques; and detection techniques. As a result, several MI structures have been discussed in the literature. A comprehensive classification of MI is presented in Fig. 4.

2.1.1 Power processing stages

MI can be classified based on the number of power structure stages, as reported in Kjaer, Pedersen, and Blaabjerg (2005), Nema, Nema, and Agnihotri (2011) and Kolantla et al. (2020). Typically, grid-connected PV systems can consist of either one or two conversion stages. The one-stage configuration typically utilizes a voltage source inverter (VSI) as its primary component. In this configuration, the control system typically consists of two loops, with the first stage responsible for controlling the dc-link voltage and extracting the maximum power, and the second stage responsible for current control (KJAER; PEDERSEN; BLAABJERG, 2005). A generic topology of a single-stage system is depicted in Fig. 5-(a).

The two-stage configuration of the PV system consists of an RES and a dc/dc converter, which serves as the first conversion stage and is used for voltage control and to follow the maximum power point. The use of step-up converters helps to reduce the number of PV modules in series in photovoltaic systems (NEMA; NEMA; AGNIHOTRI, 2011), thus supplying the necessary voltage to the inverter and preventing it from operating in overmodulation. The second conversion stage enables the conversion of power to sinusoidal voltage and current. A generic topology of a two-stage system is depicted in Fig. 5-(b). The two-stage configuration is widely used because it has simple control structures that operate independently (KOLANTLA et al., 2020).

2.1.2 Inverter topology

The industrial sector loads often consist of a combination of single-phase and three-phase systems, supplied by 4-wire three-phase grids. These ac-powered loads can be classified based on their power supply circuit (KJAER; PEDERSEN; BLAABJERG, 2005; NEMA; NEMA; AGNIHOTRI, 2011; KOLANTLA et al., 2020). Single-phase or three-phase MI systems can provide ancillary services. However, the existence of single-phase/two-phase loads in the distribution system can lead to load voltage asymmetries and neutral wire zero-sequence current

Source: Own authorship.

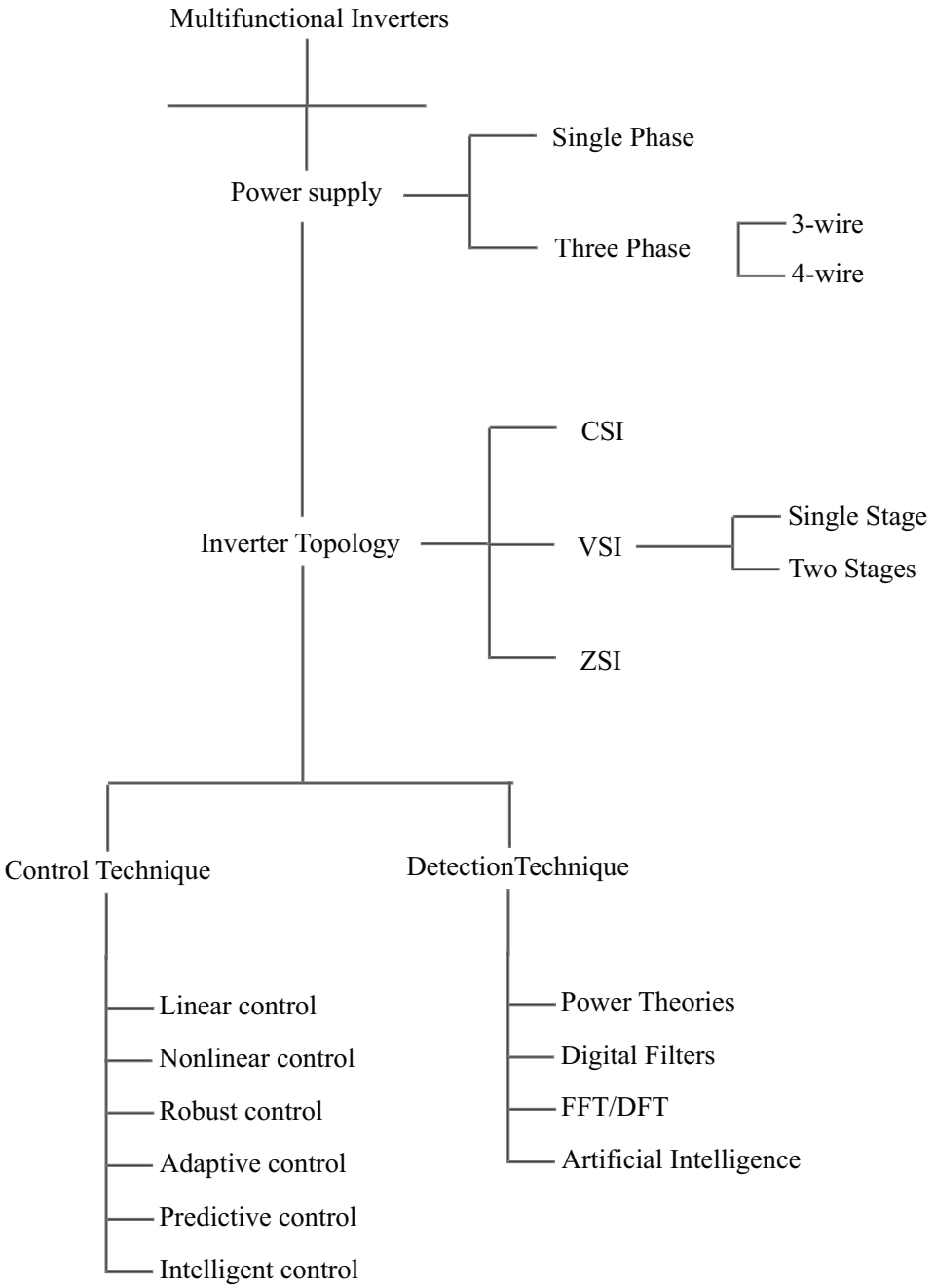

Figure 4 – Multifunctional inverters classification.

formation (WANG; DUARTE; HENDRIX, 2011). These problems can be mitigated by three-phase MI systems with a neutral wire (four-wire systems) (MA; ELLINGER; PETZOLDT, 2011). Three-phase systems also provide unbalance mitigation capabilities (ALI et al., 2019).

In the literature, there are reports of single-phase systems employed for PQ improvement using various topologies (PEREIRA et al., 2019). Single-phase systems typically have low capacities, with power ranging from 0.5 to 10 kW. The two-wire configuration of an H-bridge inverter is the most commonly used single-phase configuration for PQ disturbance support

Source: Own authorship.

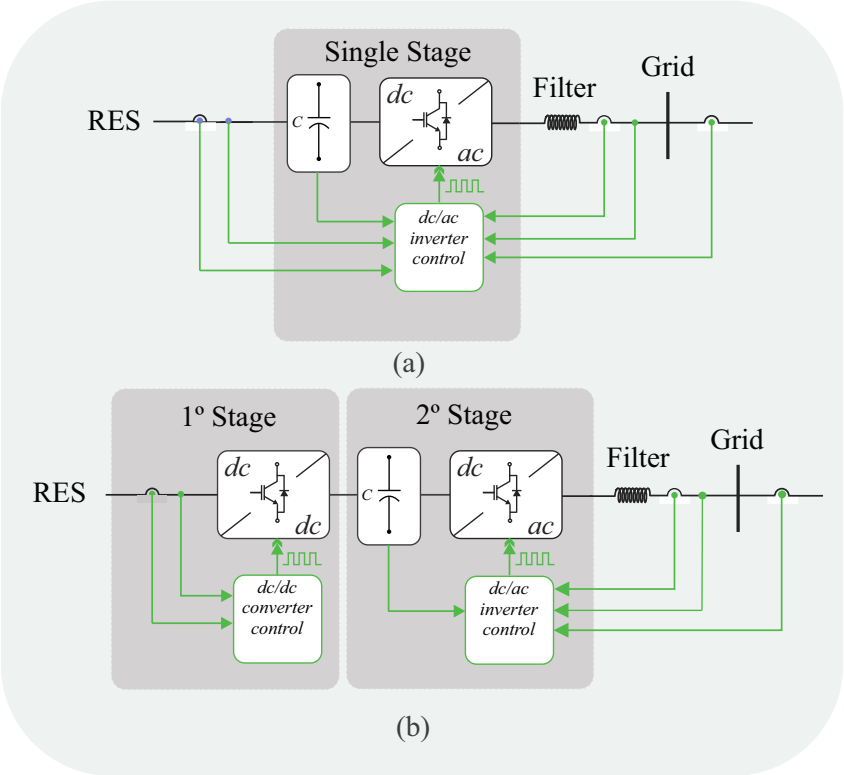

Figure 5 – Power processing stages: (a) single-stage; and (b) two-stage

(TEKE; LATRAN, 2014; MORTEZAEI et al., 2015; ANTUNES; SILVA, et al., 2018; PEREIRA et al., 2019). Fig. 6-(a) depicts the single-phase topology with a full-bridge inverter. The authors in T. Wu et al. (2007) propose a two-wire single-phase inverter composed of a half-bridge, which has PQ enhancement capabilities and can inject power from the PV system while providing ancillary services to the grid. The main advantage of the half-bridge system is its reduced cost, achieved through the use of half the switches compared to the full-bridge inverter. However, the topology presents challenges, such as balancing the capacitors voltage. Fig. 6-(b) shows the half-bridge topology diagram.

In the study conducted by Picard, Sgro, and Gioffre (2012), the authors propose a grid-tied single-phase inverter system with a unique stage composed of a four-leg inverter. The system includes both a full bridge inverter and a low-power, high-frequency auxiliary inverter connected by a high-frequency transformer and passive filter. This arrangement enables the system to perform active filtering functions. The diagram of the proposed topology is presented in Fig. 7-(a).

Additionally, the authors in Antunes, Silva, et al. (2018) propose a MI inverter based on a series compensator. This inverter is designed to switch between series and parallel connections, depending on the system conditions, via the use of circuit breakers (S) and bidirectional switches (SS). This topology provides the ability to perform multiple functions for voltage and current

Source: Own authorship.

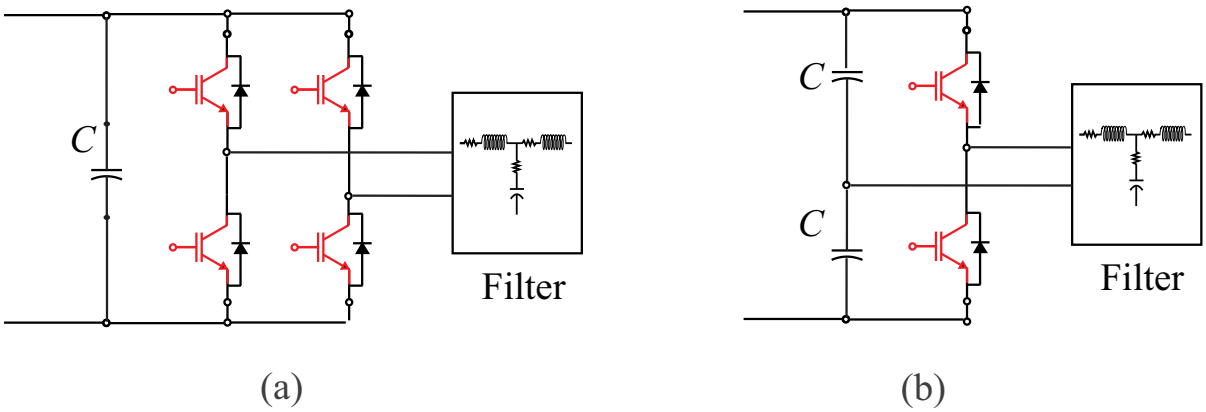

Figure 6 – Single-phase inverters topologies: (a) full-bridge; and (b) half-bridge.

disturbances, including voltage regulation during sags and swells, as well as reactive power support, harmonics reduction, and current unbalance correction. The diagram of the half-bridge topology is presented in Fig. 7-(b).

Three-phase MI inverters have a high capacity for injecting power into the grid, usually greater than 10 kW. The most common topology used for MI is the three-phase three-wire VSI system (MOUSAVI et al., 2018; DASH; SWAIN, 2018). The advantages of the VSI system include lower volume, reduced cost, and flexibility in control when compared to other topologies (SOLATIALKARAN; KHAJEH; ZARE, 2021). Fig. 8-(a) shows the diagram of a three-phase inverter.

The authors in Dasgupta et al. (2013) propose a three-phase three-wire two-leg inverter with the capability of providing reactive power support. In this topology, one phase is connected at the midpoint between the dc-link capacitors. The main advantage of the two-leg configuration is the reduction in the number of switching devices. However, voltage variations across the two dc-link capacitors may occur (BLAABJERG; NEACSU; PEDERSEN, 1999), and more reliable modulation techniques are required (NGUYEN; LEE; NGUYEN, 2010). Fig. 8-(b) illustrates the four-switch topology.

In the literature, there are different topologies for 4-wire three-phase MI systems, such as the split capacitor and 4-leg inverter (TEKE; LATRAN, 2014). The 4-leg inverter is a frequent choice as it compensates neutral current with only two additional switches. While the 4-leg topology requires two more switches, which can increase the overall switching losses, the main disadvantage of the split capacitor topology is the expensive and large capacitor, as well as the additional control loop required to achieve equal voltage sharing between the split capacitors (KIM et al., 2021). Fig. 9 shows both topologies for inverters with a neutral wire.

MI can be classified based on the dc/ac structure used for conversion. In the literature, three configurations have been presented for use in multifunctional systems: the current source

Source: Own authorship.

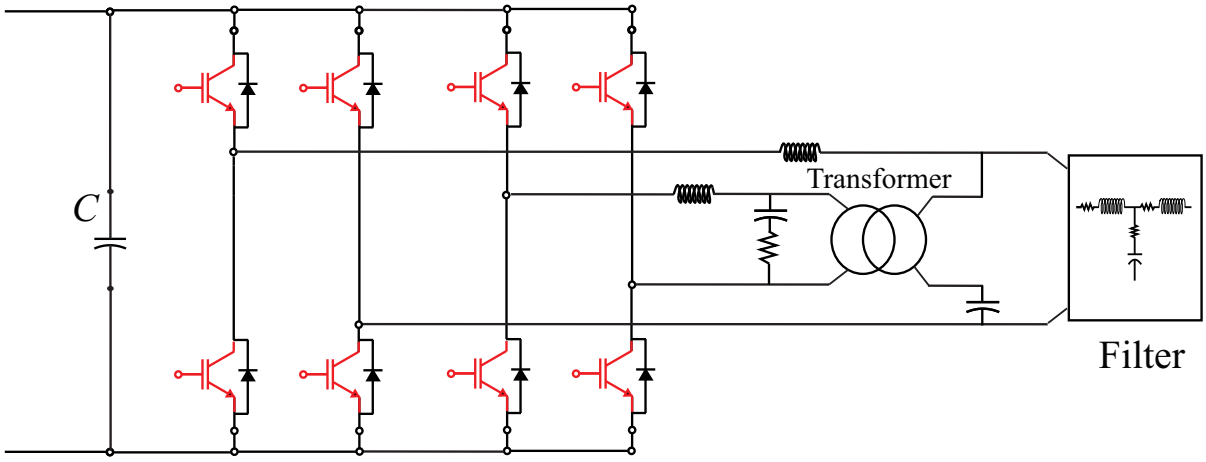

(a)

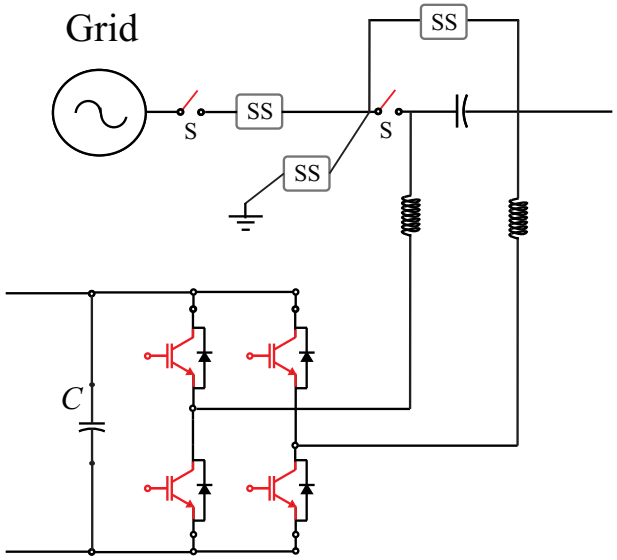

(b)

Figure 7 – Single-phase inverters topologies: (a) dual full bridge inverter proposed in (PICARD; SGRO; GIOFFRE, 2012); and (b) Series/shunt full-bridge proposed in (ANTUNES; SILVA, et al., 2018).

inverter (CSI) (LIU; WANG, et al., 2021), the VSI (ALONSO, A. M. d. S. et al., 2020), and the Z-source inverter (ZSI) (DIVYA; RAJ; MANIRAJ, 2017).

The CSI topology is shown in Fig. 10-(a). The first option is the CSI, which uses an inductor in the dc-link to provide the inverter with a constant current source. This configuration acts as a boost inverter, facilitating the matching of grid voltages without the need for an additional conversion stage (SAEED; IBRAR; SAEED, 2017). In this topology, it is necessary

Source: Own authorship.

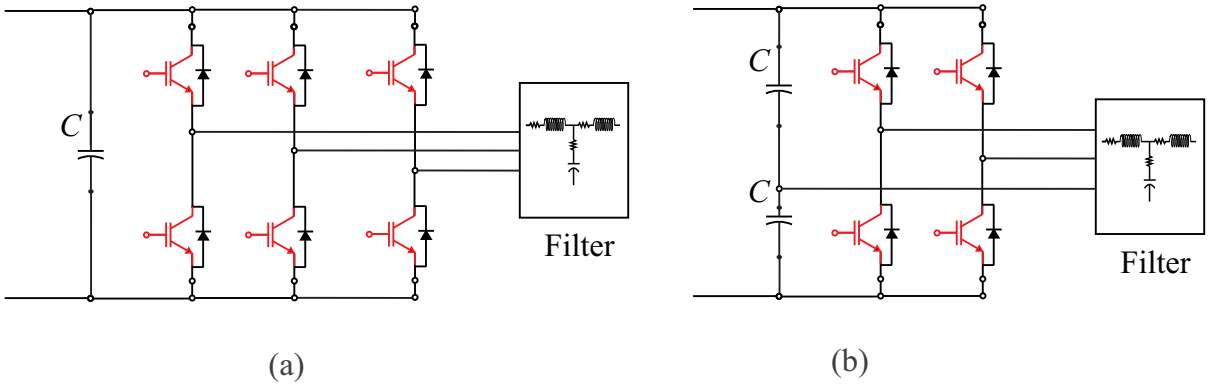

Figure 8 – Three-phase grid-connected VSI: (a) three legs inverter ; and (b) three-wire two-legs inverter

Source: Own authorship.

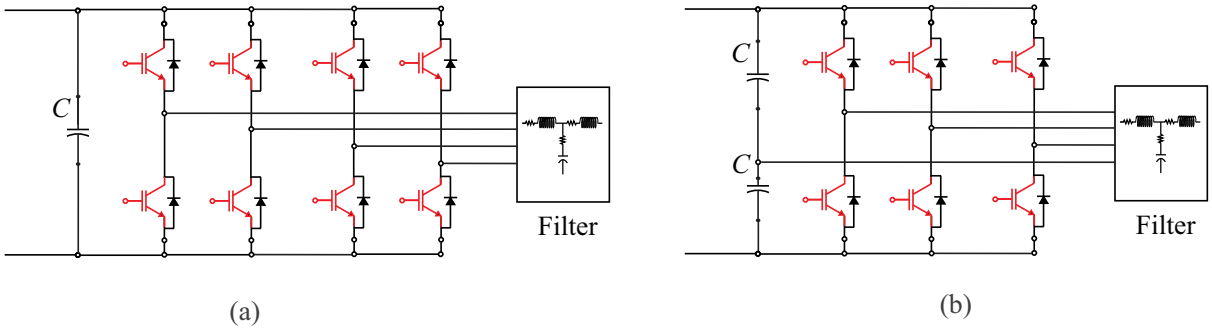

Figure 9 – 4-wire inverter topologies: (a) 4-leg inverter and (b) split capacitor inverter.

to implement overlapping switch gate signals during the commutation process to prevent voltage spikes caused by the intermittent dc current (HANIF; BASU; GAUGHAN, 2011; GENG et al., 2018). A distributed system based on a CSI with advanced active filter functionalities is presented in (GEURY; PINTO; GYSELINCK, 2015).

The VSI topology is depicted in Fig. 10-(b). The most studied inverter structure in the literature is the VSI (BASTIDAS-RODRIGUEZ; RAMOS-PAJA, 2017). The dc-link in this structure functions as a voltage source, utilizing a capacitor. Typically, synthesized voltages with lower amplitudes than the available dc-link voltage are used in the VSI (SAEED; IBRAR; SAEED, 2017). This issue can be addressed by incorporating a dc/dc step-up converter in parallel with the capacitor (FLORESCU et al., 2010). To prevent the occurrence of shoot-through, which refers to the simultaneous turn-on of two adjacent switches, it is important to exercise caution and take measures to avoid high current flow through the semiconductor devices. Such measures may include adding dead time to the gate driver or through algorithmic implementation (HANIF; BASU; GAUGHAN, 2011; GENG et al., 2018).

The ZSI topology is illustrated in Fig. 10-(c). The ZSI topology, which can function

Source: Own authorship.

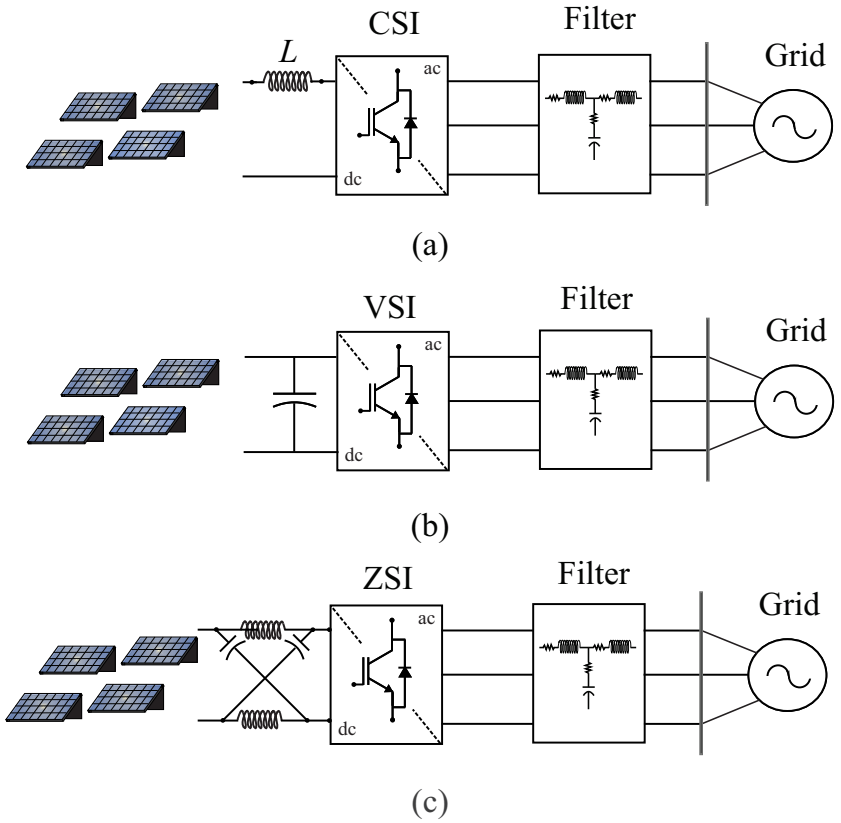

Figure 10 – Power structure: (a) CSI; (b) VSI and (c) ZCI.

as both a voltage and current source dc-link (GAJANAYAKE; VILATHGAMUWA; LOH; BLAABJERG, et al., 2007), utilizes a different passive element structure in the dc link consisting of two capacitors and two inductors. This structure has a larger volume due to the high number of passive elements. A PV system capable of providing ancillary services using a Z source converter is presented in Gajanayake, Vilathgamuwa, Loh, Teodorescu, et al. (2009).

2.1.3 Control techniques

Despite many advantages of MI, there are some control challenges associated with their implementation. Further control structures must be added due to the multiple frequencies present in the current reference (XAVIER; CUPERTINO; DE RESENDE, et al., 2017). The majority of VSI applications feature a control structure that includes an internal current feedback loop (ANTUNES; SILVA, et al., 2018; SAFA et al., 2018; NADERI et al., 2019; ALONSO, A. M. d. S. et al., 2020). This current control mode is preferred due to its ability to soften the current dynamic behavior and provide high accuracy in controlling the waveform of instantaneous currents (KAZMIERKOWSKI; MALESANI, 1998). In the literature, several controllers have been used for MI systems. In Liu, Caldognetto, and Buso (2020) authors offers a comprehensive review of various control strategies for grid-tied inverters utilized in microgrids, which are

crucial for integrating renewable energy sources and energy storage systems into low-voltage power distribution systems. The controllers can be classified into six categories (ZEB et al., 2018): linear control, nonlinear control, robust control, adaptive control, predictive control, and intelligent control.

- Linear control: Control based on linear systems functioning and dynamics. Linear systems are those that follows the superposition principle. The two main linear controllers used in multifunctional operation are the classic proportional - integral - derivative (PID) action and the proportional resonant (PR) controller (MISHRA; LAL, 2023).
- Nonlinear control: Nonlinearities are present in all real systems to some degree, and nonlinear control can often provide better performance than linear control (SRINIVAS et al., 2018). However, nonlinear controllers are generally more complex to implement. One common type of nonlinear controller used for MI is the hysteresis controller (SHAH et al., 2019).
- Robust control: Type of controllers that deal very well with uncertainties around the plant model representation. In other words, even if the model has errors, the controller is able to guarantee stability and good performance. H-∞ control is a good example of robust controllers used for MI (MOHAMMADI et al., 2022).
- Adaptive control: It is a form of control that adapts to the system necessities due to modeling errors/uncertainties or system parametric variation. Different from robust control, adaptive control does not require system parameters variations limits, however, this control requires a high computational burden (ESPI et al., 2011; ZEB et al., 2018).
- Predictive control: Uses future information based on the system model to optimize the control action. In some cases it is easy to implement, like the classic controllers, but it requires a lot of processing due to the amount of calculations (BUSO; CALDOGNETTO; BRANDAO, 2016; BUSO; CALDOGNETTO; LIU, 2019).
- Intelligent control: Control strategies that adopt some computational intelligence technique. Neural network, and Fuzzy controllers are constantly found in the literature (SINGH; CHANDRA, 2011; ANTUNES; SILVA, et al., 2018; DASH; SWAIN, 2018; SUN et al., 2019).

Control structures can be implemented in one of three coordinate frames: abc (SRINIVAS et al., 2018), stationary ($\alpha\beta$) (PEREIRA et al., 2019), or synchronous (dq) (HAMROUNI; YOUNSI; JRAIDI, 2019). In the literature the utilization of the abc reference frame for current control has been widely studied. Distinct strategies have been proposed for implementing current control in the abc frame that can involve the use of a separate controller for each phase (MIVEH et al., 2016) or that involves the use of only two controllers through a chosen decoupling method

(COSTA et al., 2021). The latter approach is favored due to its reduced computational demands. PI, PR and nonlinear controllers such as hysteresis or deadbeat controllers are used for current control in abc reference frame (ZEB et al., 2018). Fig. 11-(a) shows a generic current control in the natural reference frame. In (SRINIVAS et al., 2018), the authors propose a grid-connected photovoltaic inverter with the capability to compensate for harmonic and imbalanced currents. The control is carried out in the abc natural reference frame using a hysteresis controller.

In the $\alpha\beta$ control, the currents are transformed to the stationary frame using the Clarke transform. This type of control has the advantage of simplifying the three-phase circuit into a two-phase oscillating system. Resonant controllers are commonly used to control the $\alpha\beta$ coordinates (PEREIRA et al., 2019) as they exhibit a high current gain close to the resonant frequency, high dynamic performance, and minimal error in steady state (YEPES et al., 2011). Fig. 11-(b) shows a generic current control in the stationary frame.

In the dq control, voltages and currents are transformed to the synchronous reference frame using the Park transform. This transformation decouples the currents into two components: active (i_d) and reactive (i_q). The advantage of the synchronous coordinate system is that the controlled signals of the fundamental frequency components are continuous for balanced systems. Fig. 11-(c) shows a generic current control in the synchronous reference frame.

In Ali et al. (2019), the authors propose a control technique for a three-phase inverter that allows for compensation of unbalance, harmonics, and dc currents. The control consists of a sequence analyzer that divides the load current into four components (positive, negative, harmonic, and dc), and decouples these components so that a PI controller can be used in the synchronous reference frame. In Mousavi et al. (2018), the authors implement a grid-connected DG with coordinated current support and voltage support. The voltage support is achieved through the injection of reactive power into the grid, and the harmonic support is achieved through the implementation of a virtual impedance at the specific harmonic frequency. The control is performed in the stationary frame, and a resonant proportional controller is used.

In Singh, Khadkikar, et al. (2011), the authors present a control technique for a 4-wire three-phase inverter that has PQ improvement capability. The technique uses a four-leg topology and a hysteresis current control, which allows the compensation of neutral currents and the creation of a balanced current flow from the grid to the load. In Fei Li et al. (2011), the same topology as in Singh, Khadkikar, et al. (2011) is used, and a new form of control with ancillary service capability is proposed. The reference generator, which operates in the synchronous reference frame, separates the measured load current into positive and negative sequences, enabling independent injection of active power and reactive support. The control uses a multi-resonant proportional controller to control the current injected into the grid. In Boukezata et al. (2016), a predictive control based on the discrete model of the system is proposed. This control takes into account the controlled variables' behavior for all VSI switching states and the operating cost as required by the grid.

Source: Own authorship.

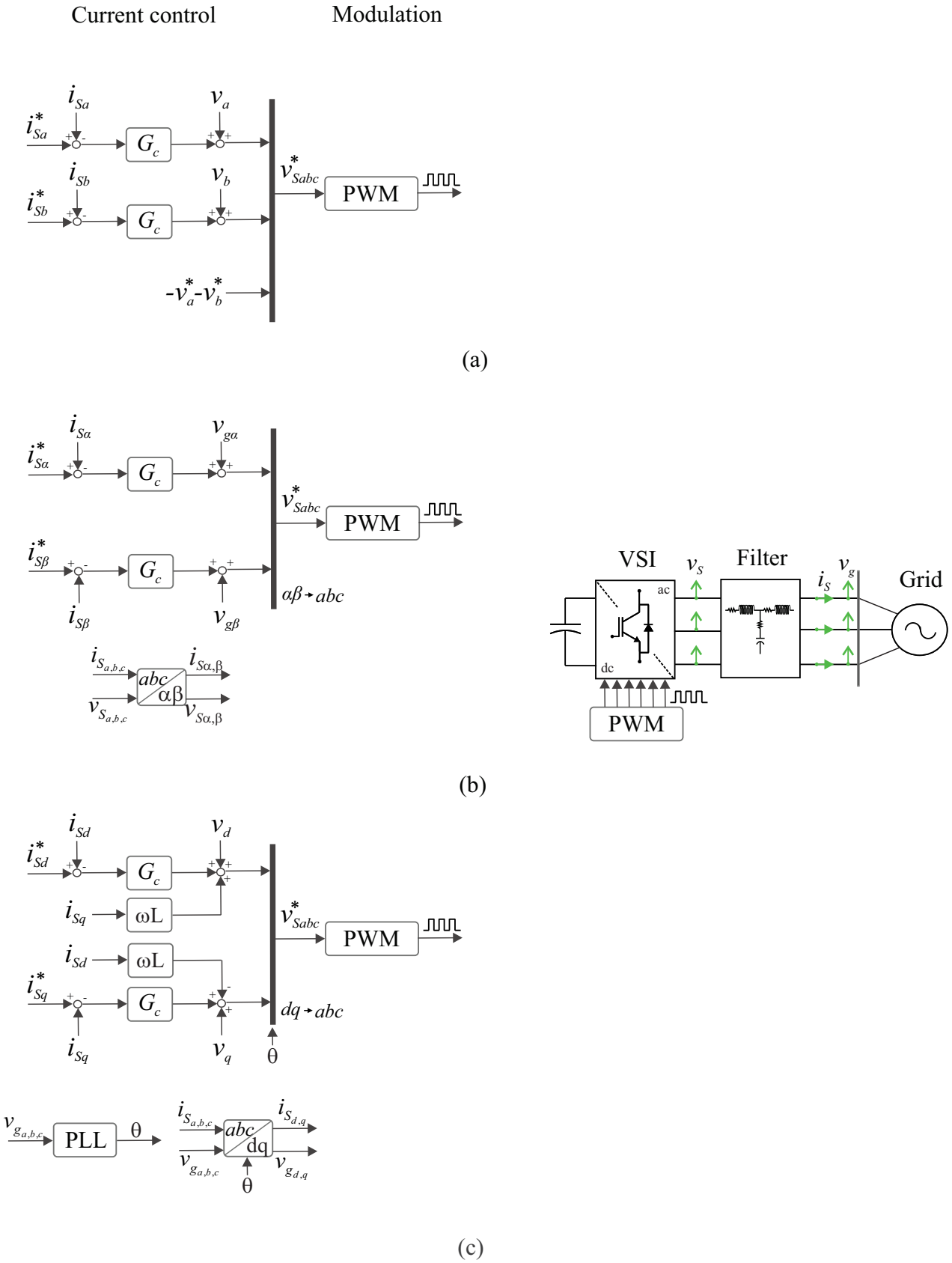

Figure 11 – Control structure: (a) abc; (b) $\alpha\beta$ and (c) dq.

Each reference frame has its own advantages and disadvantages, and the choice of a particular reference frame may depend on the specific requirements and constraints of the system. In Timbus et al. (2009) the authors examines the performance of various linear current controllers. The evaluation of the controllers is conducted under two operating conditions, steady-state, where the contribution of the controllers to the total harmonic distortion of the grid current is analyzed, and transient conditions, such as input power variations and grid voltage faults. Results indicate that while all controllers exhibit satisfactory behavior in all conditions, the deadbeat controller in abc frame proves to be superior in the case of grid faults. The authors in Costa et al. (2021) perform a quantitative comparison based on mathematical models of grid disturbances, computational effort, and steady-state and transient performance evaluation using experimental results. Results showed that the abc frame has lower computational effort and similar performance compared to the other two frames.

2.1.4 Harmonic detection techniques

One challenge in the implementation of the MI is accurate current detection. Various techniques, both in the time and frequency domains, have been proposed to decompose the signal accurately (JANPONG; AREERAK; AREERAK, 2021). These include: pq theory (WATANABE; AKAGI; AREDES, 2008), conservative power theory (TENTI; MATTAVELLI; MORALES PAREDES, 2010), discrete Fourier transform (SOLOMON, 1994), sliding window Fourier analysis (CHEN et al., 2020), synchronous reference frame (LI, X. et al., 2015), dq axis with Fourier transform (SUJITJORN; AREERAK; KULWORAWANICHPONG, 2007), adaptive notch filters (YAZDANI; BAKHSHAI, et al., 2009), and Kalman filter (WANG; LIU, 2015).

In Watanabe, Akagi, and Aredes (2008), the authors present a strategy based on the instantaneous power theory (IPT) for separating the current into two components, oscillating and average. Fig. 12-(a) illustrates the IPT block diagram. The calculations are carried out in the stationary reference frame and are based on the following equations:

$$\begin{bmatrix} p \\ q \end{bmatrix} = \begin{bmatrix} v_\alpha & v_\beta \\ -v_\beta & v_\alpha \end{bmatrix} \begin{bmatrix} i_\alpha \\ i_\beta \end{bmatrix}. \tag{2.1}$$

In a three-phase system, the instantaneous values of active power (p) and reactive power (q) contain both dc and ac components (depending on the system's active, reactive, and distortion powers). The average values of p and q represent the active ($\bar{p}$) and reactive ($\bar{q}$) load power, which can be removed by using a high-pass filter (HPF). The ac components ($\tilde{p}$ and $\tilde{q}$) represent the harmonic distortion present in the load current. Finally, the oscillating components are transformed back to the stationary reference frame using:

$$\begin{bmatrix} i_\alpha^* \\ i_\beta^* \end{bmatrix} = -\frac{1}{v_\alpha^2 + v_\beta^2} \begin{bmatrix} v_\alpha & -v_\beta \\ v_\beta & v_\alpha \end{bmatrix} \begin{bmatrix} \tilde{p} \\ \tilde{q} \end{bmatrix}. \tag{2.2}$$

Source: Own authorship.

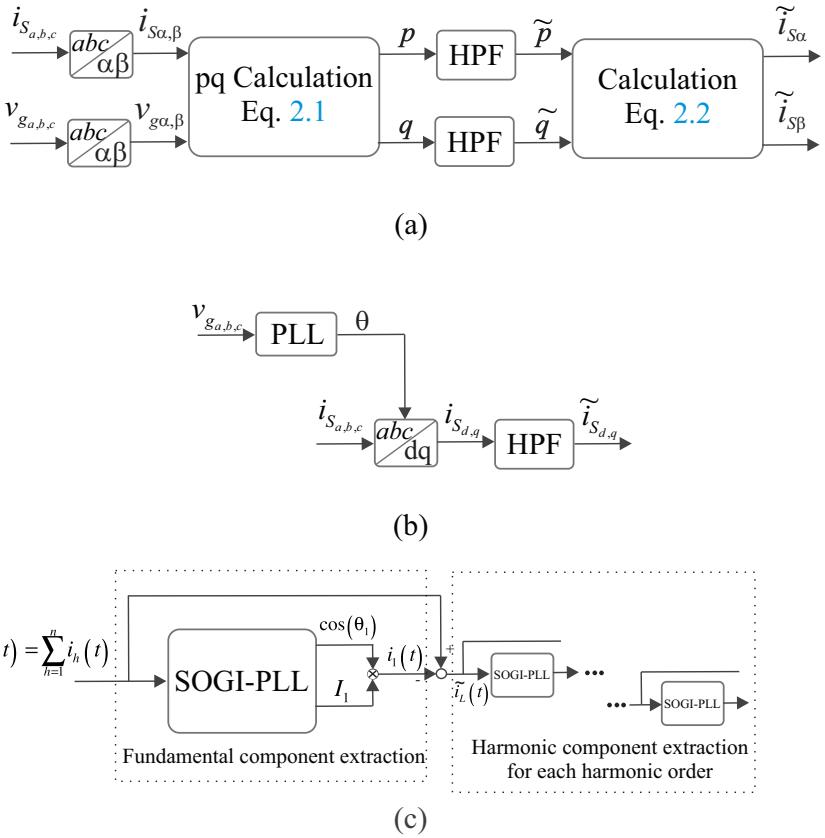

Figure 12 – Control structure: (a) IPT; (b) dq synchronous frame and (c) Cascaded Second-Order Generalized Integrator.

In Takeda et al. (1988), Asiminoaei, Blaabjerg, and Hansen (2005), and Sujitjorn, Areerak, and Kulworawanichpong (2007), a detection technique based on the Park transformation's space vector in the synchronous reference frame is presented. The technique utilizes the fundamental current angular frequency in the rotating frame, where the fundamental frequency current appears as dc quantities and the harmonic current content appears as ac signals. To extract the compensated harmonic currents, a HPF is used to remove the dc current portion. Fig. 12-(b) presents the diagram of the synchronous reference frame approach.

In Pereira et al. (2019), a flexible HCS strategy is proposed for both single-phase and three-phase inverters. The strategy is based on a Second-Order Generalized Integrator (SOGI) coupled with a PLL (Phase-Locked Loop) that detects the most significant harmonic current. A cascade structure that detects the 'n' largest harmonic components for compensation is also presented. Fig. 12-(c) presents the cascaded SOGI-PLL schematic.

Furthermore, specific techniques for detecting harmonic components in the frequency domain are utilized, which are typically based on Fourier analysis, adapted to reduce the number of calculations required, thereby enabling real-time implementation in DSPs. As presented in Sujitjorn, Areerak, and Kulworawanichpong (2007), a harmonic detection technique that combines the synchronous reference frame with sliding window Fourier analysis was proposed. The results indicated that the combined method has equivalent performance in terms of HCS when compared to sliding window Fourier analysis. However, it demonstrates superior performance in terms of phase balancing.

In Mortezaei et al. (2015), a control strategy for a grid-connected multilevel inverter with ancillary services capability was proposed. The control strategy employed the conservative power theory (CPT) to decompose signals through hierarchical control, allowing for selective HCS of decomposed quantities. The CPT presented in Tenti, Mattavelli, and Morales Paredes (2010) promotes a time-domain technique that allows for current decomposition, where all terms have physical meaning and are orthogonal to each other. In a polyphase system, these terms include:

- Balanced active current (i_a^b): constant active power conversion;
- Balanced reactive current (i_r^b): energy storage associated with capacitors and inductors;
- Unbalance active (i_a^u) and reactive (i_r^r) currents: different values of conductance and reactivity per phase;
- Void current (i_v): is related with the nonlinearity between voltage and current.

The techniques can be characterized and evaluated based on several factors, including necessary measurements, dynamics, steady-state accuracy, selective HCS, single- and three-phase applications, computational consumption time, and others (ANTUNES; XAVIER, et al., 2017). The selection of a detection technique must strike a balance between the desired features. Reports indicate that no single technique excels in all aspects (LV et al., 2020; JANPONG; AREERAK; AREERAK, 2021).

2.2 Passive Filters

Passive filters are employed to integrate the photovoltaic system into the PCC, reducing high-frequency harmonics generated by inverter switching. These harmonics, if not properly managed, can flow into the power system and potentially violate recommendations and standards that dictate acceptable levels of harmonic currents in the grid (SOLATIALKARAN; KHAJEH; ZARE, 2021). Therefore, an effective filter design is crucial to mitigate the harmonic injection into the grid. There are several passive filter topologies reported in the literature, including L

filters (PAUKNER et al., 2015), LC filters (AZRI; ABD RAHIM, 2011), LCL filters (PENA-ALZOLA; LISERRE; BLAABJERG; ORDONEZ, et al., 2014), and LLCL filters (WU, W. et al., 2014). The various passive filter topologies are depicted in Fig. 13.

Source: Own authorship.

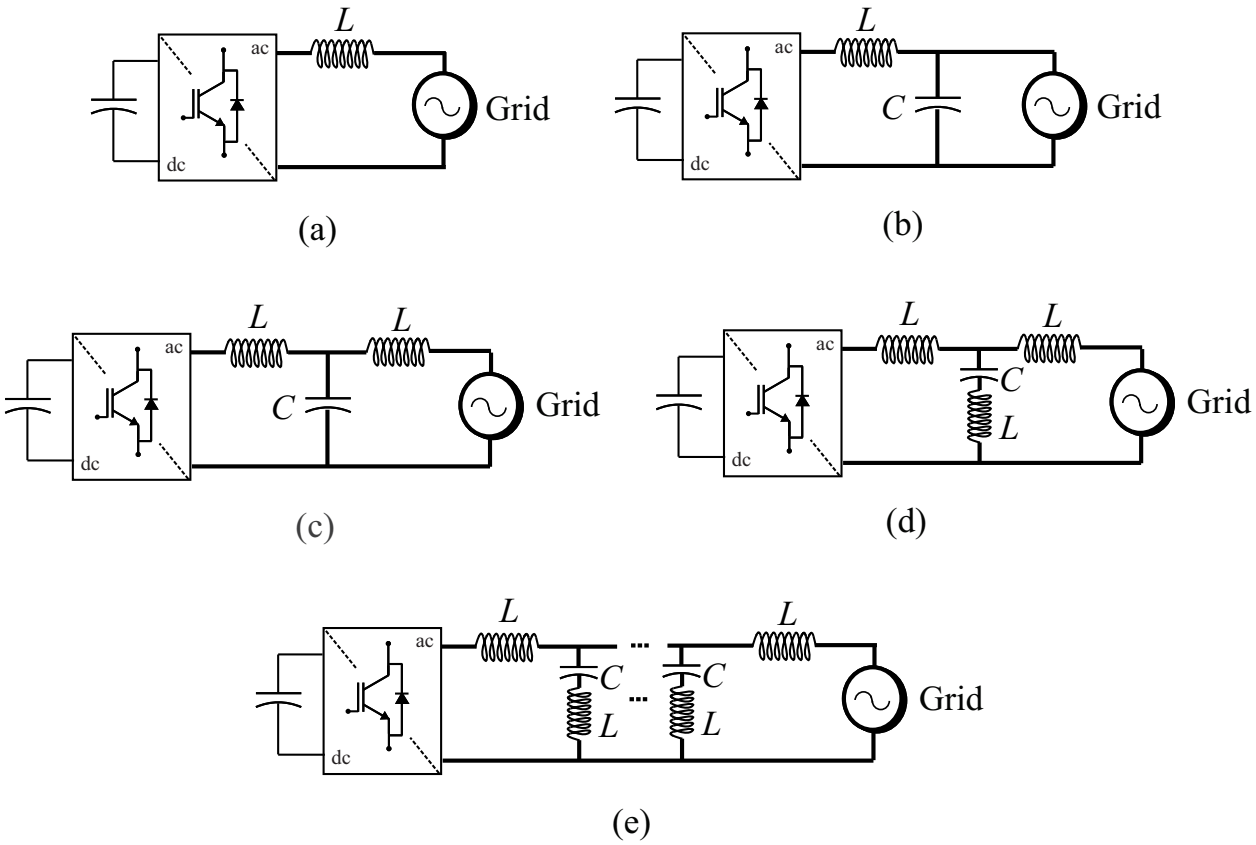

Figure 13 – Control structure: (a) L filter; (b) LC filter; (c) LCL filter; (d) LLCL filter; and (e) multi-branch filter.

Initially, first-order simple L filters were introduced as a solution for reducing current ripples and harmonics (SOLATIALKARAN; KHAJEH; ZARE, 2021). Although L filters are effective in these regards, they entail significant power losses and voltage drops due to the need for large inductors to comply with strict grid standards (BERES et al., 2016). Additionally, the use of bulky inductors can negatively impact control dynamic performance (GOMES; CUPERTINO; PEREIRA, 2018). To address these challenges, higher-order filters have been employed.

The LC filter, a second-order filter, offers improved harmonic reduction with reduced inductance values (BUYUK et al., 2016). However, the shunt capacitor added in this topology can be subjected to high currents from line voltage harmonics. Additionally, a resonance frequency that couples with the grid impedance may amplify high-order harmonic currents (GOMES; CUPERTINO; PEREIRA, 2018).

The LCL filter depicted in Fig. 13 (c) is a third-order filter that offers exceptional current ripple attenuation with lower inductance values, as stated in (SOLATIALKARAN;

KHAJEH; ZARE, 2021). Unlike LC filters, the LCL filter capacitor is not subjected to line voltage harmonics (ALAMRI; ALHARBI, 2020). Compared to L and LC filters, LCL filters boast several improvements such as a lower volume, faster dynamic response, less susceptibility to grid impedance variation, reduced voltage drop, and enhanced attenuation ratio, as noted in Gomes, Cupertino, and Pereira (2018). However, some drawbacks of high-order passive filters like the LCL filter are intrinsic resonance peaks and higher system complexity when compared to lower order filters (GOMES; CUPERTINO; PEREIRA, 2018). These challenges result in control difficulties, such as instability in the control system and resonance between the grid and the inverter (SOLATIALKARAN; KHAJEH; ZARE, 2021).

Recently, more complex topologies have been proposed in the literature, including the LLCL filter. The LLCL filter provides improved harmonic attenuation at the switching frequency and a reduction in the total filter volume compared to the LCL filter (BUYUK et al., 2016). This topology is based on the insertion of an inductor in the LCL filter capacitor's branch, forming a series resonant circuit tuned at the switching frequency. One drawback of this topology is lower attenuation starting at frequencies close to twice the switching frequency, as reported in (GOMES; CUPERTINO; PEREIRA, 2018). However, this issue can be partially addressed by adding multiple series resonant branches as needed (BUYUK et al., 2016). Fig. 13 (d) and (e) depict the LLCL topology and the multi-branch topology, respectively.

Higher-order filters exhibit a resonance frequency, which may cause instability in the closed-loop system, as reported in Zhang et al. (2014). Numerous solutions to this problem have been proposed in the literature, including passive and active solutions (WU, W. et al., 2014). Passive damping involves the insertion of passive elements into the filter to reduce the system's resonant peak. In (PENA-ALZOLA; LISERRE; BLAABJERG; SEBASTIAN, et al., 2013), a tuning method for a series resistor in the capacitor branch is proposed. This passive damping tuning method can maintain control stability without compromising filter effectiveness. Active damping methods consist of modifications to control strategies to provide closed-loop damping (ZHANG et al., 2014). Active techniques are preferred as they avoid extra losses in passive components. However, active damping results in a more complex control system and may require additional sensors (BUYUK et al., 2016). In Twining and Holmes (2003) and Pena-Alzola, Liserre, Blaabjerg, Ordonez, et al. (2014), an LCL filter design with a robust multi-loop active damping technique based on capacitor current feedback is presented, using a proportional controller (k_c). Fig. 14 (a), and (b) and (c) illustrate passive and active damping techniques, respectively.

2.3 MI Design

In this section, it is explored the decision-making process behind the selection of a specific power electronics topology and control strategies for the implemented system. Each

Source: Own authorship.

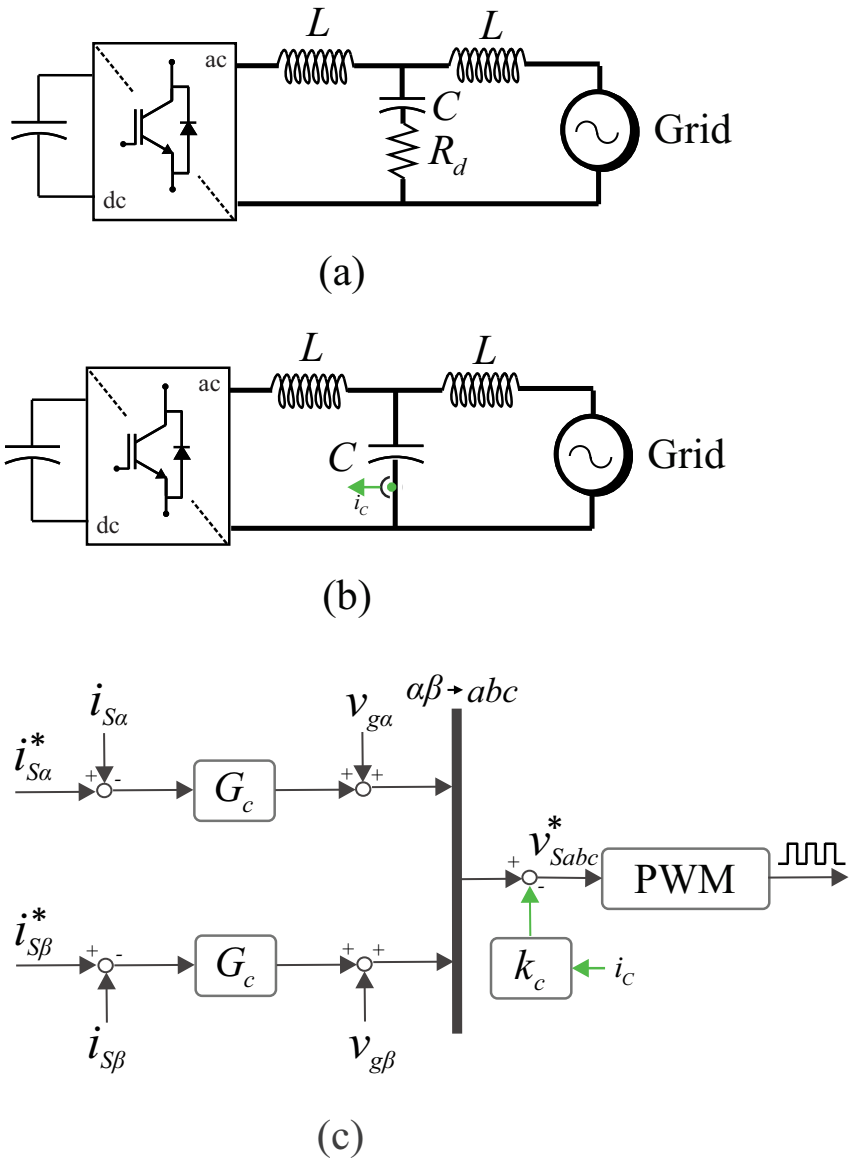

Figure 14 – Control structure: (a) Series resistor passive damping; and (b) and (c) capacitor current feedback active damping.

decision has been thoroughly considered and designed to enhance the overall functionality, and effectiveness of the system. In this work, it is adopted a three-phase single-stage topology, wherein a single interfacing inverter performs various functions, including maintaining the dc-link voltage at the level estimated by the MPPT algorithm, HCS, and injecting power into the grid.

The system comprises of a PV array, a dc-link capacitor, a VSI, and a LCL filter. It is worth mentioning that the investigation conducted in this thesis is equally applicable to a two-stage system that employs a VSI since the research is primarily focused on the grid-side. The VSI type is selected because it is the most extensively studied type of inverter, as mentioned previously. Additionally, the selection of the single-stage three-phase topology is based not only

on the power range requirements but also on the specific focus of this work's study, which is the grid-side. This topology aligns well with the research objectives and allows for a detailed analysis of grid-related performance.

The necessity for efficient harmonic mitigation and enhanced filtering performance led to the choice to include an LCL filter. Compared to other filter topologies, LCL filters provide better high-frequency harmonic attenuation and lower volume. Therefore, a LCL filter is employed to interface the system to the PCC and reduce high-frequency harmonics resulting from the inverter switching. The parameters of the LCL filter were determined based on the methodology proposed in Pena-Alzola, Liserre, Blaabjerg, Ordonez, et al. (2014), as described in Appendix B. Fig. 15 depicts the PV system topology under investigation in this work.

Source: Own authorship.

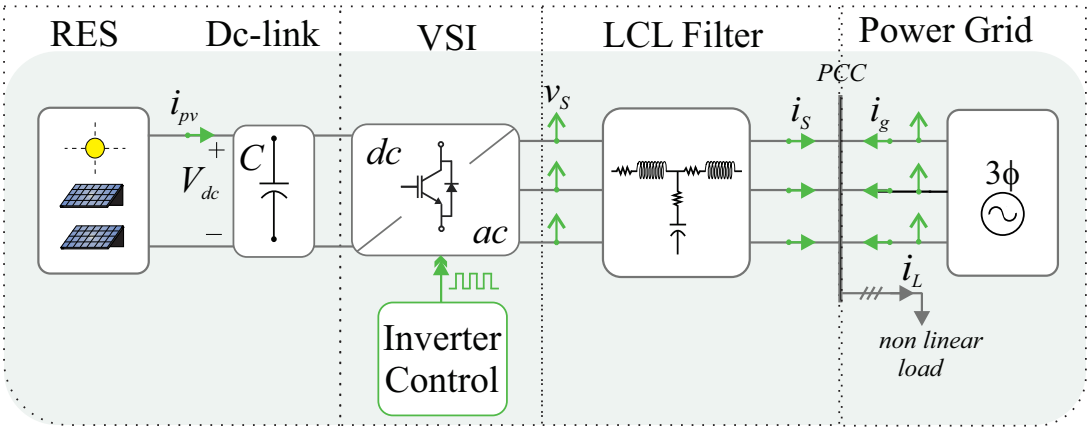

Figure 15 – Three-phase grid-connected photovoltaic system with output LCL filter.

The control strategy adopted is implemented in the stationary reference frame where it is employed a two-loop approach, with the inner loop control based on the measurement of grid-side current and the outer loop, responsible for the dc-link control, based on the V_{dc}^2 control as described in Yazdani and Iravani (2010). The parameters of the PV inverter are presented in Table 3, and the complete control structure is depicted in Fig. 16. The chosen parameters are defined to enable a proof of concept that takes into account the availability and restrictions encountered during the execution of this work.

The inner loop control regulates the current injected into the grid. The fundamental current references, $i'_{S\alpha}$ and $i'_{S\beta}$, are computed using the IPT based on the active (P^*) and reactive (Q^*) power references, as follows:

$$\begin{bmatrix} i'_{S\alpha} \\ i'_{S\beta} \end{bmatrix} = \frac{1}{v_\alpha^2 + v_\beta^2} \begin{bmatrix} v_\alpha & v_\beta \\ v_\beta & -v_\alpha \end{bmatrix} \begin{bmatrix} P^* \\ Q^* \end{bmatrix}. \tag{2.3}$$

When HCS is applied, the current reference of the inverter includes one or more harmonic components. In such scenarios, conventional control techniques using PI controllers are not

Table 3 – System Parameters.

Parameter	Value
Grid voltage (line to line) (v_g)	220 V
Grid frequency (f_n)	60 Hz
Maximum power (P_{max})	5 kW
Inverter rated current (I_m)	13.12 A
Switching frequency (f_s)	12 kHz
Filter inductances (L_f, L_g)	2.0 mH
Filter resistance (R_f, R_g)	128.6 mΩ
Filter capacitance (C_f)	20 μF
Damping resistor (R_d)	3.53 Ω
dc-link voltage (V_{dc})	370 V
Base power (S_b)	5 kW
Base voltage (V_b)	220 V
Base current (I_b)	13.12 A

Source: Own authorship.

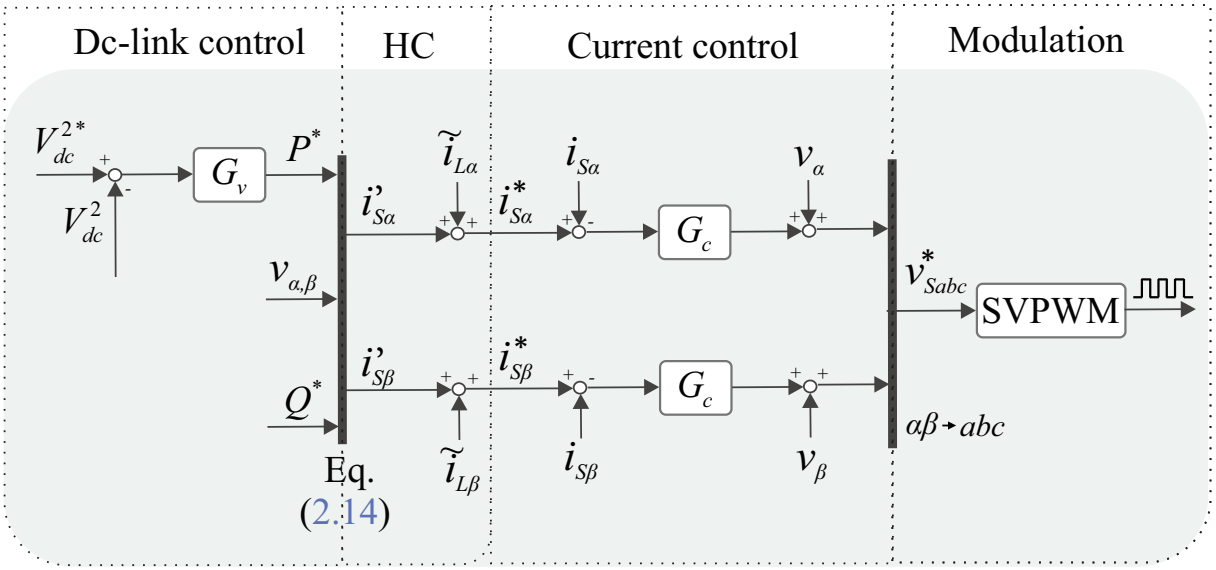

Figure 16 – Complete control structure.

suitable, as they exhibit some limitations such as the inability to follow non-sinusoidal references without steady-state error and limited disturbance rejection capacity at variable frequencies, as described in Yepes et al. (2011). To overcome these deficiencies, a resonant controller is utilized.

The current control is based on a Proportional Multi Resonant (PMR) controller, which comprises of a proportional controller and one or more resonant controllers, with one of the resonant controllers tuned to the fundamental frequency and the others tuned to the harmonic frequencies.

The PMR transfer function is given by:

$$G_c(s) = k_p + \sum_h G_R(s). \tag{2.4}$$

where k_p is the proportional gain and $G_R(s)$ is a resonant controller for each harmonic order h.

$$G_R(s) = \sum_h k_{ih} \frac{s}{s^2 + h^2\omega_f^2}. \tag{2.5}$$

where k_{ih} is the integral gain tuned at the harmonic order h and ω_f is the fundamental frequency. k_p and k_{ih} can be tuned as proposed in (YEPES et al., 2011).

The harmonic detection technique proposed in Watanabe, Akagi, and Aredes (2008) and described in Section 2.1.4 is employed in this work. The adoption of the instantaneous power theory for system control is driven by its ability to extract active, reactive, and harmonic powers on a cycle-by-cycle basis, enabling effective HCS. The chosen control reference frame, which offers a proper foundation for putting the necessary control techniques into practice, also has an impact on the choice of this detection technique. The fundamental components of the current are combined with the oscillating components, $\tilde{i}_{L\alpha}$ and $\tilde{i}_{L\beta}$, to generate the reference current for the inverter, $i^*_{S\alpha}$ and $i^*_{S\beta}$. Finally, the controller calculates the inverter modulation index (v^*_{abc}) and applies the Space Vector Pulse Width Modulation (SVPWM) algorithm to set the switch pulses of the inverter.

2.4 Chapter Conclusions

The decision to implement a three-phase single-stage system in this work emerged from a thorough analysis of the existing literature, technical considerations, and personal preference. The chosen configuration is considered appropriate for the study's objectives as it offers compatibility with a substantial part of existing research found in the literature. It is important to note that while the chosen three-phase single-stage system holds promise, this decision does not imply superiority over other topologies or control structures. The selected systems for examination will enable us to further investigate their performance characteristics, evaluate their effectiveness in addressing HCS, and explore potential improvements or enhancements. The subsequent chapters of the thesis will employ the described PV inverter topology to examine and assess the impact of HCS.

3 Operation Limits of Grid-Tied PV Inverters with HCS

The utilization of passive filters in the integration of PV systems with the power grid serves to mitigate high-frequency harmonics generated by the switching frequency of the converter (GOMES; CUPERTINO; PEREIRA, 2018). These filters must adhere to well-defined design specifications, including reactive absorption, voltage drop in inductive elements, total harmonic distortion (THD), and losses, among others (BERES et al., 2016; BUYUK et al., 2016; GOMES; CUPERTINO; PEREIRA, 2018). However, during multifunctional operation, the impact of HCS on these specifications can pose challenges. In particular, the voltage drop in passive filters may hinder the PV inverter's ability to compensate for nonlinear loads harmonic currents.

The design of the passive filter must account for two factors: limitations on the inverter current and restrictions imposed by the dc-link voltage. It is important to note that in this chapter, it is assumed the use of an ideal inductor, meaning that it is not consider nonlinear effects such as saturation and hysteresis that can occur in real-world inductors. However, in the next chapter, it is consider these effects and evaluate their impact on the capability curves.

It is imperative to ensure that the control strategy is appropriately designed to compensate the desired harmonic orders. A wide enough control bandwidth is necessary to cover the frequencies being controlled, as indicated by Liserre, Teodorescu, and Blaabjerg (2006). If the control bandwidth is not sufficient, instability may occur. Furthermore, according to Pena-Alzola, Liserre, Blaabjerg, Ordonez, et al. (2014), the resonance frequency of the filter should be positioned halfway between the control bandwidth and the switching frequency.

3.1 Limit imposed on the inverter rated current

The thermal stress on semiconductors is a crucial aspect to be taken into account during the design and operation of PV systems. It can negatively impact the performance and reliability of the semiconductor devices used in the system (ANDRESEN; LISERRE, 2014). This stress is caused by the heating of the devices due to electrical resistance and switching losses, leading to increased power loss and reduced efficiency (NOVAK; SANGWONGWANICH; BLAABJERG, 2021). The extent of thermal stress depends on various factors such as operating conditions, cooling system design, and thermal conductivity of the semiconductor materials (INFINEON, 2020).

In this thesis, the focus is on the impact of the current flowing through the semiconductors on the thermal stress in PV inverters, with the assumption that the other factors such as cooling system design, and material properties remain constant. Therefore, the current limitation is

important for the PV inverter safe operation. In MI, the synthesized current injected into the grid is given by:

$$i_S(t) = \sum_{h=1}^{+\infty} I_{Sh} \cos(h\omega_f t + \delta_{Ih}), \tag{3.1}$$

where h is the harmonic order, ω_f is the angular fundamental frequency, I_{Sh} is the current magnitude and δ_{Ih} is the current phase angle of the harmonic order h.

de Barros et al. (2018) present an analysis of the effect of HCS on the lifetime of a single-phase PV MI. The study considered the mission profile of harmonic current, irradiance and temperature to obtain a realistic estimation of the power losses and thermal stress on the semiconductors. The results show that the lifetime of the PV inverter depends on the harmonic order, phase angle, and amplitude.

Fig. 17 provides an illustration of the effects of different phase angles in the harmonic current. In this case, a 5^{th} harmonic current with an amplitude equal to 0.15 pu was added to a fundamental (60 Hz) waveform with an amplitude of 1 pu. In Fig. 17 - (a), the 5^{th} harmonic current has a 0º phase angle and the sum of these components results in a waveform with a peak value of 1.15 pu $(\hat{I}_S)$. However, in Fig. 17 - (b), the 5^{th} harmonic current has a phase angle of 180º, resulting in a peak value of 1 pu.

In summary, the presence of harmonics in the current flowing through the semiconductor devices in a VSI-type inverter can have impact on the losses in the system. Thus, it is imperative to ensure that both the average losses and the maximum stresses experienced by the semiconductors do not exceed their nominal values.

To preserve the integrity of the components the following restrictions must be ensured:

$$\begin{cases} \hat{I}_S \leq I_m \\ I_{rms} < \sqrt{{Irms_1}^2 + {Irms_3}^2 + ...{Irms_n}^2} \end{cases}, \tag{3.2}$$

where $\hat{I}_S$ is the peak value of Eq. (3.1), I_{rms} is the nominal rms value of the inverter and I_{rms_x} is the harmonic rms current of orders $x = 1, 3, 5n..., n$.

In this way, it is possible to ensure that the stress experienced by the semiconductors during HCS operation does not exceed that of the inverter's normal operation.

3.2 Limit imposed on the dc-link voltage

In this section, the assumption is made that the control possesses sufficient bandwidth to compensate the intended harmonic orders. Furthermore, the analysis is based on a balanced and symmetric three-phase system, and thus a per-phase analysis is conducted.

Source: Own authorship.

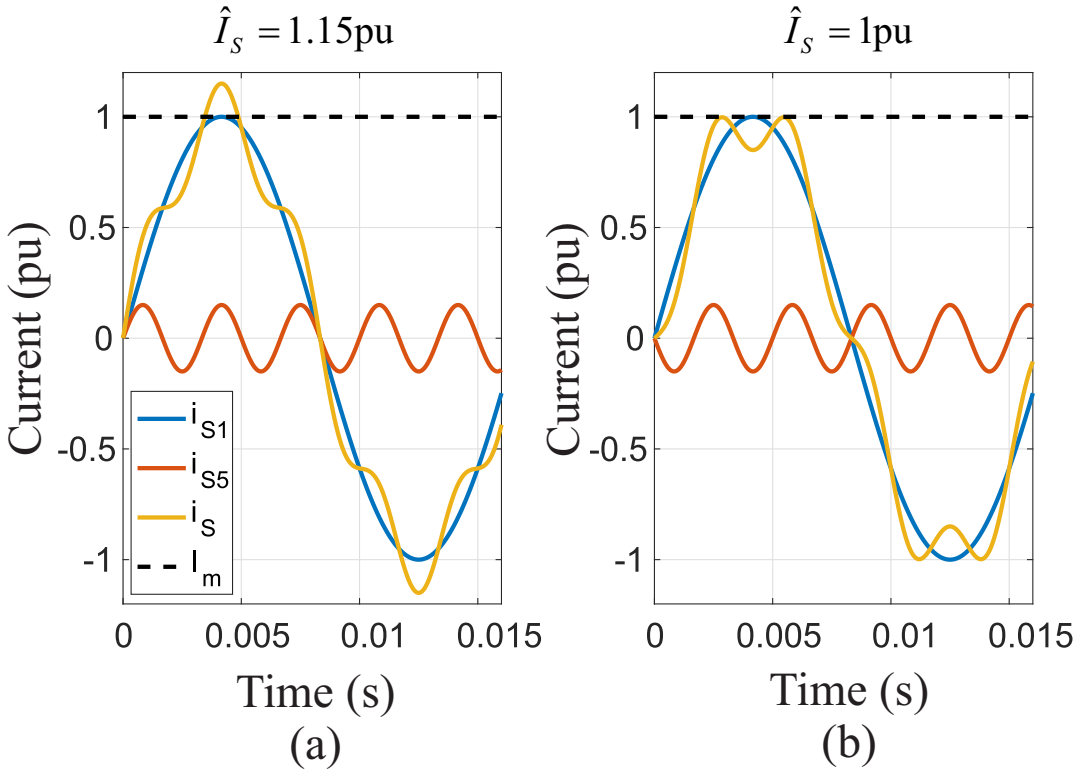

Figure 17 – Effect of different angles in the harmonic current. (a) $I_{S1} = 1$ pu, $\delta_{I1} = 0°$, $I_{S5} = 0.15$ pu and $\delta_{I5} = 0°$. (b) $I_{S1} = 1$ pu, $\delta_{I1} = 0°$, $I_{S5} = 0.15$ pu and $\delta_{I5} = 180°$.

The provision of HCS, may result in the inverter operating in the nonlinear region of modulation and injecting low-order harmonics into the grid (ADIB; LAMB; MIRAFZAL, 2019). Thus, an assessment of the required dc-link voltage for synthesizing the harmonic current is imperative to ensure that the photovoltaic inverter is operating in the linear region of modulation. Fig. 18 displays the equivalent LCL filter model per phase. The variables in the figure include: v_S, which represents the synthesized line-to-neutral voltage of the inverter; v_{gj}, which represents the grid line-to-neutral voltage; v_C, which represents the capacitor voltage; $Z_f = R_f + jX_f$, $Z_g = R_g + jX_g$, and $Z_c = -jX_c$ are the filter impedances; R_d represents the damping resistor; Z_{grid} represents the grid impedance; i_L and i_g represent the load and grid currents, respectively.

The synthesized voltage (v_S) is derived from the application of the superposition theorem and is a function of the magnitude and phase angle of the output current (I_{Sh} and δ_{Ih}, respectively), the harmonic order ($h = 1, 2, 3...$), the impedance of the LCL filter evaluated at the harmonic frequencies $(Z_{LCL}(h\omega_f))$, and the voltage at the PCC.

In order to determine the voltage drop across the LCL filter, it is crucial to comprehend the behavior of the filter during harmonic currents. As demonstrated in Fig. 18, the following transfer function can be derived:

Source: Own authorship.

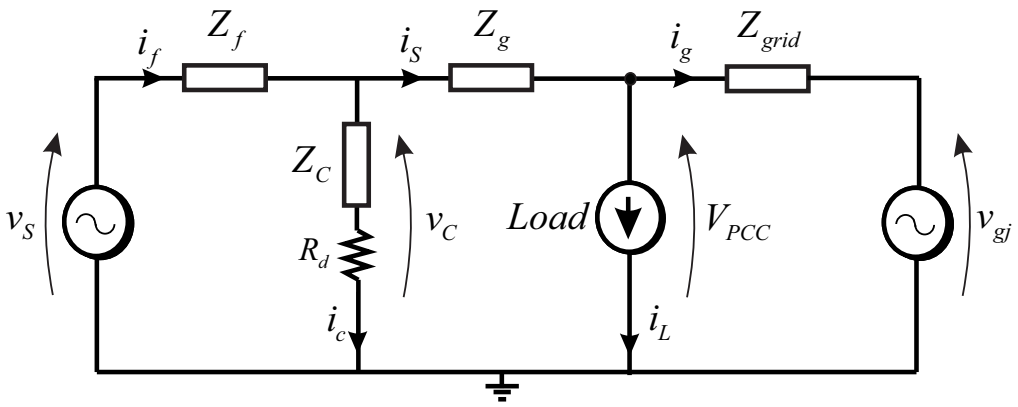

Figure 18 – Equivalent LCL filter circuit per phase.

$$Z_{LCL}(s) = \frac{V_S(s)}{i_S(s)} = \frac{as^3 + bs^2 + cs + R_f + R_g}{sC_fR_d + 1}, \tag{3.3}$$

where $a = C_fL_fL_g$, $b = C_f[L_f(R_d + R_g) + L_g(R_d + R_f)]$ and $c = [L_f + L_g + C_f(R_fR_d + R_fR_g + R_dR_g)]$.

The transfer function derived provides an expression for the output voltage as a function of the output current. The Bode diagram of the transfer function, as described in Eq. (3.3), is depicted in Fig. 19 and is based on the parameters listed in Table 3 presented in Chapter 2.

Source: Own authorship.

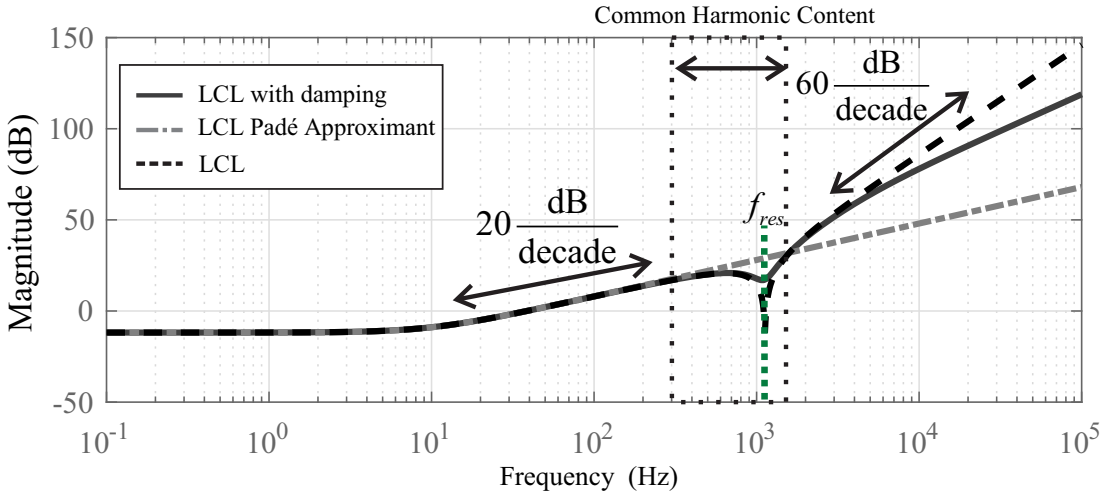

Figure 19 – LCL filter impedance bode diagram ($L_f = L_g = 2$ mH, $R_f = R_g = 128.6$ mΩ, $R_d = 1.8\Omega$, $C = 20\mu$F and $f_{res} = 1.125kHz$).

A resonant frequency (f_{res}) arises as a result of the characteristics of the LCL filter. As

depicted in Fig. 19, the impedance of the filter increases with frequency, due to its inductive component. Conversely, at lower frequency values, the impedance of the capacitor branch dominates, leading to behavior that resembles that of an L filter. To confirm and support this observation from an analytical perspective, the Padé approximant is utilized to obtain the low-frequency model of the transfer function described in Eq. (3.3).

The Padé approximant $p_{(n,m)}(x)$ to an analytic function $f(x)$ is a rational function $\frac{p(x)}{q(x)}$, where $p(x)$ is a polynomial of degree n and $q(x)$ is a polynomial of degree m (YANG et al., 2005). The Padé approximant has the same Taylor series expansion as $f(x)$ (YANG et al., 2005; GOMES; CUPERTINO; PEREIRA, 2018). Thus, the low-frequency approximation of the transfer function, taking into account the Padé approximant, is given by:

$$Z_{LCL}(s)|_{\omega \ll \omega_{res}} = s(L_f + L_g - C_f R_g^2) + R_f + R_g. \tag{3.4}$$

Since $C_f R_g^2 \ll L_f + L_g$,

$$Z_{LCL}(s)|_{\omega \ll \omega_{res}} \approx s(L_f + L_g) + R_f + R_g. \tag{3.5}$$

Fig. 19 depicts the LCL filter with a damping resistor and its approximation using the Padé method. The results in Fig. 19 demonstrate that the approximation is highly accurate for frequencies one decade below the resonance frequency.

Additionally, the authors in Liserre, Blaabjerg, and Hansen (2001) have concluded that the resonance frequency must lie within a certain range to prevent resonant issues in both the lower and upper regions of the harmonic spectrum, as follows:

$$10 f_n \leq f_{res} \leq 0.5 f_s, \tag{3.6}$$

where f_{resn} is the grid frequency, f_{res} is the filter resonance frequency and f_s is the switching frequency.

It is assumed that the resonance frequency falls within the arithmetic mean of the upper and lower boundaries defined in Eq. 3.6. Additionally, when the switching frequency is expressed as a function of the fundamental frequency, and the resonance frequency is allocated one decade above the desired harmonic order, the following expression results:

$$10 h f_n = \frac{10 f_n + 0.5 n_s f_n}{2}, \tag{3.7}$$

where n_s is the ratio between the switching and the fundamental frequency. Therefore,

$$h = \text{floor}\left(\frac{n_s + 20}{40}\right). \tag{3.8}$$

At a switching frequency of 12 kHz ($n_s = 200$), the results obtained from Eq. (3.8) indicate that the approximation provides good accuracy for the first five harmonic current components. Furthermore, it is crucial to ensure the availability of a minimum dc-link voltage value to facilitate power injection into the grid and HCS. This minimum voltage value is crucial to guarantee that the modulation operates within the linear region and is given by:

$$v_{Sh}\angle\delta_{Vh} = V_{PCCh} + Z_{LCL}(h\omega_f)I_{Sh}\angle\delta_{Ih}. \tag{3.9}$$

where V_{PCCh} is the PCC voltage for the harmonic order h. Its phase is assumed to be zero.

Based on the superposition theorem, the required voltage to HC is:

$$v_S(t) = \sum_{h=1}^{+\infty} V_{sh}\cos(h\omega_f t + \delta_{vh}). \tag{3.10}$$

Therefore, the minimum dc-link voltage is given by:

$$V_{dc_{min}} = \frac{2\hat{V}_S}{m} \tag{3.11}$$

where $\hat{V}_S = \max(v_S(t))$ is the synthesized peak voltage and m_i is the modulation index ($0 < m_i < 1$ to sinusoidal pulse width modulation (SPWM), $0 < m_i < 1.15$ to space vector PWM (SVPWM)).

Therefore, in order to ensure operation within the linear region of the modulation, the dc-link voltage must be maintained above the threshold value of $\frac{2\hat{V}_S}{m}$. This value represents the limit imposed by the dc-link voltage.

3.3 Capability curves

The capability curves of a grid-tied inverter define the operating limits of the system, based on its parameters. The methodology for generating the capability curves, which is based on the equations described in Section 3.2, is outlined in this section.

As shown by Eq. (3.9), the peak voltage synthesized by the inverter is dependent on various factors, including the grid voltage, the injected current amplitude and phase angles, and the filter impedance. As a result, it is difficult to obtain an analytical expression for this relationship. To address this, an iterative algorithm has been developed using the equations from Section 3.2, which determines the maximum harmonic current that can be synthesized by the inverter without exceeding the voltage and current limits.

The input information for the algorithm includes inverters power, which is used to calculate the current injected into the grid. The active power is related to the generation of the PV system, while the reactive power can be set based on a power factor compensation strategy or grid code requirement. The algorithm also requires information on the harmonic orders to be compensated, as each order causes a different voltage drop in the filter. The filter parameters, grid voltage, and dc-link voltage must also be specified. The steps of the algorithm are as follows, as shown in Fig. 20:

Source: Own authorship.

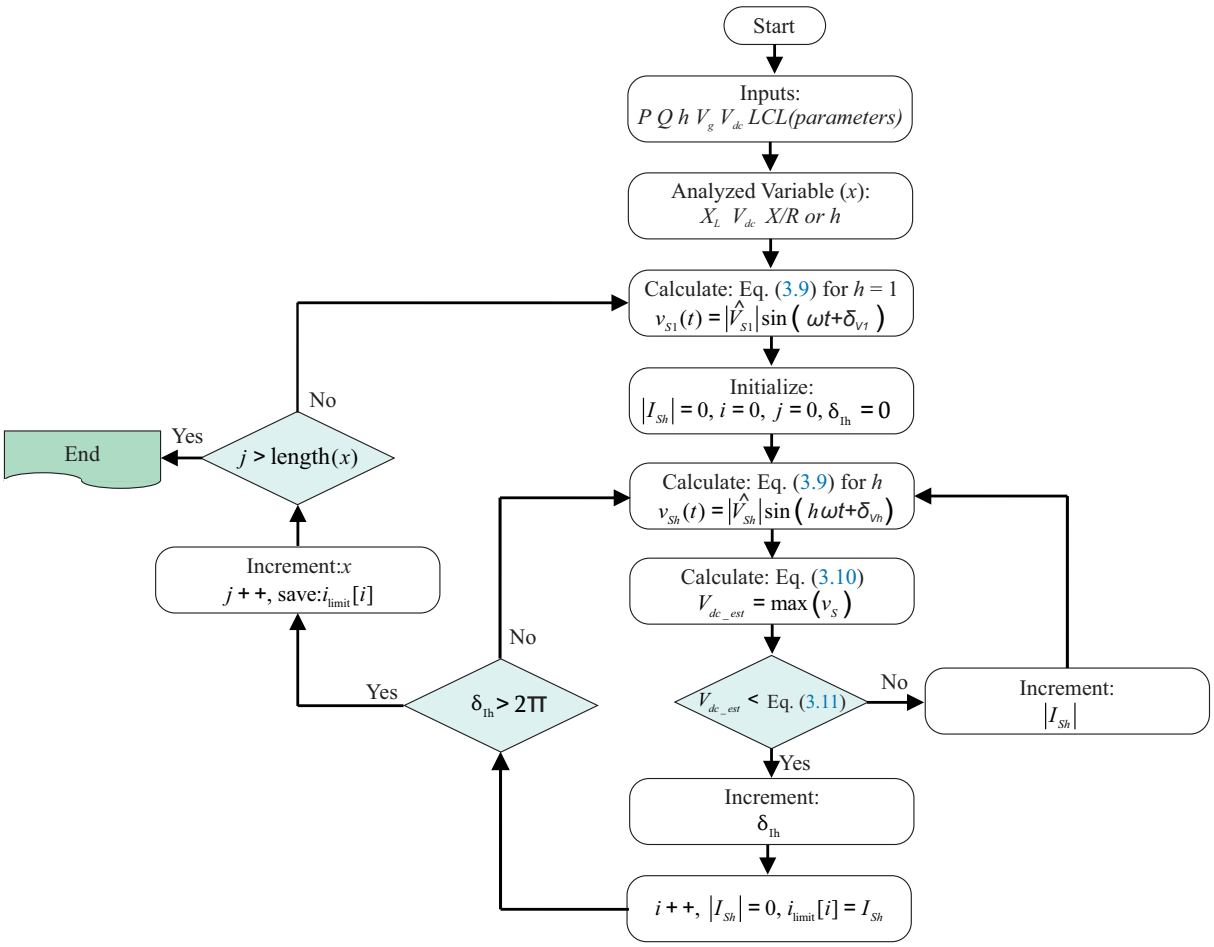

Figure 20 – HCL imposed by dc-link voltage algorithm flowchart diagram.

1. Calculate by Eq. (3.9), for $h = 1$, the necessary voltage to flow the specified active power to the grid;

2. An iteration increases the harmonic current amplitude and using Eqs. (3.9) and (3.10) until the stop condition to be satisfied;

3. The stop condition is the dc-link voltage value defined by Eq. (3.11) is equal or greater than V_{dc_est}. Where, V_{dc_est} is the estimated dc-link voltage value based on Eq. (3.10);

4. A new iteration is done for completing the saturation limits. The process needs to be repeated for each possible harmonic current angle;

5. Steps 2, 3 and 4 are repeated to complete the selected variable analysis: the dc-link voltage, the harmonic order or one of the LCL filter parameters. The stopping condition is determined by the size of the vector of the variable under analysis (x), which defines the number of iterations required to complete the process;

6. The algorithm output is a vector (i_{limit}) with the maximum harmonic current for each phase angle that can be synthesized without exceed the linear region of the modulation.

The necessary dc-link voltage calculated by the proposed algorithm, as a function of the compensated harmonic order and its phase angle, is displayed in Fig. 21. The system parameters listed in Table 3 are used, and the support of a 0.5 pu of harmonic current is demonstrated. It is seen that the necessary voltage may be up to 16% higher, depending on the angle of occurrence of the harmonic current. Additionally, as the impedance of the filter increases with frequency (due to its inductive nature), as shown in Fig. 19, higher-order harmonics demand higher voltages.

Source: Own authorship.

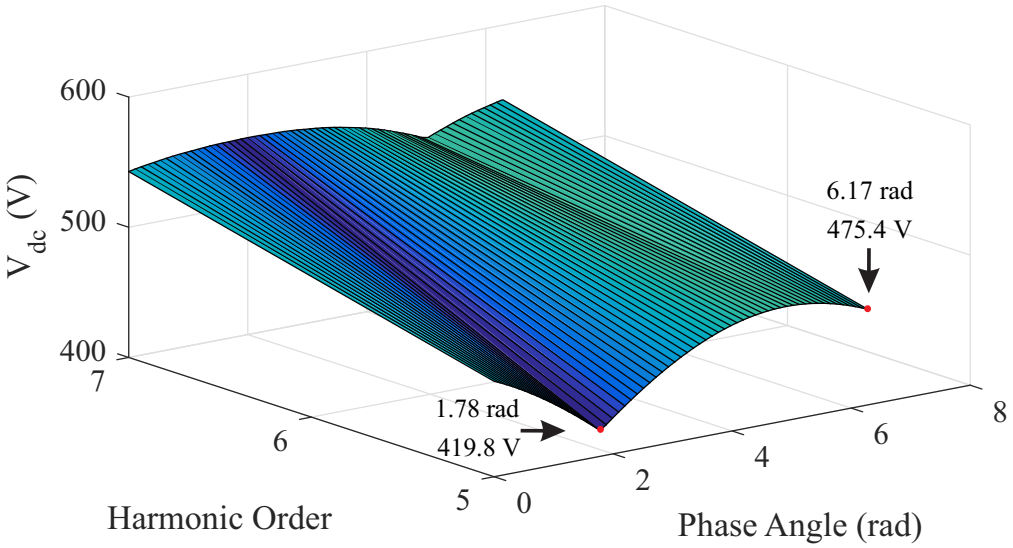

Figure 21 – Minimum dc-link voltage required to compensate 0.5 pu of harmonic current with different order (individually) and phase angles.

The developed algorithm can be modified to evaluate the support of two or more harmonic current orders, as specified in Eq. (3.10). The goal of this tool is to evaluate harmonic current profiles for support purposes. For instance, the synthesized voltage required for the 5^{th} and 7^{th} harmonic orders can be calculated as follows:

$$v_S(t) = V_{s1}\cos(\omega_f t + \delta_v) + V_{s5}\cos(5\omega_f t + \delta_{v5}) + V_{s7}\cos(7\omega_f t + \delta_{v7}) \tag{3.12}$$

Additionally, as reported in de Jesus et al. (2019), HCS can cause oscillations in the dc-link capacitor voltage, affecting the system's support capability. Fig. 22 presents an example of dc-link oscillation due to HCS for a 5^{th} harmonic order current. At 0.5 seconds, the HCS begins and it becomes noticeable that the oscillation is caused by the injection of harmonic current.

Source: Own authorship.

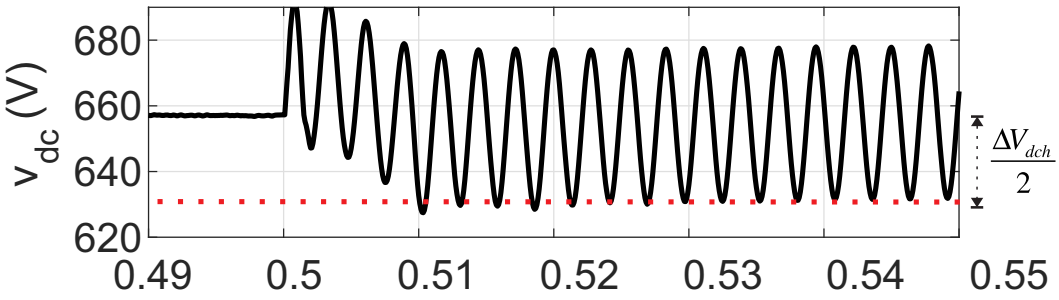

Figure 22 – Dc-link voltage oscillation example due to 5^{th} harmonic order current support. Source: (DE JESUS et al., 2019)

It is important to note that the voltage oscillation reduces the total utilization of the dc link by half of the oscillation caused by HCS. To account for this effect, the harmonic limit imposed by the dc-link voltage algorithm presented takes this into consideration. The voltage ripple for each harmonic order in Eq. 3.10 is, as reported in de Jesus et al. (2019), expressed as follows:

$$\Delta V_{dch} = V_{dc}(k_{max} - 1) \tag{3.13}$$

ΔV_{dch} is expressed in peak voltage values. And,

$$k_{max} = \sqrt{1 + \frac{3m_i}{2\omega_f C}\frac{I_{Sh}^{\pm}}{(h \mp 1)}\frac{1}{V_{dc}}} \tag{3.14}$$

where m_i is the modulation index, $I_{Sh}^{\pm}$ are the current peak value positive or negative sequence. The superscript $\pm$ and the $\mp$ signal in the Eq. 3.14 are determined by the harmonic order sequence. Additionally, it is important to note that the frequency of the oscillation triggered by HCS relies on the compensated harmonic order, whereby negative sequence harmonics induce oscillations of $(h+1)\omega_f$, while positive sequence ones trigger oscillations of $(h-1)\omega_f$.

Moreover, the estimated dc-link voltage is given by:

$$V_{dc_{est}} = \frac{2\hat{V}_S}{m} + \frac{|\sum_{h=2}^{\infty} \Delta V_{dch} cos(h\omega_f)|}{2} \tag{3.15}$$

The modified algorithm for the analysis of HCS is as follows:

- Representing multiple harmonic orders graphically can be difficult due to the different possible phase angles for each order. The proposed algorithm searches for the most restrictive phase angle to perform the analysis.
- Since the algorithm evaluates a harmonic profile, the harmonic amplitudes are fixed. The concern is if the system can compensate the specified profile.
- For each harmonic order, the dc-link voltage oscillation caused is calculated using the worst-case scenario phase angle.
- If the estimated dc-link voltage (given by Eq. 3.15) is higher than the rated dc-link voltage, the harmonic current profile cannot be compensated in that specific setup. In such cases, the designer must choose between partially or selectively compensating the targeted harmonic profile, or redefining the filter parameters in an attempt to achieve complete compensation.

Additionally, an algorithm has also been developed to determine the maximum harmonic current that can be synthesized without exceeding the inverter current limit. This algorithm operates similarly to the dc-link voltage limit imposed by the algorithm. For each possible angle value of the harmonic current, an iteration is made. The first step is to calculate the fundamental current flowing into the grid. Then, the module of the current is incrementally increased and Eq. (3.1) is calculated until the stop condition is satisfied. The stop condition in this case is the inverter's rated current. The flowchart for the algorithm is presented in Fig. 23.

The developed algorithms determine the constraints imposed by the dc-link voltage and current separately, allowing for a clearer understanding of the limitations of grid-tied inverters. This separation is particularly useful when considering the constraints for the design of multifunctional converters. However, grid-tied inverters must comply with both current and voltage limitations at the same time, resulting in a unique capability curve, which will be demonstrated in the results of subsequent sections.

3.4 Simulation results

The algorithms described in the flowcharts shown in Figs. 20 and 23 are implemented using MATLAB software. This approach is useful to provide a comprehensive understanding of the limitations of the grid-tied inverters and the resulting capability curves, which can be used to guide the design and implementation of multifunctional converters.

Source: Own authorship.

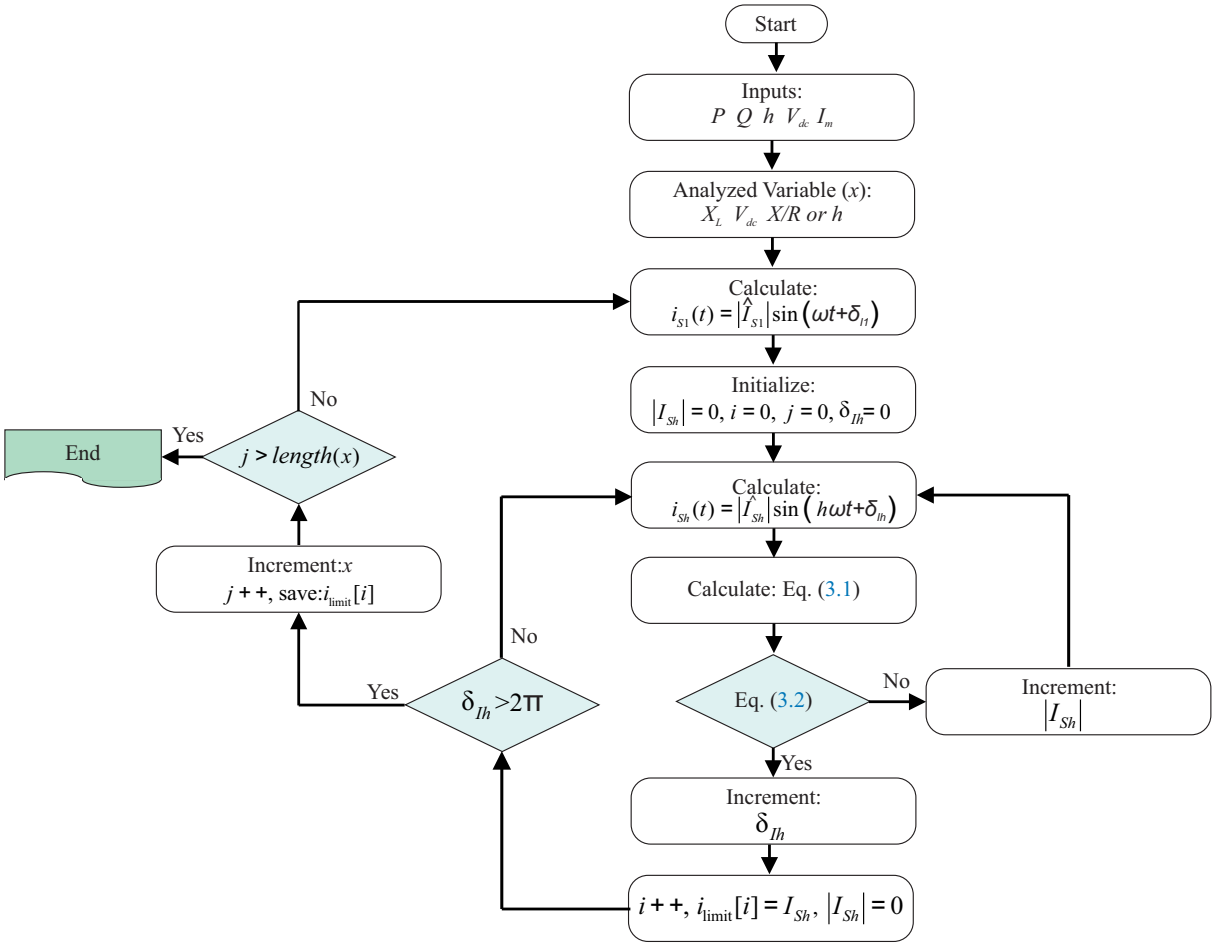

Figure 23 – HCL imposed by rated current algorithm flowchart diagram.

3.4.1 Capability Curve Representation

Fig. 24 presents the results obtained from the implemented algorithms using the parameters listed in Table 3. The scenario considered involves injecting an active power of 0.7 pu into the grid, and evaluating the 5^{th} harmonic current injection. The dependence on the harmonic current phase is such that the capability curves can be plotted on a polar diagram, where the distance from the origin represents the maximum harmonic peak current (I_{Sh}) that can be compensated, and the angle (δ_{Ih}) represents the harmonic phase. The units are expressed in per-unit (pu), with the base current equal to the rated current of the inverter (I_m).

There is an intersection between the HCL imposed by the dc-link voltage and the HCL imposed by the rated current. In this case, the actual capability curve of HCS is the area within the intersection of these two curves, as highlighted in red in Fig. 24. It can be seen that the harmonic current angle has a significant influence on the harmonic amplitude that can be synthesized. Two examples are indicated: Example ①, where the harmonic current injection has an angle of 120º and is limited by the rated inverter current; and Example ②, where the harmonic current injection has a phase angle of 180º and is limited by the dc-link voltage. In both cases, the

maximum 5^{th} harmonic current that can be injected is around 0.35 pu. However, in Example 2, if the dc-link voltage was not a constraint, the injected current would be 63% higher and limited by the rated inverter current (dashed black line).

Source: Own authorship.

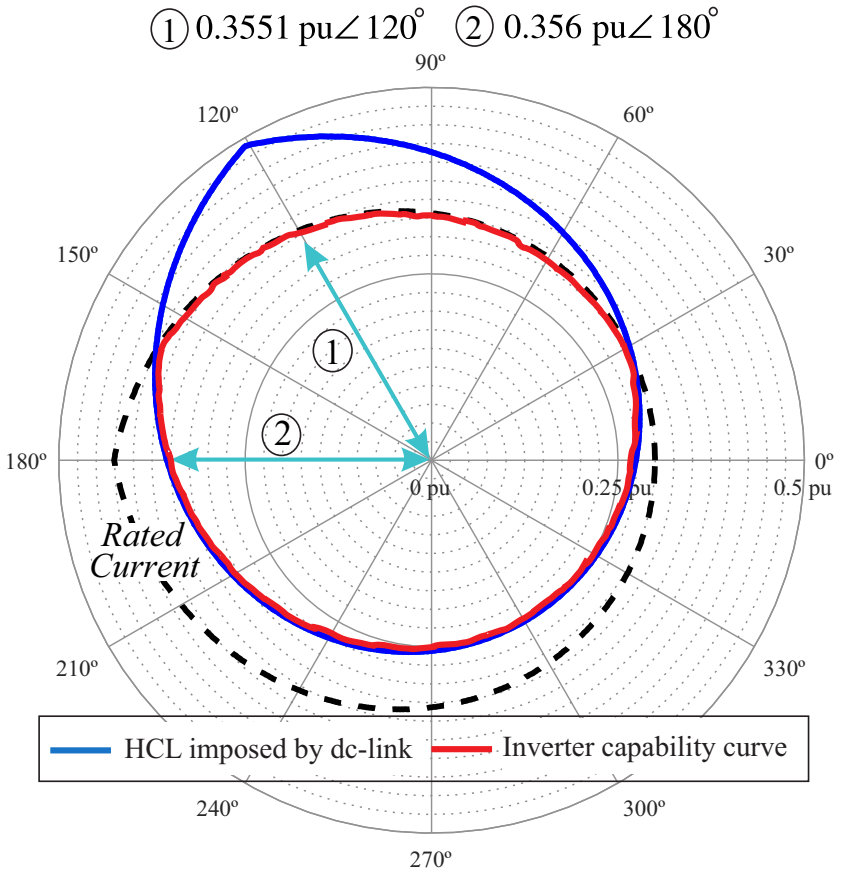

Figure 24 – Inverter capability curves for HCL imposed by dc-link voltage (colored lines) and HCL imposed by rated current (dashed black line). (0.7 pu of active power and the 5^{th} harmonic current injection)

The capability curves obtained in this manner can be utilized to determine the limits of support for each harmonic order in a PV system, while varying the injected active power. Additionally, they can also assist in defining the dc-link voltage design, ensuring that the synthesized voltage will never be more limiting than the rated current of the inverter. An example of specifying the dc-link voltage under multiple harmonic current orders is presented in the following section.

3.4.2 Parameter Variation Sensitivity

An important aspect that must be analyzed is how variations in the parameters of the PV system may affect its ability to compensate harmonic currents. Thus, in this section, the effects of variations in harmonic order, dc-link voltage, and filter passive elements (damping resistor, capacitor, inductor, and X/R ratio) are analyzed. To isolate the individual effects, the

other parameters are kept constant, as shown in Table 3. All results in this section consider an active power injection of 0.7 pu.

First, the effect of the harmonic order is analyzed. Fig. 25 presents the results obtained from varying the harmonic order on the capability curve. Four harmonic orders were considered: 5^{th}, 7^{th}, 11^{th}, and 13^{th}. It is noticeable that the higher the harmonic order synthesized by the inverter, the greater the HCL imposed by the dc-link voltage (colored lines). The HCL imposed by the dc-link voltage for the 13^{th} harmonic order is approximately 5.7 times greater than that for the 5^{th} harmonic order. Furthermore, in this case, for the 7^{th}, 11^{th}, and 13^{th} harmonic orders, the dc-link voltage is solely responsible for HCL as these curves are contained within the HCL imposed by the rated current. This is expected, as the results obtained from the Bode diagram in Fig. 19 demonstrate that the filter output impedance increases with frequency. Additionally, the equivalent LCL filter impedance phase angle changes with frequency, hence the angle resulting in the maximum harmonic current injection is different for each harmonic order.

Source: Own authorship.

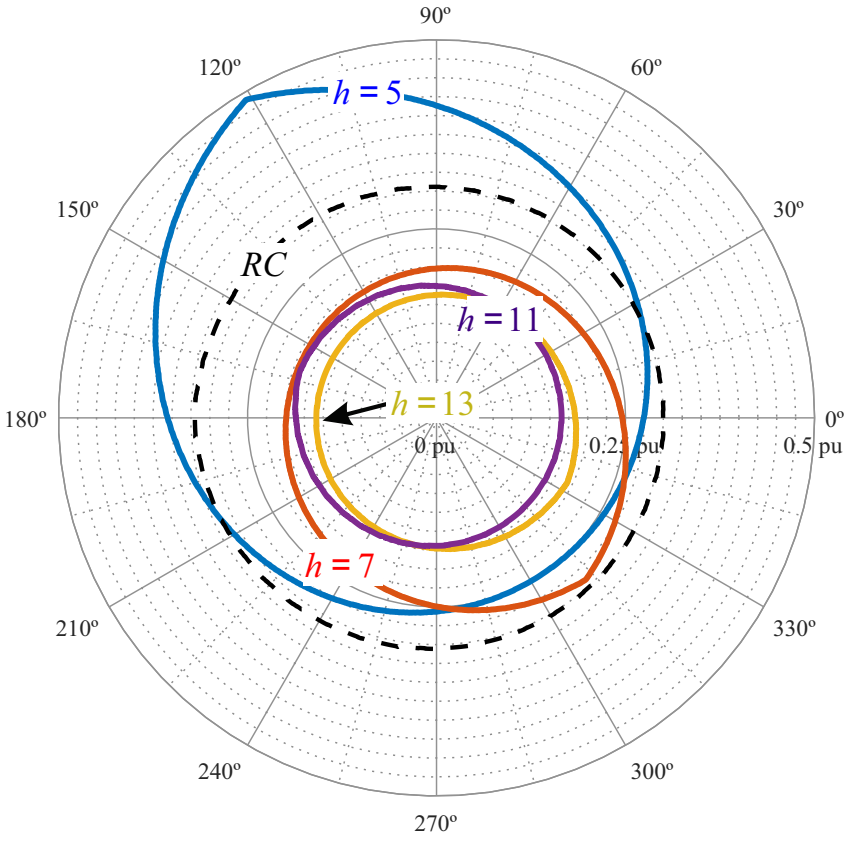

Figure 25 – Harmonic order variation effects in the capability curve. (HCL imposed by rated current (dashed black line) and HCL imposed by dc-link voltage(colored lines)). (0.7 pu of active power)

The variation in the dc-link voltage is also analyzed. The variation occurred in a range of 87% to 104%, in steps of 20 V, of the rated dc-link voltage value for a 5^{th} harmonic current injection. Fig. 26 shows that an increase in the dc-link voltage allows a higher amplitude of

harmonic current to be injected into the grid. The voltage drop across the filter has a linear increase with the current injected into the grid, as established by Ohm's law. The increase in the dc-link voltage will also behave linearly with the HCL. Comparatively, it is possible to inject approximately 16% more 5^{th} harmonic current with an increase of 4% in the nominal dc-link voltage. Usually, in commercial inverters, there is a limit for the dc-link voltage, since higher voltage values affects the inverter costs, increases the switching losses and consequently decreases the system efficiency (BIERHOFF; FUCHS, 2004; CALLEGARI; CUPERTINO; FERREIRA; BRITO, et al., 2019; CALLEGARI; CUPERTINO; FERREIRA; PEREIRA, 2021). Additionally, according to Backlund et al. (2009) there are three voltage ratings to be considered: the dc-voltage which determines the cosmic radiation failure rate and the long-term leakage current stability, the repetitive overshoot voltage spikes during turn-off and the maximum switching voltage to guarantee the safe operation area.

Source: Own authorship.

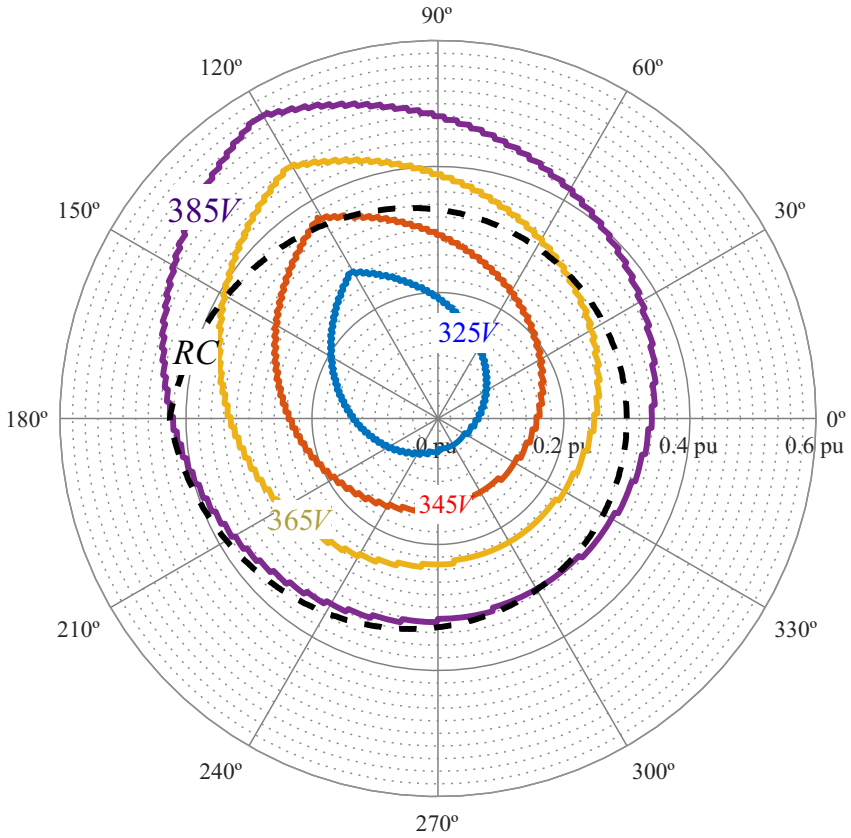

Figure 26 – Dc-link voltage variation effects in the capability curve for 5^{th} order harmonic current. (HCL imposed by rated current (dashed black line) and HCL imposed by dc-link voltage(colored lines)). (0.7 pu of active power and the 5^{th} harmonic current injection)

There are several LCL filter design methods presented in literature, author in Liserre, Blaabjerg, and Dell Aquila (2004) affirm that the total filter inductance value can vary between a minimum and a maximum value. In general, the total inductance value is limited to 0.1 pu in

order to limit the voltage drop as larger inductances will imply in larger dc-link voltages that will increase significantly the switching losses of the power converter. On the other hand, the minimum filter inductance is determined based on the maximum acceptable current Total Harmonic Distortion (THD). In Kouchaki and Nymand (2018), the authors considers the converter current ripple as a definition parameter. Therefore, the effect of inductance variation is analyzed under three conditions: the minimum calculated value (0.025 pu), the maximum value relative to the filter voltage drop (0.1 pu), and the value available in the experimental setup (0.16 pu). Fig. 27 shows the results for a 5^{th} harmonic current injection. As seen, even with inductance values within the limits set for the filter design, there is a significant variation in the HCL imposed by the dc-link voltage (approximately 40% between the minimum and maximum values of inductance as designed in Liserre, Blaabjerg, and Dell Aquila (2004)).

Source: Own authorship.

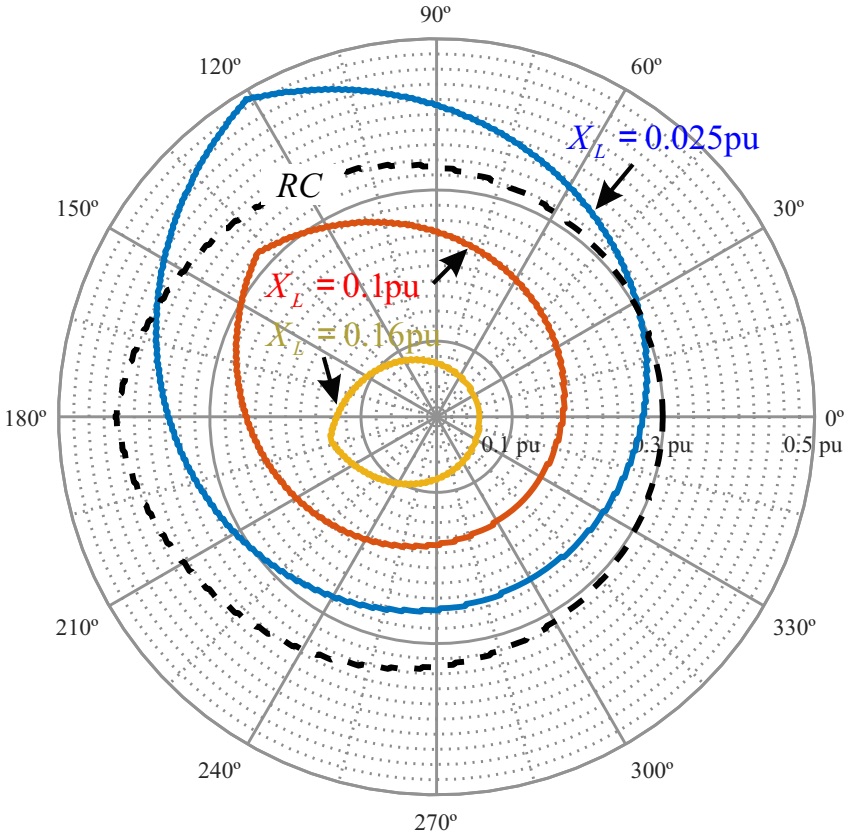

Figure 27 – Inductive reactance variation effects in the capability curve for a 5^{th} harmonic current injection. (HCL imposed by rated current (dashed black line) and HCL imposed by dc-link voltage(colored lines)). (0.7 pu of active power)

Another parameter analyzed is the X/R ratio of the inductors calculated at the fundamental frequency. Although the LCL filter inductors are designed to have low losses, it is important to determine the impact of this parameter on the inverter's capability. The ratio is varied between 5 and 40. Fig. 28 shows the result obtained from the variation in the X/R ratio effect on the injection of a 5^{th}-order harmonic current. It can be seen that there is only a small variation ($<5\%$)

in the capability to inject the harmonic current for the tested minimum and maximum values of the X/R ratio. As a result, this parameter can be considered insignificant.

Source: Own authorship.

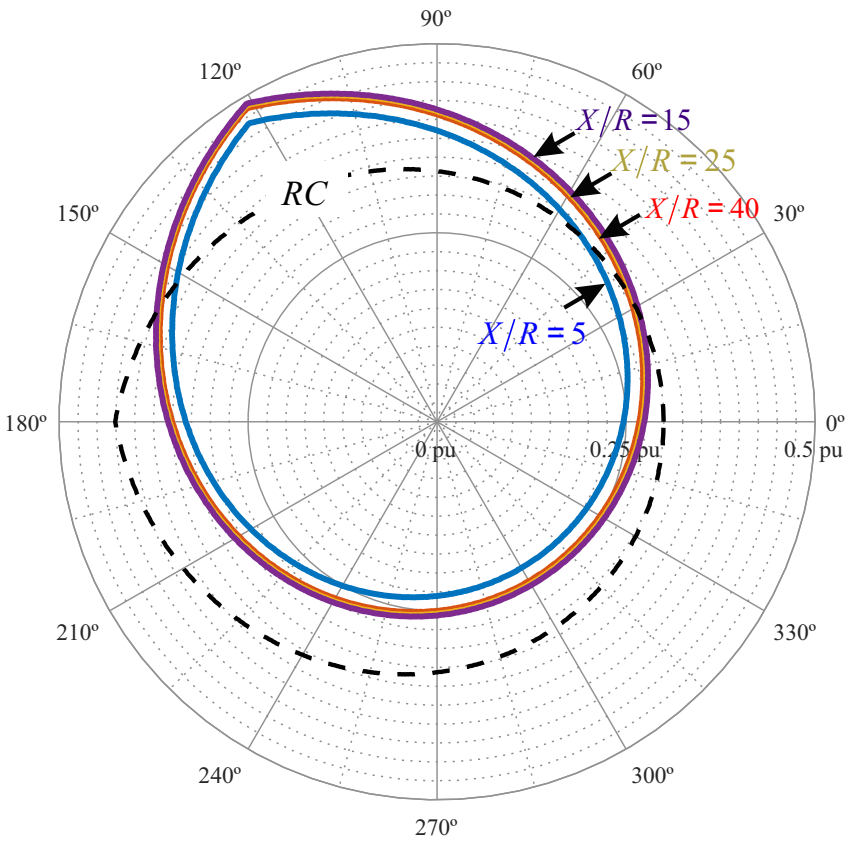

Figure 28 – X/R ratio variation effects in the capability curve for a 5^{th} harmonic current injection. (HCL imposed by rated current (dashed black line) and HCL imposed by dc-link voltage(colored lines)). (0.7 pu of active power)

Fig. 29 shows a comparison between an LCL filter and a filter neglecting the capacitor branch (Padé approximant). When assessing the 5^{th} harmonic injection, a 7.3% error is observed in the capability curve when the capacitor branch is neglected. However, for the 17^{th} harmonic order current injection, a 233% error occurs. It is worth noting that the 17^{th} harmonic order selected is only for the purpose of comparison, as its frequency is already very close to the upper limit of the control bandwidth. According to Eq. (3.8), with a switching frequency of 12 kHz, the accuracy of the Padé approximant is only valid up to the 5^{th} harmonic. This is mostly due to the harmonic current frequency range, as capacitors tend to have high reactance at lower frequencies. Also, in this tested case, the resonance frequency of the filter is very close to the 17^{th} harmonic order frequency and thus has a higher influence.

In general, the harmonic current capability analysis involves evaluating the resonance frequency of the LCL filter. If the resonance frequency is placed far away from the common harmonic content, the LCL filter can be approximated by an L filter with its inductance equal to the sum of the inductances of the LCL filter.

Source: Own authorship.

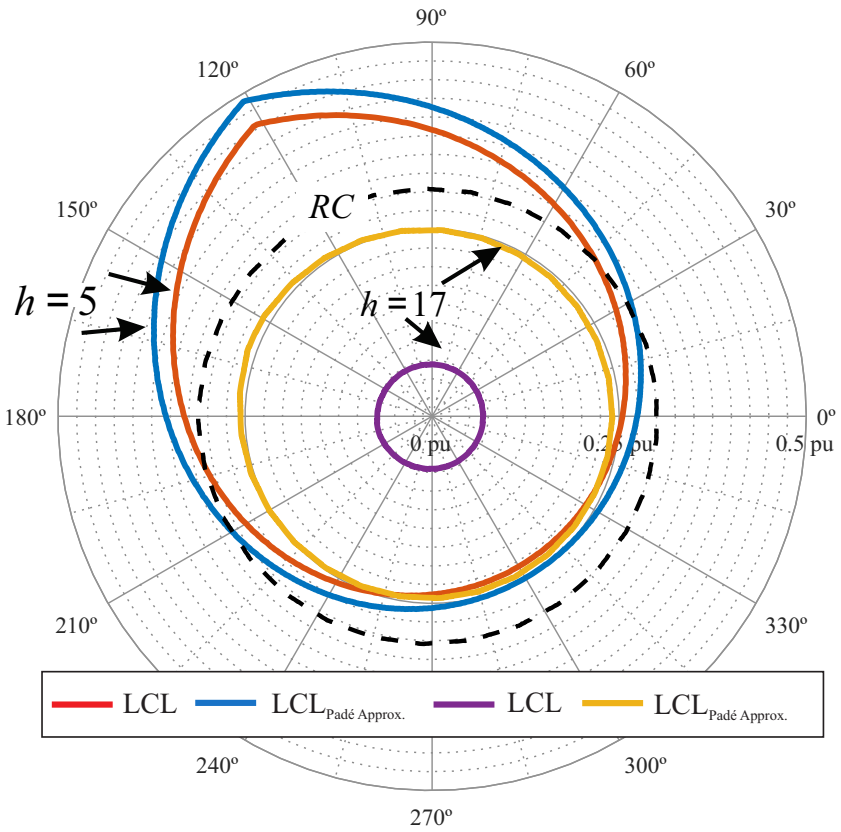

Figure 29 – Capacitance variation effects in the capability curve. (HCL imposed by rated current (dashed black line) and HCL imposed by dc-link voltage(colored lines)). (0.7 pu of active power)

The impact of the damping resistor on the injection of harmonic current is also analyzed. The variation was observed in a range from zero to the recommended value for the damping resistor (which is approximately 20% of the capacitor impedance value at the resonance frequency) according to references Liserre, Blaabjerg, and Hansen (2001) and Pena-Alzola, Liserre, Blaabjerg, Sebastian, et al. (2013). However, during the range of variation tested, the damping resistor had no significant impact on the injection of harmonic current. As a result, this finding is not presented. The purpose of the damping resistor is to absorb a portion of the switching frequency ripple to prevent resonance. Additionally, the high impedance of the capacitor, due to the frequency of HCS from nonlinear loads, results in a low current in the damping branch.

The following conclusions can be stated based on the obtained results:

- The increase of the dc-link voltage has a linear effect in the HCL, i.e., the higher the voltage, the higher the HC capability. However, the maximum dc-link voltage is limited by the maximum semiconductors and capacitors rated voltages;
- The damping resistor has no considerable effect in the harmonic current injection capability;

- The capacitor effects are dependent on the proximity between the harmonic current frequency and the LCL resonance frequency, Eq. (3.8). For higher frequency harmonics (780 to 1140 Hz) a more accurate result would be achieved considering the capacitor reactance;
- X/R ratio has a small impact in the capability curve and may be neglected;
- The inductance is mainly responsible for the limitation of harmonic current injection.

3.5 Experimental results

An experimental setup was assembled to validate the algorithms developed in this work. The implemented system consists of a three-phase single-stage inverter, as shown in Fig. 15. The parameters of the experimental system are presented in Table 4. The system control is implemented using the eZdsp F28335 kit from Spectrum Digital and the TMS320F28335 digital signal processor. In order to ensure controlled and reproducible results, a programmable voltage source was used instead of a photovoltaic array. An overview of the experimental setup is presented in Fig. 30.

Table 4 – Parameters of the Experimental System.

Parameter	Value
Maximum power (P_{max})	5 kW
Grid voltage (V_g)	220 V
Grid frequency (f_n)	60 Hz
Switching frequency (f_s)	12 kHz
Filter inductance (L_f, L_g)	2.0 mH
Filter resistance (R_f, R_g)	128.6 mΩ

3.5.1 Algorithms validation

Initially, for the experimental results, the PV inverter is set to inject the 5^{th} and 7^{th} harmonic order currents separately. The dc-link voltage is controlled at 375 V. For both harmonic order currents, the angle is varied from 0 to 360° with a 45° step. For each angle, the harmonic current is initially set to 0 A and gradually increased until the limit imposed by the dc-link voltage is reached. The limit imposed by the dc-link voltage is obtained by measuring the maximum amplitude of the reference signal sent to the PWM. Throughout the tests, a 4 A fundamental peak current per phase is maintained. The HCL imposed by the rated current is omitted in both figures since it does not represent any limitation at the presented conditions.

An energy quality analyzer (Fluke 435-II) and an oscilloscope (Tektronix TPS 2024) were used to measure the synthesized voltage level and voltage grid distortion. The quality

Source: Own authorship.

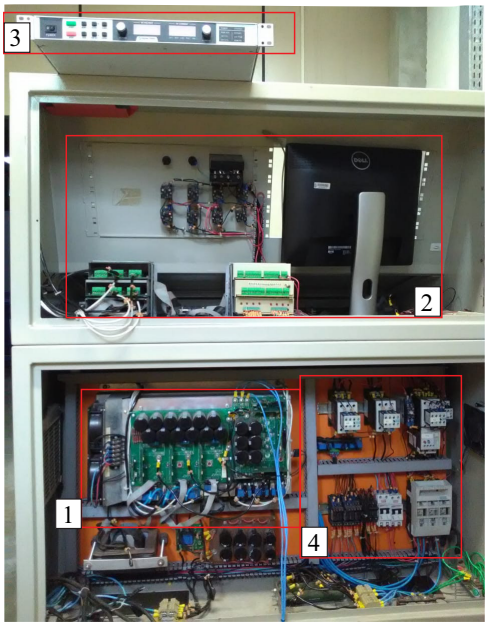

Figure 30 – Experimental prototype. 1 - power inverter, 2 - control system and interface board, 3 - controllable dc voltage source and 4 - command and protection circuits.

analyzer provides the distortion to be used as the input information for the algorithm. The voltage total harmonic distortion measured was 3.5%, with amplitudes of 3.8 V and 2.5 V for the 5^{th} and 7^{th} harmonic orders, respectively. The voltage level and distortion information were used to obtain more reliable results when evaluating Eq. 3.9.

First, the effect of the harmonic order is validated by considering the 5^{th} and 7^{th} harmonic orders. Fig. 31 presents the experimental results for the harmonic order variation. In the second test, the system is set to control the dc-link voltage at two different levels (365 V and 375 V) while compensating the 5^{th} harmonic order currents with the same angles as in the previous result. Results for the test are presented in Fig. 32.

The colored points in Figs. 31 and 32 closely approximate the theoretical results. It can be seen that the experimental results have the same behavior as the developed algorithm. Upon analyzing the results for the 7^{th} harmonic at 270°, it is observed that there is a deviation of 0.03 pu between the experimental and theoretical values. This deviation represents an error of around 20% or an absolute current value of 0.39 A. Considering the size of this error, it is difficult to pinpoint a specific source, particularly since only two particular points in the experiment displayed higher errors. Nevertheless, a general observation reveals that the experimental results verify the algorithms developed in this work.

Source: Own authorship.

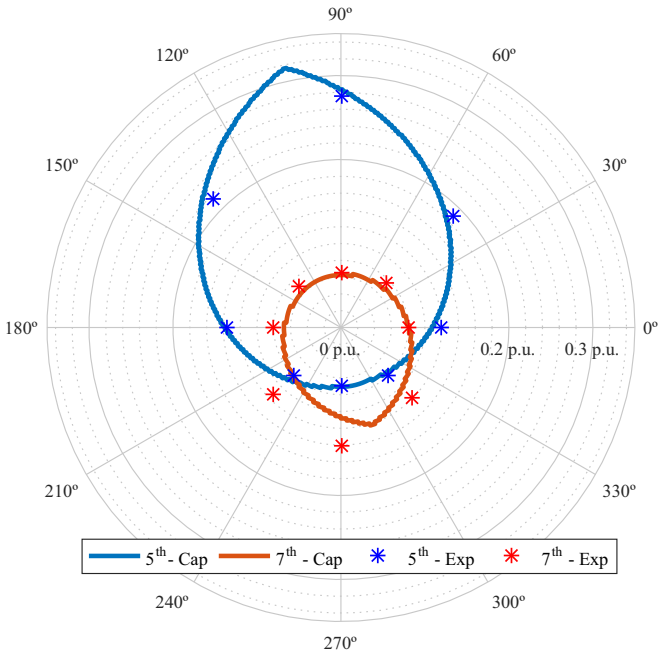

Figure 31 – Comparison between inverter capability curve (Cap) and experimental results (Exp) for 5^{th} and 7^{th} HCS. *Remark*: The base current is 13.12 A.

Source: Own authorship.

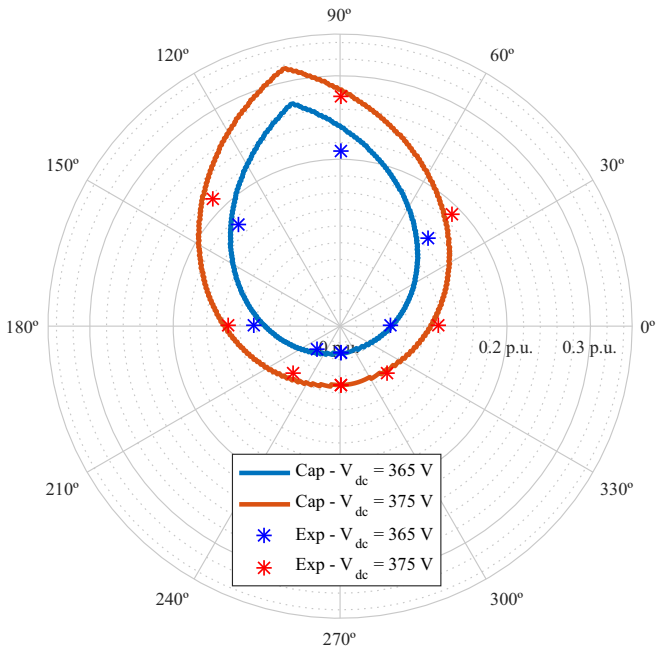

Figure 32 – Comparison between inverter capability curve and experimental results for 5^{th} HCS and variation in the dc-link voltage.

3.5.2 Performance under multiple harmonic current orders

The developed algorithm has also been validated for multiple harmonic orders as presented in Eq. (3.12). Different combinations of the fundamental current, 5^{th}, and 7^{th} harmonic orders have been tested. Three testing conditions were used:

Source: Own authorship.

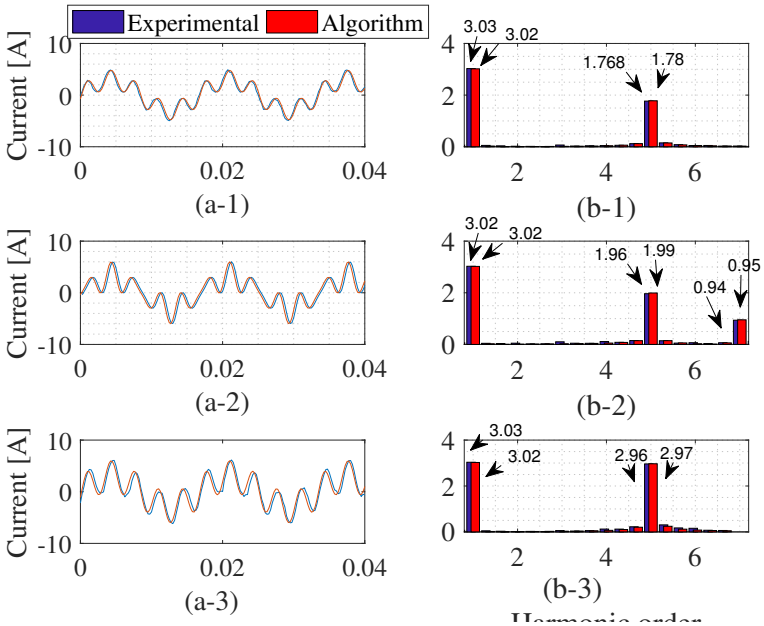

Figure 33 – Synthesized current for the first, second and third conditions in (a-1), (a-2) and (a-3), respectively. And its respective harmonic spectrum in (b-1), (b-2) and (b-3). *Remark*: Experimental data loaded from the DSP.

- First condition: 3 A fundamental current and 2 A 5^{th} harmonic order current, all with $0°$ phase angle.
- Second condition: 3 A fundamental current, $0°$ phase angle, 2 A 5^{th} harmonic order current, $0°$ phase angle and 1 A 7^{th} harmonic order current, $90°$ phase angle.
- Third condition: 3 A fundamental current, $45°$ phase angle and 3 A 5^{th} harmonic order current, $45°$ phase angle.

The synthesized current and reference voltage for modulation were experimentally acquired and compared with the algorithm's output. As seen in Figures 33 and 34, the algorithm's estimation shows good agreement with the experimental results.

These are valuable results, as with knowledge of the harmonic load characteristics, it is possible to estimate the minimum required dc-link voltage to compensate for harmonic currents without overmodulation. Using the tested conditions as an example, the following synthesized peak voltage and the respective required dc-link voltage are:

Source: Own authorship.

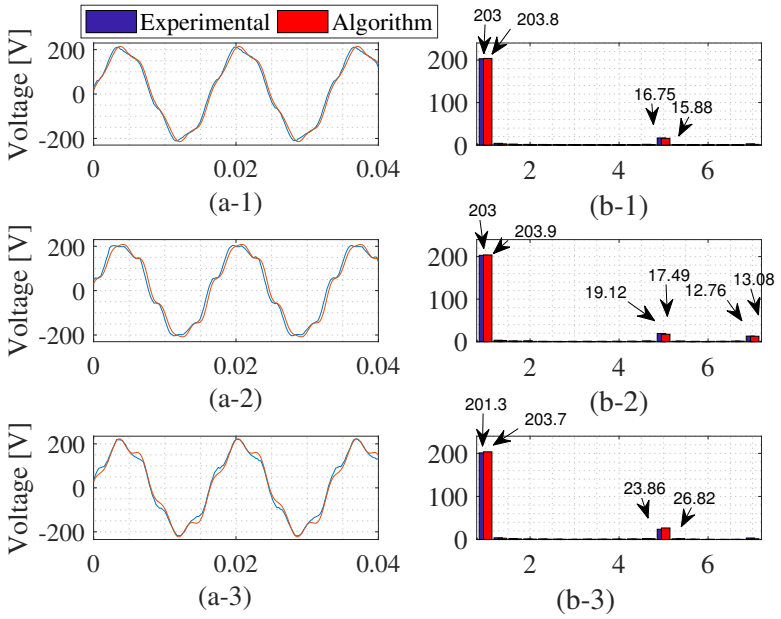

Figure 34 – Reference voltage for modulation for the first, second and third conditions (a-1), (a-2) and (a-3), respectively. And its respective harmonic spectrum in (b-1), (b-2) and (b-3).

- First condition: $\hat{V}_S = 214.5$ V $\rightarrow V_{dc} = 371.5$ V.
- Second condition: $\hat{V}_S = 208.2$ V $\rightarrow V_{dc} = 360.9$ V.
- Third condition: $\hat{V}_S = 223.4$ V $\rightarrow V_{dc} = 383.7$ V.

Therefore, the minimum required dc-link voltage for this harmonic profile to prevent overmodulation would be 383.7 V.

3.6 Discussion

As observed in the previous analysis, the LCL filter has a significant impact on the operation of MI with HCS, and therefore, additional precautions must be taken.

The methodology implemented in this work can be used in two ways: as an auxiliary tool in the passive filter and dc-link voltage design, and to evaluate already installed projects that have been retrofitted to provide HCS for nonlinear loads. Additionally, the results provided by the algorithm can answer two important questions: What is the limit imposed by the filter for a given harmonic current? What is the required dc-link voltage to safely compensate a given harmonic load current?

3.7 Chapter conclusions

The analysis conducted on the operating limits of inverters during HCS has provided valuable insights for sizing crucial elements and characteristics of the system, such as the passive components of the LCL filter and the dc-link voltage. Particularly the inductors, as evidenced in the same filter project, it is possible to choose inductance values within a range. This can result in a significant variation in the limits imposed by the dc link, approximately 40% in the case being studied.

Furthermore, the algorithm implemented for analysis serves as a valuable tool in assisting the design of LCL filters and determining the appropriate dc-link voltage. It also has the potential to evaluate existing projects that could be retrofitted to accommodate HCS for nonlinear loads. The methodology presented here can be extended to encompass other types of inverters and passive filter topologies, thus expanding its applicability and utility. In the upcoming chapter, the impacts caused by the saturation of inductors on the inverters ability to provide HCS will be presented.

4 Impact of Inductor Saturation on the Operating Limits of Grid-Tied PV Inverters with HCS

The nonlinearities of the inductors can have a significant impact on the performance and stability of the PV system. Due to the nonlinear and time-varying nature of the inductor, the current waveform produced may contain odd harmonics, leading to an increased THD of the current, which is subject to regulatory limits. Additionally, inductance saturation can compromise the stability of current-controlled systems and the actual value of the inductance is challenging to estimate due to its time-varying nature. The use of current-dependent models of nonlinear inductors has been proposed to study the behavior of the system and to develop controllers that can mitigate the effects of inductance saturation and harmonic distortion.

The nonlinear inductance of the filter can change depending on the current level, which makes it difficult to estimate accurately. When considering capability curves, inductance has a direct impact on the ability to withstand harmonic currents. Fig. 35 presents an example of a current-inductance curve. It is noteworthy that depending on the operating region of the inductor, there can be significant variations in inductance. These variations have the potential to undermine the effectiveness of the PV system for multifunctional operations.

The objective of this chapter is to analyze the impact of inductor nonlinearities on the inverter's ability to provide HCS.

4.1 Model of nonlinear inductor

An inductor is an electrical component that stores energy in a magnetic field when current flows through it. Nonlinearities in inductors refer to deviations from ideal behavior, such as changes in inductance with varying current or temperature, hysteresis effects, and saturation effects. These nonlinearities can impact the performance of circuits that use inductors and need to be taken into consideration when designing and analyzing such circuits.

To model the behavior of nonlinear inductors, a number of mathematical models have been proposed in the literature (MASTROMAURO; LISERRE; DELL'AQUILA, 2008; VILKN, 2018). One approach is to use empirical models that are based on experimental data and can provide a good fit to the measured characteristics of the inductor. Another approach is to use analytical models that are based on physical principles and can provide a deeper understanding of the underlying physics of the inductor. These models can be used to predict the behavior of the inductor under different operating conditions and can be incorporated into circuit simulation

Source: Own authorship.

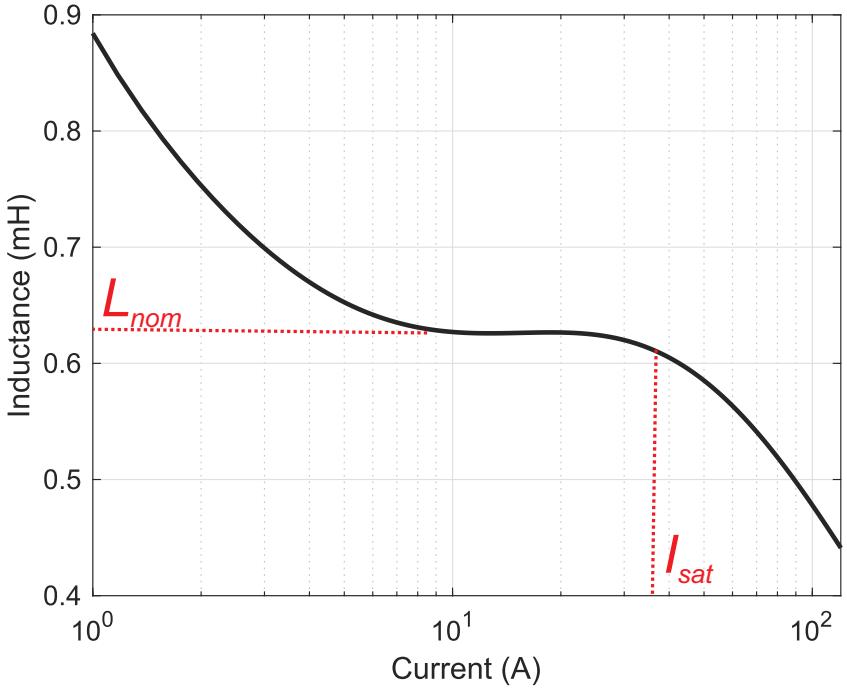

Figure 35 – Typical current-inductance curve.

software to design and optimize electrical circuits that contain nonlinear inductors.

In Mastromauro, Liserre, and Dell'Aquila (2008) it is presented three distinct models to account for the impact of core saturation in inductors. These models include the average model, which calculates the effective inductance of the inductor based on its average magnetic flux density, the piecewise linear model, which divides the magnetic flux density range into several linear regions and models each region separately, and the Volterra model, which is a more complex model that uses a mathematical technique to express a nonlinear function as a series of products of the function's input signals. In Vilkn (2018) is introduced a nonlinear inductance model that allows the simulation of saturation effects using inductor design data. This is achieved by utilizing the material's magnetic flux density (B) x magnetic field strength (H) curve and relevant equations that enable the derivation of B from current and H from voltage.

Given the specific context of this work, the most suitable model, which aligns with the needs and tools already employed, is the one proposed in Vilkn (2018). The equation for B depend on the geometry of the inductor and the voltage drop across the inductor (v_{ind}) and it is given by:

$$B(t) = \frac{1}{NA_e} \int v_{ind}(t)dt. \tag{4.1}$$

where N is the number of turns of the inductor and A_e is the cross-sectional area of the inductor core.

Through a lookup table containing the BxH values of the magnetic material used it is possible to determine the corresponding H. Subsequently, applying a suitable mathematical equation to the obtained magnetic field strength makes it possible to determine the inductor current.

$$i(t) = H(t)\frac{l_e}{N}, \tag{4.2}$$

where l_e is the inductor's magnetic path length.

A descriptive diagram and functions used to implement the nonlinear inductor model in the PLECS software are presented in Fig. 36.

Source: Own authorship.

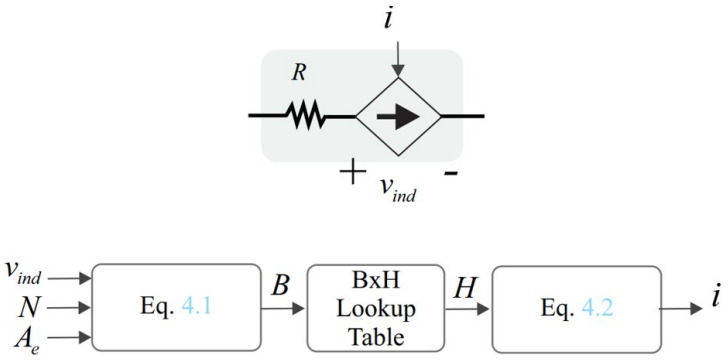

Figure 36 – Nonlinear inductor model implemented in PLECS software.

A simulation was conducted using the data presented in Table 3, in Chapter 2, to compare the performance of the ideal inductor and the implemented model. The characteristics of the inductors, along with the BxH curves needed for implementing the model, are presented in Appendix A. The tests were carried out in PLECS software, where only constant active power was injected. The results of the simulation were analyzed by measuring the total harmonic distortion (THD) of both signals, and the findings are presented in Table 5. Furthermore, an example of the analysis for active power injection of 1.2 pu is illustrated in Fig. 37 where it is presented the measured current and the current control error.

The results demonstrate the differences in behavior between the two approaches, with the saturation model exhibiting nonlinear effects. Specifically, Fig. 37 shows that the saturation model results in higher THD, indicating that the nonlinearities of the inductor have a significant impact on the current control performance. It is worth noting that these results are consistent with previous experimental results presented by Mastromauro, Liserre, and Dell'Aquila (2008), suggesting that the nonlinear behavior of inductors is a key factor in the design and implementation of current control systems.

Table 5 – Comparison of simulation results between the linear inductor and the implemented model.

Injected Power (pu)	THD (%)	
	Linear Inductor	Implemented Model
0.2	1.9	5.96
0.5	1.5	2.73
0.8	1.5	2.8
0.9	1.5	3.4
1.0	1.5	15.0
1.2	1.5	23.2

Source: Own authorship.

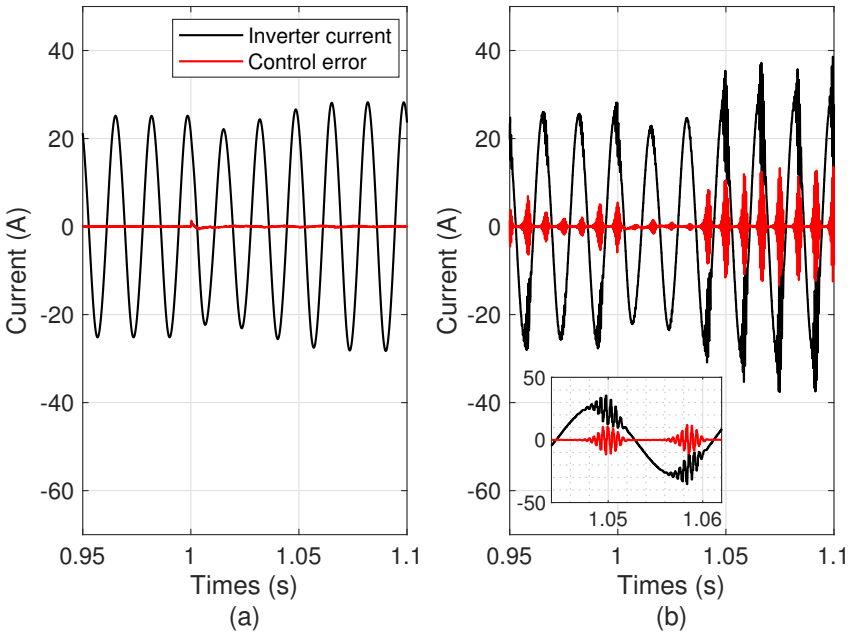

Figure 37 – Comparative analysis of current control using (a) ideal and (b) saturated inductor models (1.2 pu of fundamental current injection).

Besides the issues related to current control, inductor saturation can further compromise HCS by decreasing the margin of available dc-link voltage and current to perform the ancillary service. The impact of inductor saturation on HCS further emphasizes the importance of addressing the control errors resulting from inductor saturation. By mitigating these errors, it may be possible to improve the overall performance of the system, including its ability to support harmonic loads.

When the inductor is subjected to currents higher than a specified value, it can saturate, resulting in a significant change in its impedance and a subsequent alteration in the inverter's current control performance. Changing the current controller gains can help mitigate the effects

of the saturation in the current control. However, changing the gains too much can result in unstable operation in the current control loop.

It is important to bear in mind that the main interest is to prevent the inductor saturation process from reducing or making it impossible to achieve HCS, without compromising the stability of the system. Therefore, this work proposes to investigate an adaptation of the control to mitigate the effects of inductor saturation in the current control, as it affects the capability of the system to provide HCS.

4.2 Current control

In Yepes et al. (2011) authors provide several insights into the design and analysis of resonant controllers. For example, it notes that an increase in k_p can lead to faster transient response and less selective filtering, but can also decrease stability margins. Additionally, the text highlights that the effect of the integral gain k_{ih} on stability can often be neglected, but should be tuned to provide a balance between selective filtering and dynamic response.

Additionally, Yepes et al. (2011) also notes that traditional rules for stability analysis may not be suitable for resonant controllers. For example, a positive gain margin is not always sufficient for stability and there is always a positive and a negative phase margin for resonant controllers. Finally, the authors suggest that the sensitivity peak is a more compact and reliable stability indicator than phase margin. This is because it indicates the minimum distance to the critical point evaluated across all possible frequencies, rather than only at the crossover frequency.

The quantification of error rejection can be achieved through the sensitivity function, given by:

$$S(s) = \frac{1}{1 + P(s)G_c(s)}. \tag{4.3}$$

where $P(s)$ is the plant transfer function and $G_c(s)$ is the current controller transfer function.

The magnitude of $|S(s)|$ can reach its maximum value, referred as the sensitivity peak $1/\eta$, which can be utilized as a concise measure of the system's relative stability. Here, η represents the minimum distance to the critical point (-1,0j) in the Nyquist diagram, and it is used to quantify the actual proximity to instability.

In their work, authors in Yepes et al. (2011) provide guidelines for calculating the proportional gain to ensure stability, steady-state error, and filtering of switching harmonics. k_p gain can be calculated as,

$$k_p = \frac{R_T}{1-\rho^{-1}\sqrt{2}}\sqrt{2+2\rho^{-2}-(1+\sqrt{5}))\rho^{-1}}, \tag{4.4}$$

where $\rho = e^{\frac{R_T T_s}{L_T}}$, T_s is the sampling period and L_T and R_T are the equivalent inductance and equivalent series resistance of the filter, respectively.

After analyzing Eq. 4.4, it is found that k_p is determined solely by the sampling time and the total resistance and inductance of the circuit. Since inductor saturation causes the inductance to decrease below the nominal value, the current control will exhibit different characteristics than those for which it was designed. This raises the hypothesis that adjusting the gain of the controllers can mitigate the control errors resulting from inductor saturation. Furthermore, it is important to note that the k_p gain remains constant and does not depend on the specific harmonic orders that are being compensated.

Specifically, the proportional gain (k_p) is directly linked to selective filtering and the stability margin of the system. By using sensitivity analysis, it is possible to assess the effectiveness of adjusting the controller gains in mitigating the effects of inductor saturation on the control system. It is worth noting that the focus of the controller adjustments is on mitigating the effects of inductor saturation in the current control, rather than preventing saturation from occurring.

To summarize the effect of proportional gain variation on system sensitivity, Table 6 is presented. The base value of $k_p = 29.66$, as calculated using Equation 4.4, is varied to observe the effect of this change on the system's sensitivity. It is important to note that the higher the η value, the more robust the system will be. It is worth noting that decreasing the proportional gain directly impacts sensitivity of the system. Fig. 38 illustrates the effects of varying the proportional gain on the stability analysis of the system through the Nyquist diagram. To some extent, reducing the proportional gain can improve η, which in turn can benefit the system by enhancing its robustness. However, it is important to consider that decreasing k_p also leads to slower control, which can affect the system's stability.

4.2.1 Adjustable current control design

An idea for a new control technique to avoid anomalous instability behavior involves adjusting the proportional gain of the controller based on the system's operating conditions. This technique takes advantage of the fact that the proportional gain affects the system's stability directly as previously shown. By monitoring the system's response and adjusting the proportional gain, the controller can be fine-tuned to avoid anomalous conditions in the current control. In Zarei, Mokhtari, and Blaabjerg (2021) it is presented a fault detection and protection coordination strategy that can detect and locate faults in the system, even when fault currents are close to the nominal current of the converters. The study also identifies a control technique that modifies

Source: Own authorship.

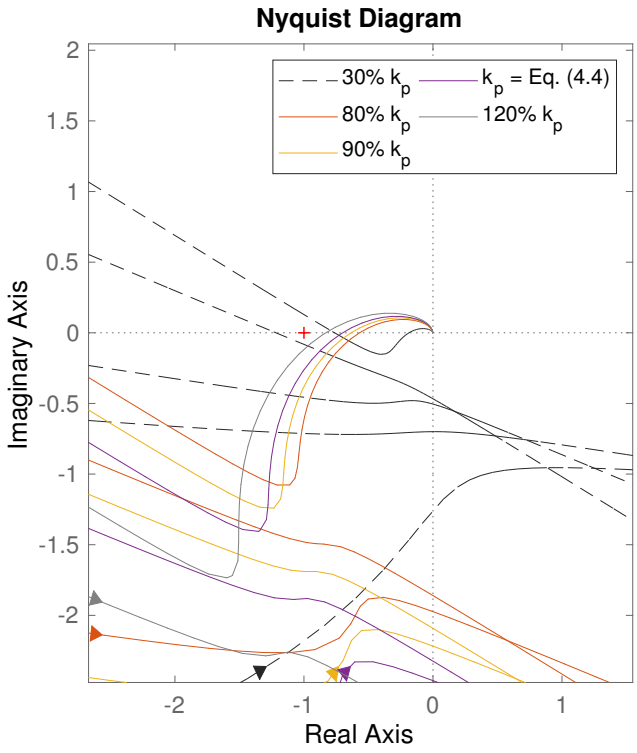

Figure 38 – Nyquist diagrams of $G_c(s)P(s)$ for different values of k_p.

Table 6 – Effects of varying the proportional gain of the resonant controller on the system sensitivity. *Remark*: $k_p = 29.66$ as calculated using Eq. 4.4.

k_p	η
20%	0.1195
30%	0.3272
40%	0.6550
50%	0.7816
80%	0.8415
90%	0.8352
100%	0.8288
120%	0.8125

the control action of a resonant controller according to the system's operating conditions. PMR control is chosen for the current loop because it can achieve high bandwidth and robustness.

The dynamics of the LCL filter capacitor are neglected in order to simplify the plant modeling of the inner control loop (MASTROMAURO; LISERRE; DELL'AQUILA, 2008; LISERRE; BLAABJERG; HANSEN, 2005). The plant model transfer function of the dc/ac stage current control is given by:

$$P(s) = \frac{1}{L_T s + R_T}, \tag{4.5}$$

The current control is conducted in the $\alpha\beta$ reference frame where the current reference is a sinusoidal signal. The PMR controller provides the resonant frequency to achieve infinite theoretical gain and reduce the steady-state error (YEPES et al., 2011). The transfer function of the PMR controller can be expressed as follows:

$$G_c(s) = k_p + \sum_{h=1,5,7,11,13} G_R(s), \tag{4.6}$$

where $G_R(s)$ is the resonant part of the controller given by:

$$G_R(s) = k_{ih} \frac{s}{s^2 + h^2 \omega_f^2}. \tag{4.7}$$

where k_{ih} is the integral gain tuned at the harmonic order h and ω_f is the fundamental frequency.

The PMR controller is applied with the resonant frequency set to the fundamental frequency of the grid voltage (60 Hz) and at harmonic orders of 5^{th}, 7^{th}, 11^{th}, and 13^{th}. The controller is discretized using the pre-warping Tustin method. Fig. 39 shows the open-loop Bode diagram of the PMR control.

Source: Own authorship.

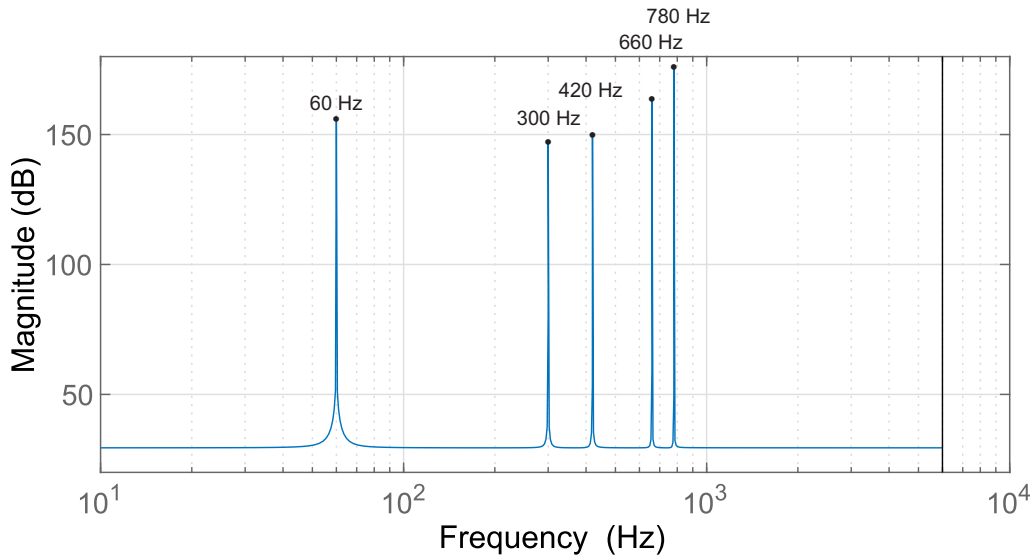

Figure 39 – Open-loop diagrams of PMR current controller.

As discussed in Section 4.1, saturation can cause an increase in the THD of the current produced by the inverter and lead to a higher steady-state error in the control. To address this

issue, it is proposed an adjustable control approach that involves using a peak detector to evaluate the control error (e) and an additional anti-windup PI controller with saturation limits between a minimum value and 1 to generate a correction factor (k_e) that adjusts the proportional gain of the resonant control. The control action to adjust the proportional gain will be implemented through a threshold error value (e^*_{thold}), which is a constant carefully selected to prevent the inherent noise in current control from triggering unnecessary actions. The threshold error value is determined through simulation in a non-saturate state of the inductors. The minimum saturation value defined in PI is determined by analyzing the Nyquist diagrams and the sensitivity of the system, which involves varying the gain (k_p), as demonstrated in Sections 4.1 and 4.2.

The control modeling assumes that the current control loop operates at a much faster rate than the anti-windup PI control action. Fig. 40 presents the complete inverter control structure.

Source: Own authorship.

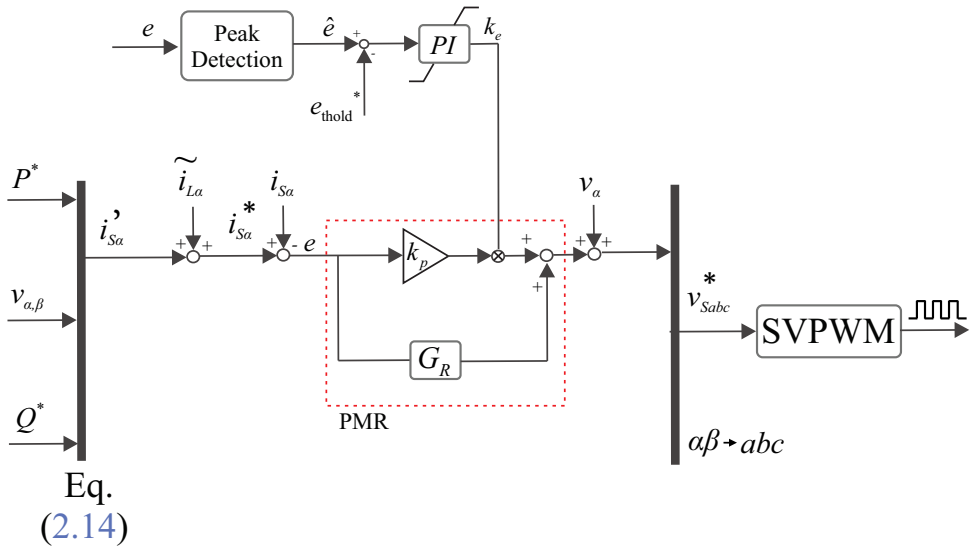

Figure 40 – Complete inverter control structure.

The transfer function $U_C(s)$ of the PI controller is given by:

$$U_C(s) = k_{pPI} + \frac{k_{iPI}}{s}. \tag{4.8}$$

where k_{pPI} and k_{iPI} are the proportional and integral gains of the PI controller, respectively.

The peak detection algorithm incorporates a delay, denoted by the term $e^{-s\tau}$. This delay can be approximated using a first-order delay transfer function, which can be described as follows:

$$e^{-s\tau} = \frac{1}{\tau s + 1} = J(s). \tag{4.9}$$

To ensure that the pole of $J(s)$ is canceled by the zero of $U_C(s)$, the PI gains are designed adopting the relationship $\tau = k_{pPI}/k_{iPI}$.

The closed-loop transfer function of the adjustable control is:

$$A(s) = \frac{k_p k_{iPI}}{s + k_p k_{iPI}}, \tag{4.10}$$

and the following controller gains can be found as:

$$k_{iPI} = \frac{2\pi f_p}{k_p} \tag{4.11}$$

and

$$K_{pPI} = \tau K_{iPI}. \tag{4.12}$$

where f_p is the pole frequency of $A(s)$. The peak detector introduces a certain amount of time delay that is determined by the fundamental frequency of the signal being detected. Moreover, the closed-loop system cannot operate faster than the delay imposed by the peak detector. Increasing the speed of the closed-loop beyond the limit imposed by the peak detector may result in suboptimal performance.

4.2.2 Adjustable current control analysis

Initially an assessment of the adjustable PMR control's dynamics and performance will be conducted to ensure compliance with design criteria. Subsequently, the output response will be analyzed to guarantee system performance metrics, including rise time and settling time. The stability, performance and dynamic behavior of the system can be evaluated. The controller was designed to operate at 6 Hz, which is two decades below the 120 Hz delay imposed by the peak detector. This results in the controller having gains of K_{pPI} = 0.020 and k_{iPI} = 1.25. The system has a time constant of 0.0265 s, a rising period of 0.583 and a settling period of 0.104. To evaluate the control implemented in the simulation, a step is applied to the error threshold, and the control response to this step is analyzed.

Upon analyzing the response, in Fig. 41, it can be seen that the simulated system's behavior in response to the error threshold step is consistent with the proposed behavior, exhibiting a rise time of approximately 0.45 and a settling time of 0.88.

Additionally, the simulation of the complete system and the adjustable current control, as presented in Sections 2.3 and 4.2.1, were carried out in the PLECS software. The inductor

Source: Own authorship.

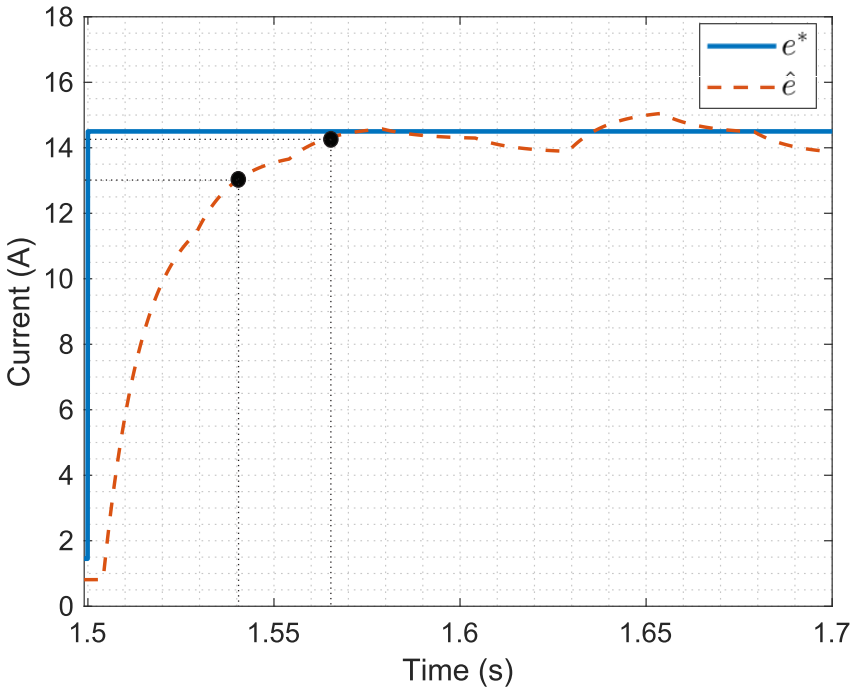

Figure 41 – Simulation adjustable PMR control error step response.

used is the 2 mH whose characteristics are shown in Fig. 44. The operating conditions of the adjustable PMR control were simulated, and the graphs of the synthesized current, control error, and k_e factor are presented in Figs. 42 and 43. After the initial transients at 1.2 s, an injection of 8 A of fundamental + 5 A of 5^{th} harmonic peak current start. At the instant 2.2 s, the fundamental current is increased to 14 A, keeping the 5^{th} harmonic amplitude. Finally, at time 3.8 s, the inverter current ceases. Figures 42 and 43 show the simulation results obtained with the adjustable control turned off and turned on, respectively.

In the results obtained with the adjustable control turned off, as shown in Fig. 42, an increase in the error of the current control is visible at 2.2 s, which can be attributed to control issues resulting from the saturation of the inductor. Since there is no action taken by the adjustable control, the current error persists until the current reaches levels that do not cause saturation in the inductor core.

In Fig. 43 during the injection of only 8 A of fundamental current and 5 A of 5^{th} harmonic current, it is observed that the nonlinear inductor effects in the current control are minimal, and the adjustable control does not enter in operation, except for a transient at the beginning of the current injection at 1.2 s. However, when the fundamental current increases, it is observed that the error in the current control increases due to the nonlinearities caused by the inductor operating in the saturated mode. This causes the adjustable control to come into operation, reducing the value of the control proportional gain. By second 3.8 s, the current stops, and the control adjusts again

Source: Own authorship.

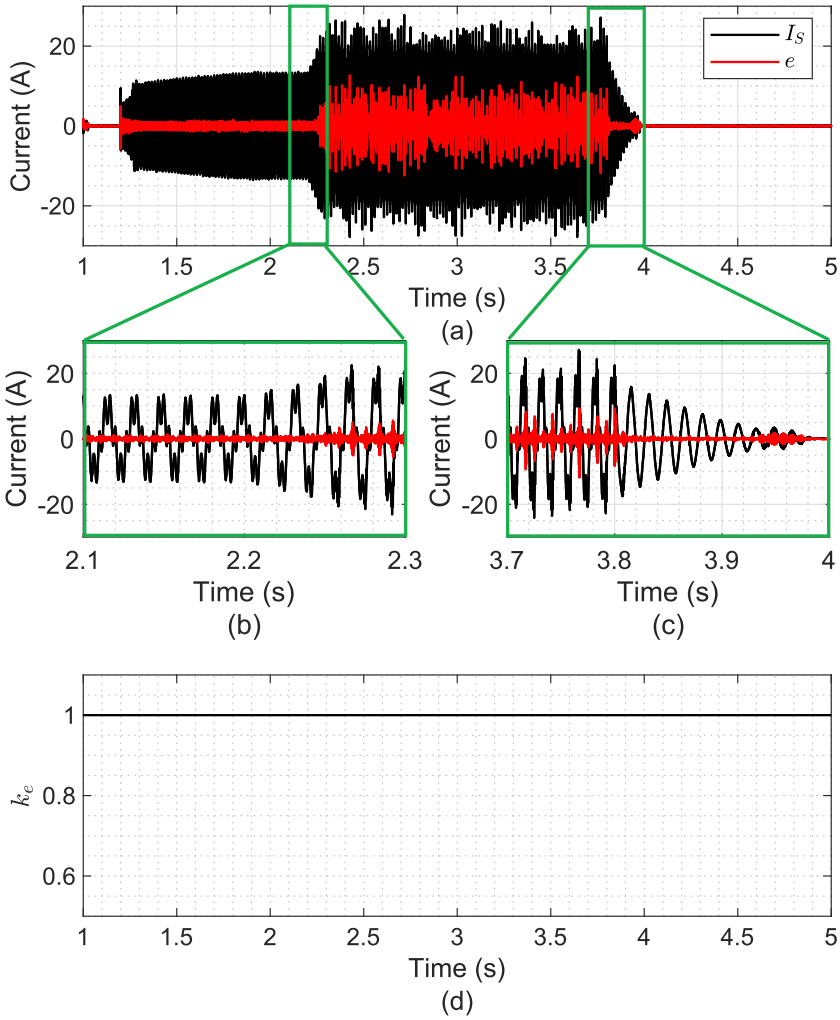

Figure 42 – Simulation result of (a), (b) and (c) synthesized current and current control error, and (d) k_e factor with no adjustable control.

to the unity value.

In addition to Table 5, it is presented in Table 7 the THD values of the output current are included for the simulation of the inductor model that is implemented using the adjustable control operation.

It is noteworthy that when operating with the adjustable control turned off, the system operates with higher THD and error values as demonstrated in Table 7, despite not reaching a point of instability. This behavior confirms the effectiveness of the proposed adjustable PMR control in mitigating the effects of inductor saturation on current control, ensuring that the controller operates as designed unless an unexpected condition occurs. Overall, the simulation results demonstrate the feasibility and effectiveness of the proposed control strategy to reduce

Source: Own authorship.

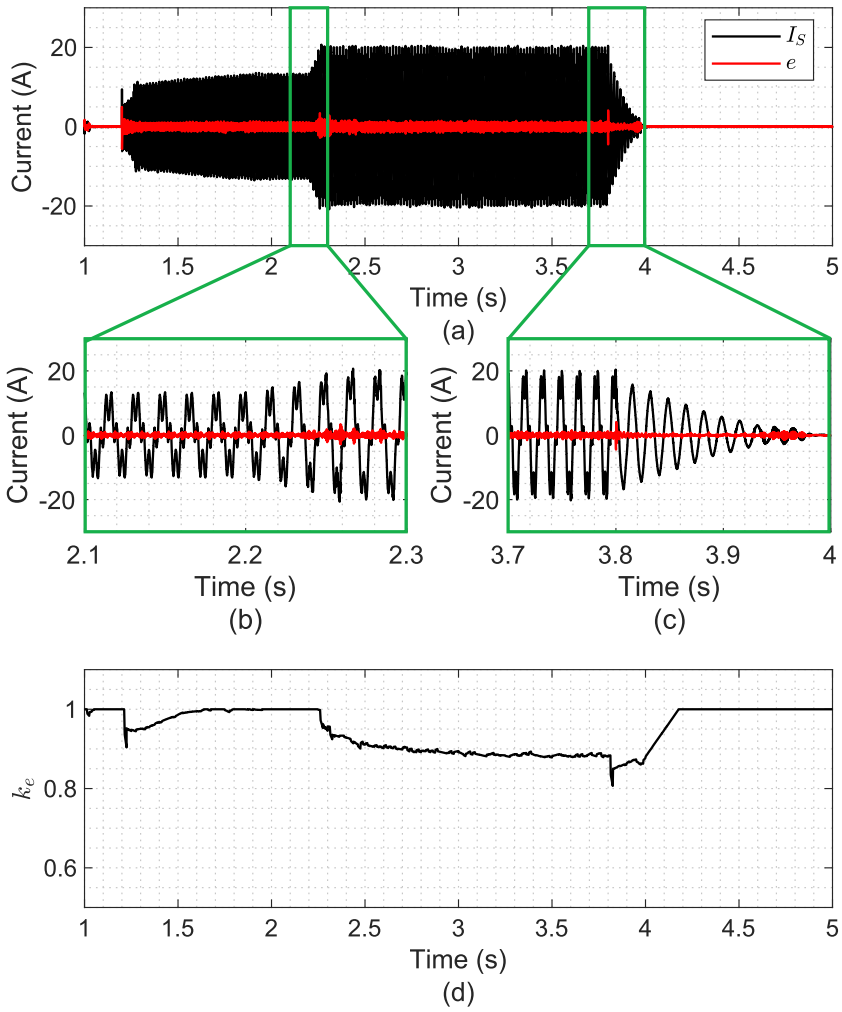

Figure 43 – Simulation result of (a), (b) and (c) synthesized current and current control error, and (d) k_e factor with adjustable control.

the effects of inductor saturation on current control in HCS applications.

As demonstrated, it is evident that the nonlinearities of the inductors can cause significant control problems. However, it was possible to identify mechanisms that mitigate these effects in the current control, such as adjusting the selective filtering and the dynamic response of the PMR controller through the proportional gain. The proposed technique is simple and can be easily implemented in existing control systems with minimal modifications, making it a cost-effective solution for improving the stability and performance of the system during HCS. Another way to address control problems is to design inductors using cores with more linear behavior within the excursion of the rated current of the inverter.

Table 7 – Comparison of simulation results between the linear inductor and the implemented model with and without the adjustable control.

Injected Power (pu)	THD (%)		
	Linear Inductor	Implemented model	
		Without adjustable control	With adjustable control
0.2	1.9	5.96	3.17
0.5	1.5	2.73	1.97
0.8	1.5	2.8	1.71
0.9	1.5	3.4	1.70
1.0	1.5	15.0	1.60
1.2	1.5	23.2	4.35

4.3 Capability curves

The process for deriving the capability curve is similar to the one discussed in Chapter 3, except for the need to incorporate the nonlinearities of inductor saturation into the implemented code. The first step is to obtain the inductance versus current curve, which can be accomplished by following the steps outlined below:

- Obtain the B x H curve: During the design of the inductors, as explained in Appendix A, the equation for raising the magnetization curve for each of the cores can be obtained directly from the manufacturer's catalog.
- Calculate the magnetic permeability: the magnetic permeability is the ratio of the magnetic flux density (B) to the magnetic field strength (H). This can be calculated for each data point on the B x H curve.
- Calculate the inductance: the inductance (L) of the inductor can be calculated using the formula $L = N^2/\mathcal{R}$, where N is the number of turns in the inductor and $\mathcal{R}$ is the reluctance of the magnetic circuit. The reluctance can be calculated as $R = l_e/(\mu A_e)$, where l_e is the length of the magnetic circuit, A_e is the cross-sectional area of the magnetic circuit, and μ is the magnetic permeability.
- Obtain the inductance vs current data: by plotting the inductance values against their corresponding current values, a lookup table can be generated.

Note that the inductance vs current curve is only valid for the range of current values for which the BxH curve is obtained. If the current exceeds this range, the magnetic properties of the inductor may change and the inductance vs current curve will no longer be accurate. Fig. 44 shows an example of the L x i curve obtained through the inductor's B x H curve.

Source: Own authorship.

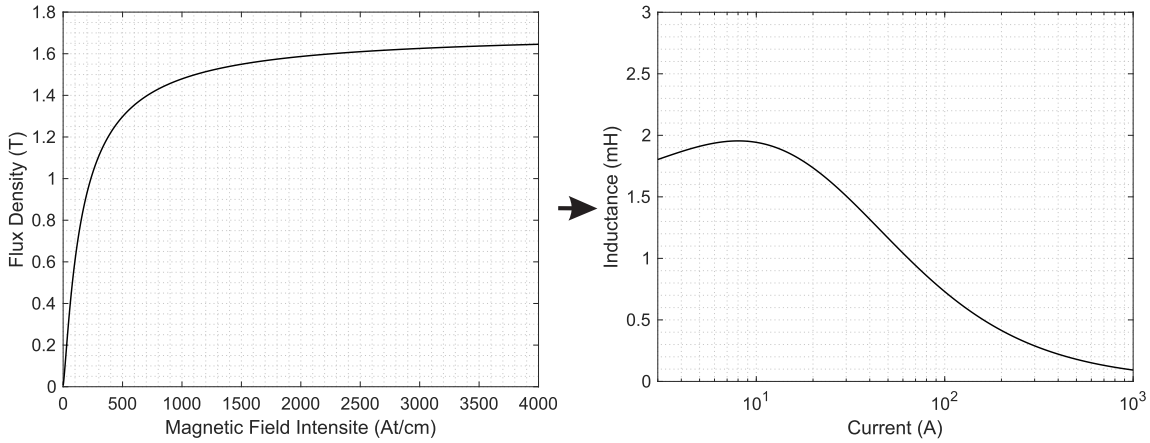

Figure 44 – Example of the L x i curve. Material: Xflux Toroid - Part Number: 78777 - $N = 102 - l_e = 177.2mm - A_e = 492.0mm^2$

Source: Own authorship.

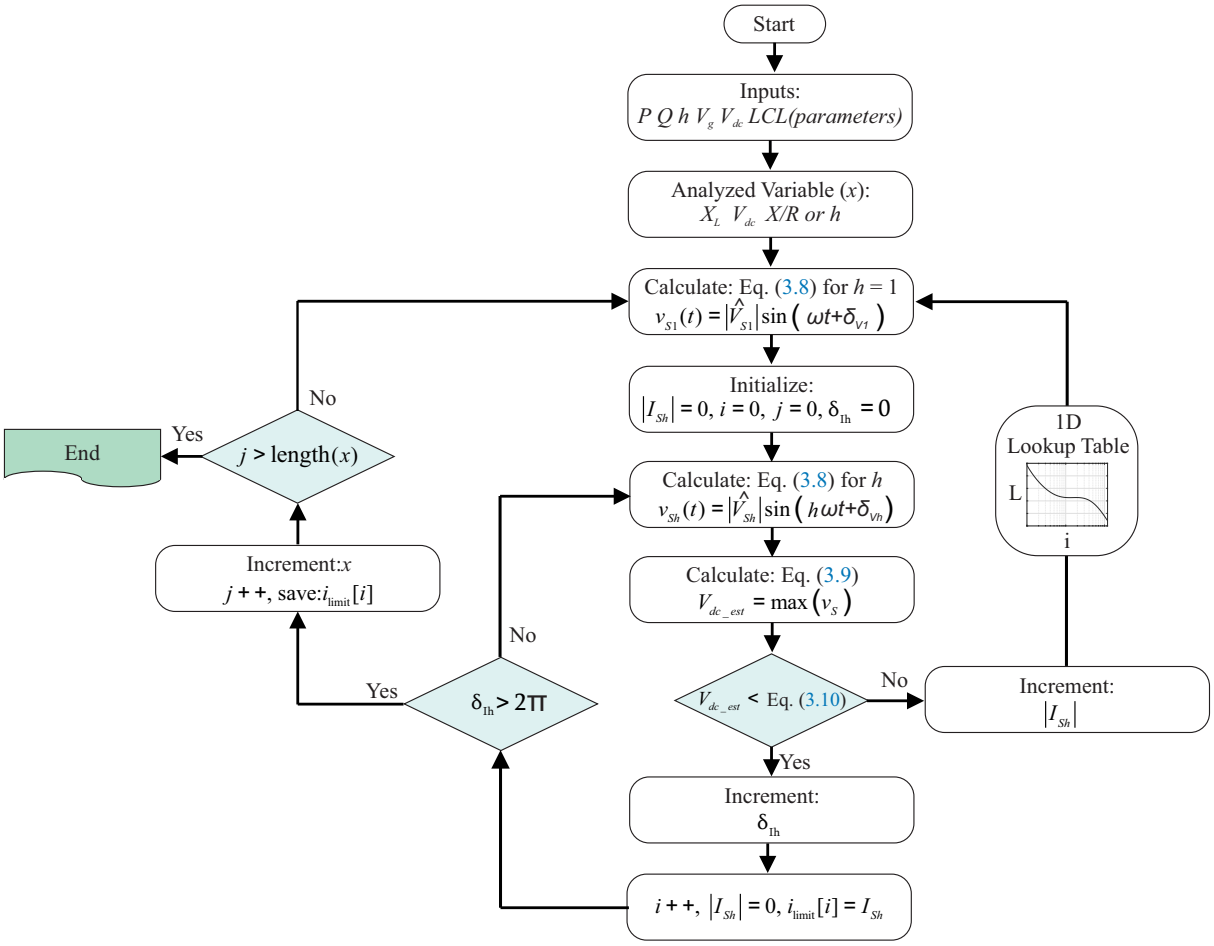

Figure 45 – HCL imposed by dc-link voltage algorithm flowchart diagram.

This enables to update the guidelines presented in Chapter 3 as follows. The algorithm

requires input information such as power data, the specific harmonic orders to be compensated (as each order causes a different voltage drop in the filter), filter parameters, grid voltage, dc-link voltage, and the B x H curve. The algorithm consists of the following steps, as shown in the flowchart in Fig. 45:

1. Calculate from Eq. (3.9), for $h = 1$, the necessary voltage to flow the specified active power to the grid;
2. An iteration increases the harmonic current amplitude and using Eqs. (3.9) and (3.10) until the stop condition to be satisfied;
3. Every time a current increment occurs and the iteration does not reach the stopping conditions specified by Eq. (3.11), the algorithm automatically updates the region in which the nonlinear inductor is operating.
4. The stop condition is the dc-link voltage value defined by Eq. (3.11) greater than V_{dc_est}. Where, V_{dc_est} is the estimated dc-link voltage value based on Eq. (3.10);
5. A new iteration is done for completing the saturation limits. The process needs to be repeated for each possible harmonic current angle;
6. Steps 2, 3 and 4 are repeated to complete the selected variable analysis: the dc-link voltage, the harmonic order or one of the LCL filter parameters. The stopping condition is determined by the size of the vector of the variable under analysis (x), which defines the number of iterations required to complete the process;
7. The algorithm output is a vector (i_{limit}) with the maximum harmonic current for each phase angle that can be synthesized without exceed the linear region of the modulation.

4.4 Simulation results

When there is a need to support harmonic currents and there are problems with inductor saturation, it is imperative to mitigate the problems caused by current control. These problems can drastically reduce the margin for supporting harmonic currents. For these reasons, a test will be conducted to determine the capacity of a system with nonlinear inductors to support harmonic currents using the adjustable control.

MATLAB software was used to implement the algorithms outlined in the flowchart presented in Fig. 45. The simulation of the complete system and the adjustable current control, as presented in Sections 2.3 and 4.2.1, were carried out in the PLECS software. This approach permits a comprehensive assessment of the limitations of grid-tied inverters and the resultant capability curves, which can aid in the design and implementation of multifunctional converters.

In order to obtain the simulation results, the PV inverter is initially configured to inject 5^{th} and 7^{th} harmonic order currents separately. The dc-link voltage is controlled to maintain a constant value of 370 V. To assess the behavior of the system under varying conditions, the angle of injection is varied from 0 to 360° in increments of 45° for both harmonic orders. For each angle setting, the harmonic current is gradually increased from 0 A until the maximum limit imposed by the dc-link voltage is reached. The maximum amplitude of the reference signal sent to the PWM is measured to determine this limit. It is important to note that during the tests, a fundamental current of 9.2 A (0.7 pu) is maintained. Fig. 46 presents the simulation results for the 5^{th} and 7^{th} harmonic orders.

Source: Own authorship.

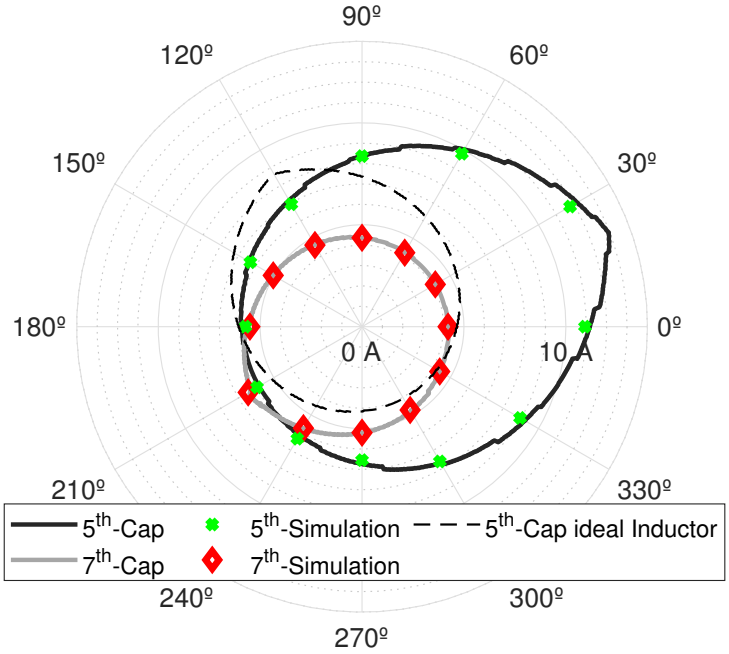

Figure 46 – Comparison between inverter capability curve (Cap) and simulation results (Simulation) for 5^{th} and 7^{th} HCS. Capability curve for 5^{th} order current using ideal inductor for comparison (dashed black line).

The colored points depicted in Fig. 46 closely approximate the algorithm theoretical results, indicating a strong correlation between the developed algorithm and the simulation results. Notice the difference in the 5^{th} harmonic current curves with and without saturation. There is a discrepancy not only in the angle at which the maximum current can be compensated but also in the total amount of harmonic that can be compensated. This effect arises from the difference in the effective inductance of the nonlinear inductor, which in turn alters the output filter impedance, thereby modifying the compensation curve.

This is a significant finding as it validates the accuracy of the proposed methodology for validating HCS considering the inductor saturation effects. In Chapter 3, the algorithms validation were demonstrated in the form of parametric variations, such as the values of the passive elements of the filter, harmonic order, and dc-link voltage. This chapter now focuses on

validating the implementation of the nonlinear inductor model effects on the capability curve. It is also important to note the significance of the PMR control with adjustable gain, as its absence makes impractical to deduce the voltage limits due to the nonlinear effects in the current control.

In order to ensure the robustness and stability of the control system in PV systems with LCL filters, it is essential to perform a sensitivity analysis over the entire dc-link voltage limit to HCS capacity range. Such an analysis can help to identify the points where a possible drop in the robustness of the control system may occur. However, it is important to mention that the graph does not show regions of instability, but rather regions where the effects of nonlinear inductors can cause control issues.

The results presented in Fig. 47 were obtained by analyzing each point inside the 5^{th} harmonic capability curve while maintaining a fundamental current of 0.7 pu, using the inductor model as presented in Fig. 44. It is important to note that this sensitivity analysis was performed using the proportional gain as calculated from Eq. 4.4 without the adjustable control. For each point, the effective inductance was computed for the given condition, and the sensitivity of this condition was calculated. It can be observed that for certain angles of the 5^{th} harmonic, amplitudes of 6 A already show drops in the robustness of the system. It is important to note that a higher value of η indicates greater robustness of the system.

Source: Own authorship.

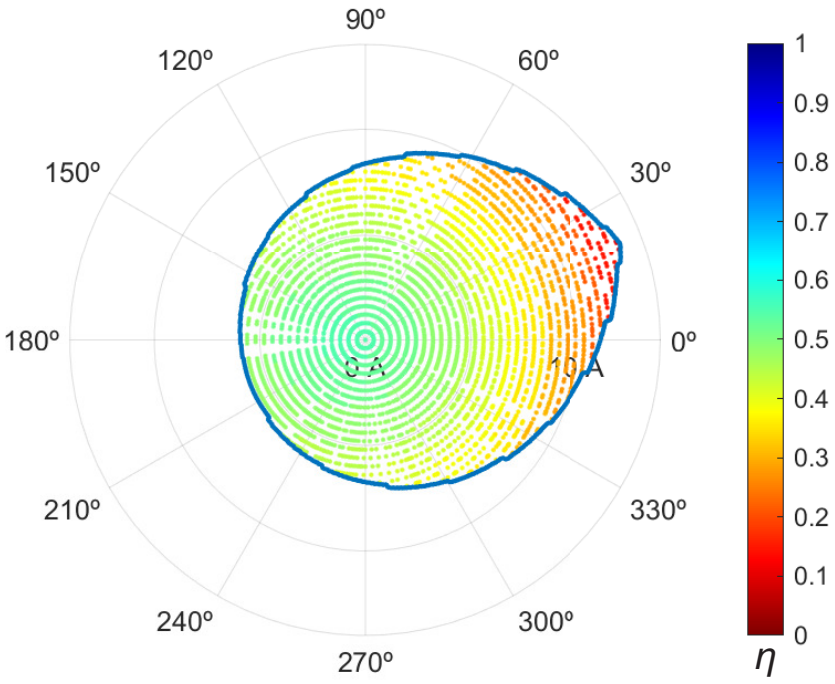

Figure 47 – Sensitivity analysis for the inverter capability curves for HCL imposed by dc-link voltage.

Conducting a sensitivity analysis can also help identify potential areas for further im-

provement in the design of the control system. By analyzing the system's behavior under different operating conditions and parameters, designers can identify areas where changes may be needed to improve its performance and reliability. This can lead to the development of more efficient and effective control systems for PV systems with LCL filters with HCS.

4.5 Discussion

The effects of inductor saturation on current control have a significant impact on the ability of inverters to provide HCS. Identification of saturation issues allows for the adoption of mitigation strategies to address the control problems. These strategies may include replacing inductor cores with more linear cores in the system's operating region or designing more robust current controls to counteract saturation effects.

Additionally, the previous analysis demonstrates the nonlinear effects of inductors can be incorporated into the inverter capability curves, resulting in more reliable curves that reflect the actual behavior of the photovoltaic system. This enables the tools developed in this study to assist in evaluating and designing the capacity of inverters to provide HCS.

4.6 Chapter conclusions

This chapter discussed the impact of nonlinearities in inductors on the performance and stability of PV systems. Results showed that the inductor saturation can compromise HCS by decreasing the margin of available dc-link voltage and current to perform the ancillary service. The impact of inductor saturation on HCS further emphasizes the importance of addressing control errors resulting from inductor saturation to improve the overall system performance. To mitigate the impact of inductor saturation on current control, a PMR controller with an adjustable k_p gain is proposed. The results demonstrated that the control system successfully maintains the THD of the current within the 5% limit prescribed by technical standards.

Once the saturation of the inductors is mitigated by any adopted measure, it is evident when comparing the capability curves of the linear model and the nonlinear model that the limits imposed by the dc-link voltage behave differently. This is due to the fact that the nonlinear inductor exhibits variable inductance along the current excursion, which leads to a correlation between the module and angle of the filter impedance and this variation. The methodology presented in this study can also be extended to other inverters and passive filter topologies. The subsequent chapter outlines an optimization design methodology for the MI's LCL filter, aimed at selecting the optimal LCL filter parameters to enhance HCS capabilities.

5 Optimized Design of LCL Filter for HCS

Passive filter designs are used to mitigate harmonic current injection into the grid (PAUKNER et al., 2015). However, with the implementation of ancillary services, such as HCS, different conditions are imposed on these systems. A complicating factor during HCS is the increased losses in the overall system, including switching, conduction, and passive element losses (DE BARROS et al., 2018). Although ancillary services can improve PQ, high efficiency and high power density are still desired (DROFENIK; KOLAR, 2006).

Therefore, in order to strike a balance between efficiency and power density, a multi-objective optimization is necessary. In literature, converter optimization analysis focusing on efficiency (KOUTROULIS; BLAABJERG, 2011) and size (K. et al., 2009) has been presented. To attain this targets, the system performance must be analyzed in a multi-dimensional space (LE LESLE et al., 2017). Hence, an optimization technique is employed to obtain the optimal solution for a given set of specified objectives.

5.1 Design procedure

The circuit topology, along with its control and modulation strategies, must be selected with defined parameters to meet desired specifications (KOLAR; BIELA; MINIBOCK, 2009). Additionally, minimum requirements for the system performance must be set (BORTIS; NEUMAYR; KOLAR, 2016) and the physical limits of components must be respected (LE LESLE et al., 2017). While some components are designed from scratch, providing a wide range of design variables, such as magnetic components for inductors, others, like semiconductor devices, are prefabricated modules with limited selectable variables. The design process includes the following steps: adjustment of LCL filter parameters, inductor design, semiconductor and capacitor selection, and cooling system design. It is important to note that this work proposes a guide to evaluate and compare LCL filter parameters for HCS.

5.1.1 LCL Parameters Design

The LCL filter parameters vary with the system operating frequency. Higher switching frequencies require lower values of inductance and capacitance, resulting in a smaller filter volume. To find an optimal design for filter elements, the switching frequency is varied within an acceptable range for the chosen semiconductors. A switching frequency range from 7 to 40 kHz, f_{min} and f_{max}, respectively, is adopted. Based on the methodology for LCL filter design

presented in Appendix B, the grid parameters and inverter power showed in Table 3 in Chapter 2, the LCL filter project was carried out.

The relationship between the resonance and switching frequencies ($r_f \approx 4.5$) is chosen based on a series resistor damping strategy. The damping resistor is calculated according to Pena-Alzola, Liserre, Blaabjerg, Sebastian, et al. (2013) as:

$$R_d = \frac{1}{2\pi f_s C_f}. \tag{5.1}$$

To obtain equal inductances and minimize voltage drop in the inductors, $r_L = 1$ is used, where r_L is the ratio between grid-side and inverter-side inductors. The r_q ratio (between filter inductance and capacitance) is varied between 1 and 10 with 0.1 steps. The following constraints are adopted to meet minimum design requirements:

- Minimum power factor equal to 0.995 to limit the filter reactive power;
- the THD must be smaller than 5% to respect grid codes;
- total inductance smaller than 0.1 pu to limit the filter voltage drop;
- total inductance smaller than purely inductive filter;
- minimum inductance in order to limit current ripple in the first inductor in 30%.

Fig. 48 presents the results of several passive filter designs that meet the constraints. It is apparent that multiple combinations exist for each frequency, which is due to the capacitor/inductor relationship (r_q). The behavior of r_q with regards to inductance and capacitance values for a fixed frequency is shown in Fig. 48. In total, there are 1,925 possible combinations between switching frequencies from 7 and 40 kHz.

5.1.2 Inductor Design

The inductor core and winding parameters are determined through an iterative design procedure recommended by the core manufacturer and adapted in Cota (2016). This methodology is explained in detail in Appendix C. The inductor values and switching frequencies are obtained through the filter design procedure outlined in Section 5.1.1.

In this study, the inductors were designed using toroidal, E and U cores produced by Magnetics with different material composition. According with Magnetics (2020) while all seven materials found in their catalog can be used for various applications, each has its unique advantages. To achieve the lowest loss inductor, Kool Mμ Hf and MPP materials should be used as they exhibit the lowest core loss. For designs that prioritize small package size in a dc

Source: Own authorship.

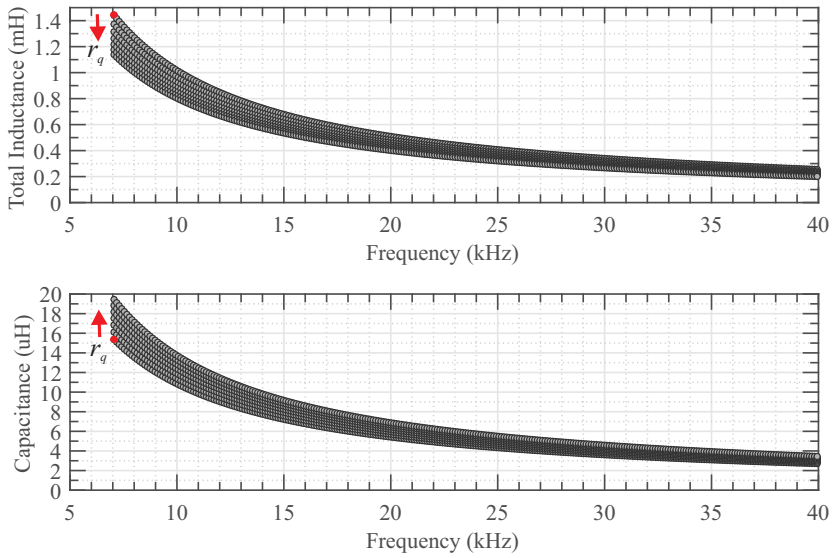

Figure 48 – LCL filter design: (a) total inductance; (b) capacitance.

bias dominated environment, Edge and High Flux are recommended as they possess the highest flux capacity. XFlux, on the other hand, can be a more cost-effective alternative to High Flux in situations where higher core losses and limited permeability availability are acceptable. Both Kool Mμ and Kool Mμ MAX are economical options that offer superior dc bias under current loading.

In conclusion, the following restrictions were applied to the inductor design:

- solid round wire for manufacturing simplicity and cost;
- fill factor equal to 0.4 as suggested in the manufacturer catalog;
- toroidal, E and U cores produced by Magnetics:
  - Kool Mμ Hf;
  - MPP;
  - Edge;
  - High Flux;
  - XFlux;
  - Kool Mμ MAX;
  - Kool Mμ.

5.1.3 Capacitor Selection

5.1.3.1 Dc-link Capacitor

The value of the dc-link capacitor is based on the maximum dc-link voltage ripple, which is a common approach used in many PV inverter designs (ABU-RUB; MALINOWSKI; AL-HADDAD, 2014). By setting a maximum allowable dc-link voltage ripple, the capacitance value can be calculated to ensure that the voltage remains within the desired range, as demonstrated in Singh, Chandra, and Al-Haddadl (2015).

$$C_{min} = \frac{I_0}{2\omega_f \Delta V_{dc}}. \tag{5.2}$$

where C_{min} is the minimum dc-link capacitance, I_0 is the capacitor rms current and ΔV_{dc} is the dc-link voltage ripple.

Nevertheless, the capacitor value calculated with traditional approach does not take into account multifunctional operation with HCS. As proposed in de Jesus et al. (2019), it can be defined a capacitance value to limit the oscillations caused by the mitigation of harmonic currents. As presented in de Jesus et al. (2019), the lower the harmonic order, the greater its influence on the dc-link power oscillation. By rearranging the equations introduced in de Jesus et al. (2019) and depicted in Eq. 3.13 and Eq. 3.14 in terms of the dc-link capacitance, it is obtained:

$$C_{min} = \frac{3 m_i I_{Sh}}{2r\omega_f (h \mp 1) V_{dc}}, \tag{5.3}$$

where m_i is the modulation index, I_{Sh} is the current peak value and r is,

$$r = \sqrt{\frac{\Delta V_{dc}}{V_{dc}} + 1} - 1. \tag{5.4}$$

It is important to note that each harmonic order utilized in the harmonic support process will contribute to dc-link oscillations. In this study, four harmonic orders were employed, specifically, 5^{th}, 7^{th}, 11^{th}, and 13^{th}. A capacitance value will be defined to limit the oscillation value to 1% of the dc-link voltage from the 5^{th} harmonic order. This value ensures that the dc-link oscillations resulting from harmonic support will not surpass the previously established 3% limit for conventional minimum capacitance designs, even when all four harmonic orders are simultaneously active. Table 8 presents the data required to calculate the capacitances.

Thus, considering the parameters described in Table 8, a minimum dc-link capacitance value of 500 μF is necessary to guarantee a voltage ripple of 3% on the dc-link and based on Eq. 5.3, the minimum capacitance required is 2200 μF.

Table 8 – Parameters of the System.

Parameter	Value
Grid voltage voltage (line to line) (v_g)	220 V
Dc-link voltage (V_{dc})	375 V
Harmonic current (I_{Sh})	3.7 A
Harmonic current order (h)	5
Fundamental frequency (ω_f)	60 Hz

For normal operation, the dc-link capacitor used is the B4352B9687M0, a 680µF/400V electrolytic capacitor manufactured by TDK with a maximum current at 100 Hz/40 °C of 8.1A. The capacitor bank is composed of two strings (each composed of two capacitors in series) connected in parallel. For multifunctional operation, the dc-link capacitor used is the B4352A9188M0, an 1800µF/400V electrolytic capacitor also manufactured by TDK with a maximum current at 100 Hz/40 °C of 17.2A. The capacitor bank is composed of two strings (each composed of two capacitors in series) connected in parallel.

5.1.3.2 LCL filter Capacitor

A popular choice for passive filters are film capacitors, which are known for their low equivalent series resistance (ESR) and ability to handle high frequency ripple currents with high reliability and low losses (KOLAR; BIELA; MINIBOCK, 2009). Film capacitors are also suitable for high voltage surge ratings.

In this work, film capacitors will be used in the passive filter design. As the capacitance range has already been established in Fig. 48 - (b), only the manufacturer and model of the capacitors need to be defined. The capacitors were selected based on the first commercially available capacitance value that was higher than the designed value. A summary of the capacitor characteristics can be found in Table 9.

Table 9 – Film capacitors selected. (EPCOS/TDK B32361A4)

Parameter	Value
Rated voltage (line to line)	480 V
Capacitance	5, 10, 15, 20, 25 and 30 μF
ESR	9.6, 4.8, 4.1, 4.3, 5.2, and 4.8 mΩ

5.1.4 Semiconductor Selection

The selection of semiconductors was based on the rated current capacity (13.12 A) of the proposed prototype. A silicon six-pack IGBT module from Infineon was chosen for this purpose. This product integrates a three-phase inverter circuit into a single module, allowing a compact

power circuit design. A summary of the semiconductor's characteristics can be found in Table 10.

Table 10 – Selected silicon module. (INFINEON FS15R12VT3)

Parameter	Value
Collector-emitter voltage	1200 V
Rated current	15 A
IGBT Thermal resistance junction to case	1.3 K/W
IGBT Thermal resistance case to heatsink	0.6 K/W
Diode Thermal resistance case to heatsink	0.65 K/W
Diode Thermal resistance junction to case	1.95 K/W

5.1.5 Thermal design

The design of the cooling system is based on the losses calculation in each semiconductor device and the thermal models of the entire system (ZHOU; HOLLAND; IGIC, 2008; COTA, 2016; ABRANTES, 2016; SANTANA, 2018; BALACHANDRAN; KUMARI, 2019). The heat generated by these devices must be effectively transferred to the environment to prevent overheating and potential device destruction (KUNZI, 2016). In this work, the Foster model is used to perform the thermal analysis. The Foster model is derived empirically by approximating the transient thermal impedance (Z_{th}) curve into an RC network (ZHOU; HOLLAND; IGIC, 2008). Fig. 49 shows the thermal Foster model, where C_{th} is the thermal capacitance, $R_{th,jc}$ represents the junction to case thermal resistance, $R_{th,ch}$ represents the case to heatsink thermal resistance, $R_{th,ha}$ represents the heatsink to ambient thermal resistance, and P_Q and P_D are the losses of the IGBT and diode, respectively.

Additionally, the steady-state thermal resistances $R_{th,jc}$ and $R_{th,ch}$ are usually provided in the manufacturer's datasheet, while information for the transient model is obtained from the device's transient thermal impedance curves. Fig. 50 shows a thermal impedance curve provided in the datasheet. The manufacturer also provides a table of thermal resistances and time constants related to the curve, which can be used to obtain the thermal capacitance as follows:

$$\tau_i = R_{th} C_{th}. \tag{5.5}$$

where τ_i is the thermal time constant.

In section 5.1.4, a silicon six-pack IGBT module with anti-parallel diodes from Infineon was defined. The steady-state thermal model of the module is presented in Fig. 51. By utilizing circuit analysis techniques based on the Foster model (MITSUBISHI ELECTRIC, 2020), the maximum thermal heatsink resistance can be estimated as,

Source: Own authorship.

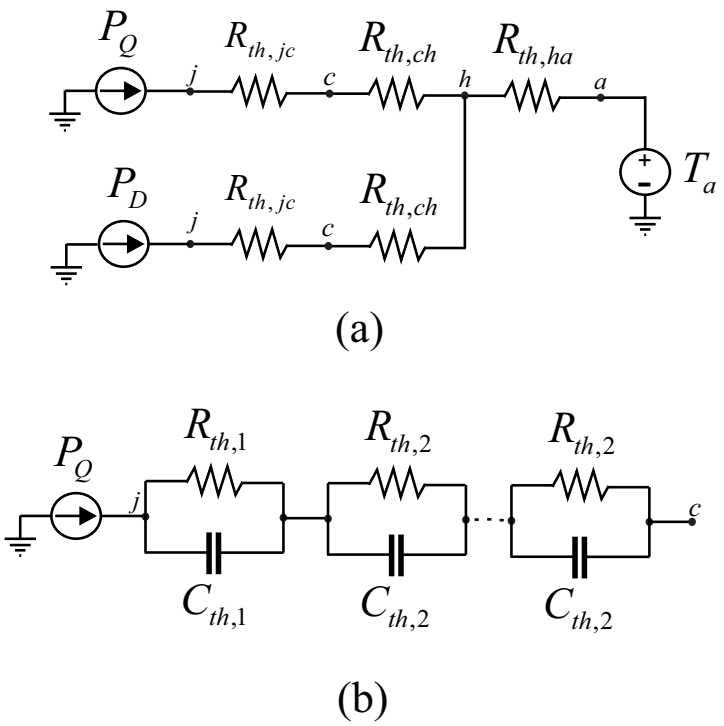

Figure 49 – Thermal model: (a) steady state; (b) transient model.

Source: Datasheet.

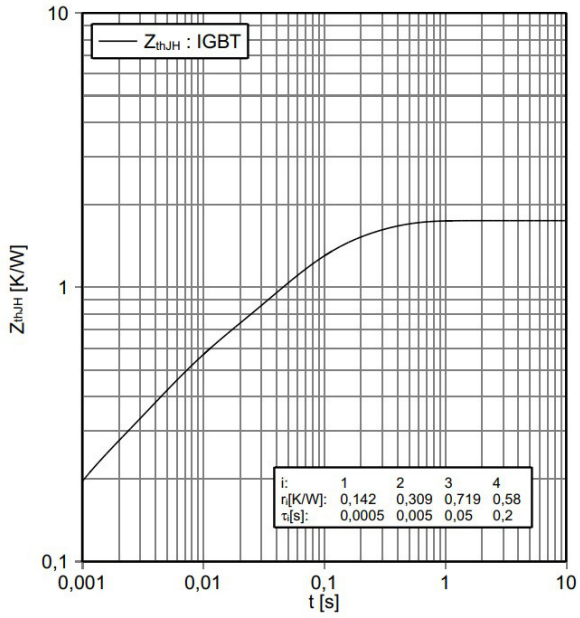

Figure 50 – IGBT transient thermal impedance. (INFINEON, 2020)

$$R_{th,h-a} < \frac{T_{vj(max)} - T_a - P_{Q,D}(R_{th,jc} + R_{th,ch})}{6(P_Q + P_D)}, \tag{5.6}$$

Source: Own authorship.

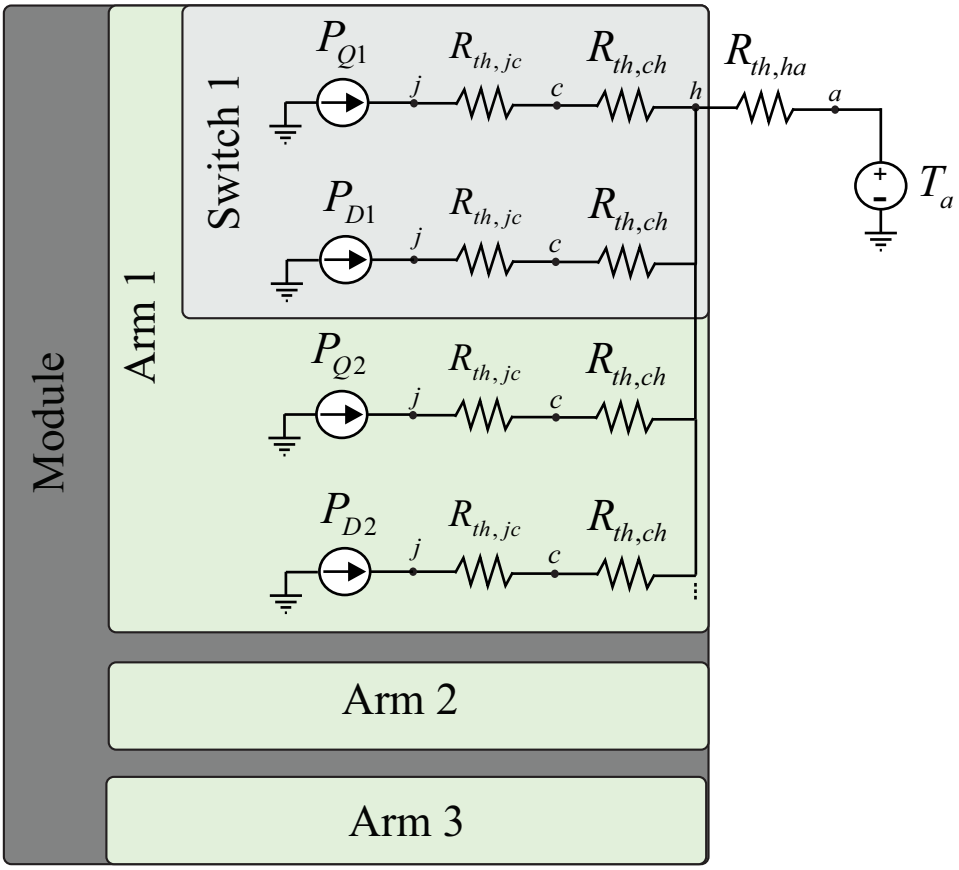

Figure 51 – Three-phase IGBT/diode thermal model.

where T_a is the ambient temperature and $T_{vj(max)}$ is the maximum junction temperature.

In this study, a maximum junction temperature of 105 °C and an ambient temperature of 40 °C are considered. The maximum junction temperature limit was established based on the rated operation of the PV system, considering only active power and no harmonic support. By considering the differences in the increase in losses, it is possible to determine the required heatsink volume in the final design.

5.2 Losses and volume evaluation

Accurate loss estimation is crucial for analyzing power density and efficiency. In the case of the chosen topology, the three-phase single-stage inverter, the main sources of losses are the semiconductor devices and passive filter elements. Losses from command circuits, conditioning, and control contribute only a small and fixed portion of total losses (KOLAR; BIELA; MINIBOCK, 2009; COTA, 2016). Additionally, losses in the dc-link capacitor can usually be neglected as the use of many electrolytic capacitors tends to minimize the equivalent resistance and corresponding losses.

This study focuses solely on losses associated with semiconductors and passive filter components. This is because losses in dc-link capacitors are minimal, and other losses are typically encountered in conventional or multifunctional inverter operations. The evaluation of the system's total volume involves the consideration of volumes that are common to both operational modes, including control circuits, signal conditioning and so on, as well as volumes that are influenced by the system's operation, namely, the cooling system, dc-link capacitors, and passive filter components.

5.2.1 Inductor Losses

The search for high-power density systems is a current challenge. Improvements in system components are made to increase switching frequency without sacrificing efficiency (VILLAR et al., 2009; SHIMIZU et al., 2011; FUJITA, 2011). These advances also result in more compact and lighter magnetic components. However, high switching frequency and reduced size can lead to excessive temperature rise in these components (MATSUMORI et al., 2016).

Power inductor losses consist of dc copper loss, ac copper loss, and core loss. The dc copper loss is due to conductor resistivity, while the ac winding power loss is caused by eddy current effects, such as skin and proximity effects (REATTI; KAZIMIERCZUK, 2002). Core losses result from hysteresis and eddy currents in the magnetic path (VILLAR et al., 2009). The computation of inductor losses depends on the winding and core physical characteristics, and the total inductor losses are used to estimate temperature rise in the component, ensuring that its thermal limit is not exceeded (MAGNETICS, 2020).

5.2.1.1 Cooper Losses

For the estimation of cooper losses, the total winding resistance and the joule losses must be calculated for each frequency, as described in Bahmani, Thiringer, and Ortega (2014). The design of power inductors is often complicated by the need to calculate the winding ac resistance, which is influenced by skin and proximity effects, particularly at high frequencies, as discussed in Ferreira (1992) and Bartoli et al. (1995).

The skin effect refers to the concentration of current in the outer edges of the conductor, causing its ac resistance to be higher than its dc resistance, particularly at high frequencies, as noted in reference Popovic (2000). The proximity effect, on the other hand, is caused by the interaction between currents flowing through a conductor and the magnetic field in adjacent conductors, and is exacerbated at high frequencies and when there is little spacing between coil turns, as explained in Popovic (2000).

Significant efforts have been made to develop accurate models of frequency behavior(FERREIRA, 1992; BARTOLI et al., 1995). Solid round conductors are commonly used in power inductor design due to their availability in a wide range of diameters at low cost (WOJDA;

KAZIMIERCZUK, 2013). In this work, copper loss estimation is based on the analytical solution presented in Bartoli et al. (1995), which accounts for skin and proximity effects by considering their orthogonality, as described in Ferreira (1992). This method has been improved by the introduction of porosity factors to enhance its accuracy (BAHMANI; THIRINGER; ORTEGA, 2014). The methodology adopted in this work is presented in detail in Appendix D.

Therefore, the power losses dissipated in the inductors winding can be estimated as:

$$P_w = R_{dc} i_{RMS}^2 + \sum_{h=1}^{\infty} R_w[h] i_{RMS}^2[h] \tag{5.7}$$

where R_{dc} is the winding dc resistance, i_{RMS} is the total RMS current through the inductor winding, $R_w[h]$ and $i_{RMS}[h]$ are the ac resistance and the current for the h^{th} harmonic order, respectively.

5.2.1.2 Core Losses

In the literature, various methods can be found for the calculation of magnetic core losses, including hysteresis models (JILES; ATHERTON, 1986), loss separation (KAPELLER; PLABNEGGER; GRAGGER, 2018), and empirical methods (STEINMETZ, 1984; LI; ABDALLAH; SULLIVAN, 2001; REINERT; BROCKMEYER; DE DONCKER, 2001; VENKATACHALAM et al., 2002). Methods based on hysteresis models can be further divided into those based on the Jiles-Atherton model (JILES; ATHERTON, 1986) and those based on the Preisach's work (HUI; ZHU, 1994). However, the practical use of these methodologies is limited due to the large number of empirical parameters required (REINERT; BROCKMEYER; DE DONCKER, 2001). The loss separation approach involves three separate components: static hysteresis, eddy current, and excess eddy-current losses. This method also requires increased computational effort and the use of empirical parameters (LI; ABDALLAH; SULLIVAN, 2001; VILLAR et al., 2009).

Empirical methods based on the Steinmetz equation (STEINMETZ, 1984) have proven to be the most practical tool for core loss estimation, as they only require three parameters, which are typically provided by the manufacturer. Over the years, different modifications of the Steinmetz equation have been developed, including the modified Steinmetz equation (MSE) and the generalized Steinmetz equation (GSE) (LI; ABDALLAH; SULLIVAN, 2001; REINERT; BROCKMEYER; DE DONCKER, 2001; VENKATACHALAM et al., 2002). Both methods allow the calculation of losses in non-sinusoidal waveforms, with GSE often providing higher accuracy (LI; ABDALLAH; SULLIVAN, 2001). This is due to the inclusion of the instantaneous flux density in the formulation, as discussed in Villar et al. (2009).

Finally, the improved generalized Steinmetz equation (iGSE) was introduced in Venkatachalam et al. (2002). This approach replaces the instantaneous flux density with its peak-to-peak value, taking into account the effects of magnetic variation history. In this work, iGSE is used for

the calculation of inductor core losses, as proposed in Venkatachalam et al. (2002). The iGSE states that:

$$P_v = \frac{1}{T}\int_0^T k_i \left|\frac{dB}{dt}\right|^{\alpha} (\Delta B)^{\beta-\alpha} dt, \tag{5.8}$$

where k_i is given by:

$$k_i = \frac{k}{(2\pi)^{\alpha-1}\int_0^{2\pi} |cos\theta|^{\alpha} 2^{\beta-\alpha} d\theta}, \tag{5.9}$$

where P_v is the time-average power loss per volume unit, and k, α, β are empirically determined material parameters, also called Steinmetz parameters. ΔB is peak-to-peak flux density within period (T) and θ is the flux density instantaneous phase angle.

The Steinmetz parameters can be obtained from the manufacturer's datasheet and are defined for every designed inductor, as specified in Section 5.1.2. The computational implementation of the iGSE equation can be found in the literature, as described in Sullivan (2006). In this work, the core losses algorithm was integrated with the proposed code.

5.2.1.3 Thermal Analysis

The design of the inductor's thermal properties is an important consideration (MATSUMORI et al., 2016). In theory, these properties are the main design limitation, as they specify the boundaries that the magnetic component can continuously operate without exceeding its critical temperature. According to Magnetics (2020), it is possible to estimate the inductor temperature rise as follows:

$$\Delta T_i(^{\circ}C) = \left(\frac{P_{ind}}{S_e}\right)^{0.833}, \tag{5.10}$$

where S_e is the surface area for core wound with a fill factor of 0.4 and P_{ind} is the inductor total losses.

Furthermore, since the wire resistance is temperature-dependent, it is possible to adjust the winding resistance accordingly. The ac resistance as a function of temperature is described in Bartoli et al. (1995), and is given by:

$$R_w[T] = 1 + (0.00393(T_a + \Delta T_i - 20)), \tag{5.11}$$

where T_a is the ambient temperature and 0.00393 is the copper temperature coefficient.

5.2.2 Capacitor Losses

The ESR of capacitors is an important parameter in determining the best product for a specific application (KOLAR; BIELA; MINIBOCK, 2009; BRAHAM et al., 2010). ESR represents the sum of all losses caused by the capacitor's dielectric and metal elements (BRAHAM et al., 2010). Each dielectric material has a corresponding loss factor. ESR is frequency-dependent and can be calculated using the capacitor's complex impedance (MAGNETICS, 2020), where the real part represents the ESR and the imaginary part represents the reactive part. The angle between the total impedance and its imaginary component is called the loss factor, which is numerically equal to the dissipation factor ($tan(\delta)$), as listed in the datasheet. Fig. 52 shows the complex impedance diagram.

Source: Own authorship.

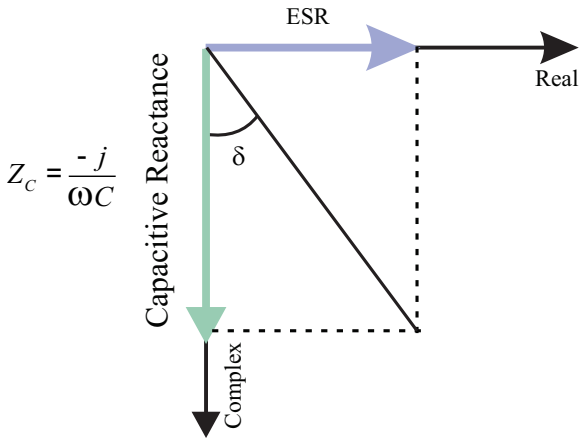

Figure 52 – Capacitors phase relationship.

Therefore, the ESR can be obtained as:

$$ESR[h] = |Z_C| tan(\delta), \tag{5.12}$$

where $ESR[h]$ is the equivalent series resistance for the h^{th} harmonic order. Therefore, the power dissipated in a capacitor can be calculated by:

$$P_{cap} = \sum_{h=1}^{\infty} ESR[h] i^2_{RMS}[h], \tag{5.13}$$

It is important to note that the ESR of the capacitors also varies with temperature (SILVEIRA BRITO, 2021). However, due to the minor impact of capacitor losses on the overall losses of the system, temperature-dependent ESR variation was not considered in this study.

5.2.3 Semiconductors Losses

During the operation of an inverter, the semiconductor devices are subjected to intrinsic power losses as they conduct electrical current and switch between on and off states at high voltage and current levels. These losses can be divided into two main categories: conduction and switching losses (DE ANDRADE et al., 2016; COTA, 2016; ABRANTES, 2016; SANTANA, 2018). Conduction losses arise when the collector current flows through the semiconductor module, along with a small voltage drop across the module. The necessary information for calculating conduction losses, such as the emitter collector voltage curve (v_{ce} versus i_c) for the IGBT and the direct voltage (v_f) versus direct current (i_f) for the diode, is usually provided in the datasheet (INFINEON, 2020). Fig. 53 - (a) and (d) present the (v_{ce} x i_c) and (v_f x i_f) curves, respectively.

Switching losses, on the other hand, result from the time delay during the devices' on (t_{don}) and off (t_{doff}) transitions. When turning on, a residual blocking voltage occurs briefly due to the delay as i_c rises from zero to its steady-state value. Conversely, during switching off, there is residual i_c while v_{ce} begins to rise. A similar situation occurs in the diode during the change to the blocking condition. The necessary data for calculating switching losses, such as the switching on and off (E_{on} and E_{off}) energies versus collector current for the IGBT and the recovery energy (E_{rec}) versus forward voltage for the diode, is also provided in the datasheet. Figs. 53 - (b) and (c) present ($E_{on,off}$ x i_c) and (E_{rec} x i_f) curves, respectively.

In addition, these device losses are dependent on the junction temperature (T_{vj}), which affects their performance (DE ANDRADE et al., 2016). The manufacturer typically provides information on the devices' thermal behavior, as discussed in Section 5.1.5. When compensating for harmonic currents, it is important to consider the harmonic characteristics, as the conduction and switching power losses depend on the harmonic amplitude, order, and phase angle (DE BARROS et al., 2018). To accurately compute the semiconductor devices' losses, an inverter model was designed in a simulation environment (PLECS). A lookup table was assembled to quantify the power losses in steady-state.

5.2.4 Cooling System

The cooling system of a converter usually constitutes a substantial portion of its total volume and weight (DROFENIK; KOLAR, 2006). The heatsink can be characterized by its power density, which is related to its thermal conductivity per unit volume, known as the Cooling System Performance Index (CSPI) (DROFENIK; LAIMER; KOLAR, 2005). According to Drofenik, Laimer, and Kolar (2005), commercial aluminum heatsinks have a CSPI of around 5 $W/(Kdm^3)$, while optimized copper heatsinks can have a CSPI of up to 31 $W/(Kdm^3)$.

The volume of the cooling system, in dm^3, can be calculated based on the CSPI as follows:

Source: Datasheet.

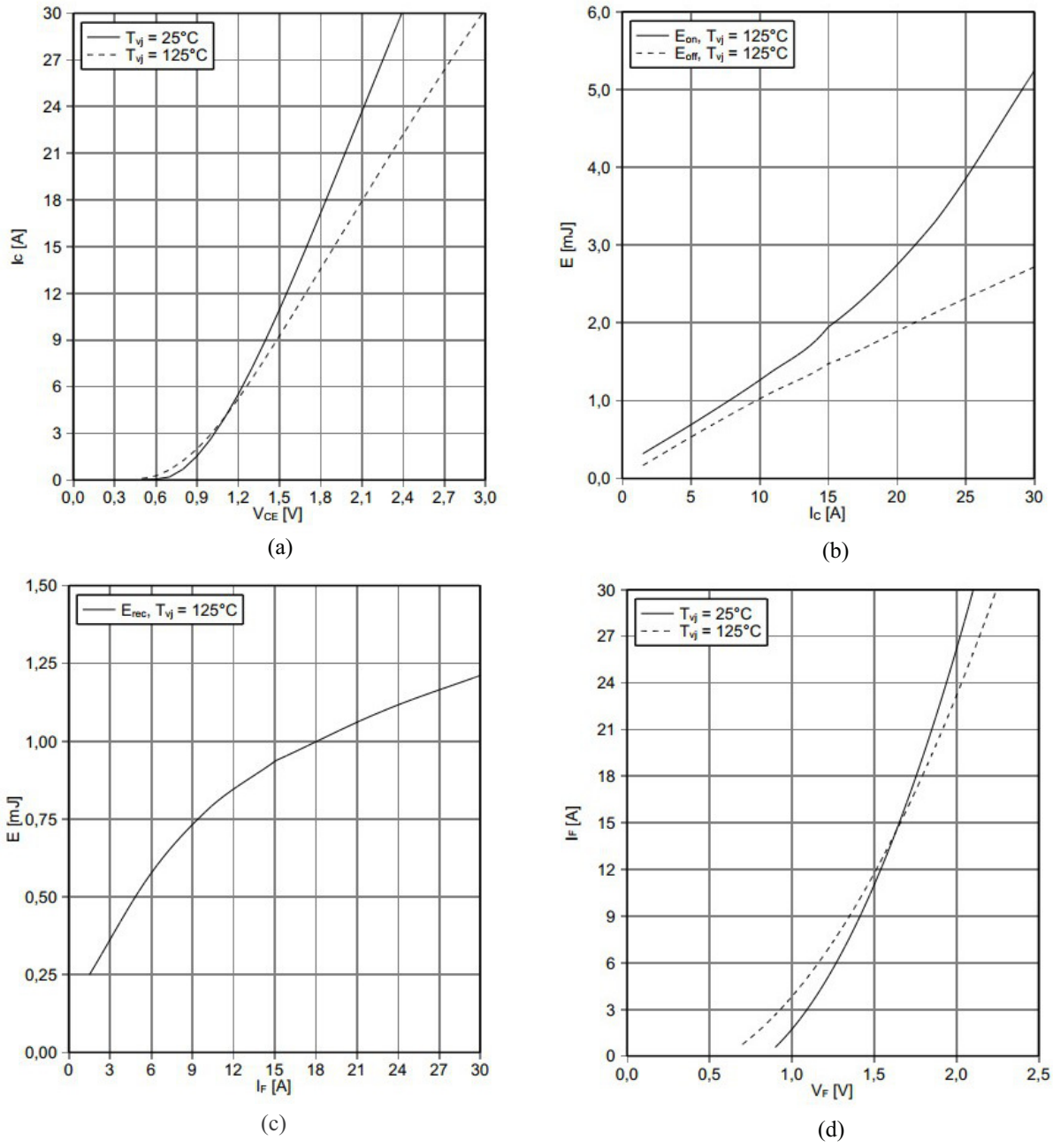

Figure 53 – Datasheet information. (a) v_{ce} x i_c; (b) v_f x i_f; (c) $E_{on,off}$ x i_c; and (d) E_{rec} x i_f. (INFINEON, 2020)

$$V_{CS} = \frac{1}{R_{th,h-a} CSPI}. \tag{5.14}$$

This thesis utilizes commercially available aluminum heat sinks, and thus a CSPI of 5 $W/(Kdm^3)$ was adopted. As a result, it is feasible to utilize Eq. 5.6, as outlined in Section 5.1.5, to approximate the total volume associated with the system's cooling system.

5.2.5 Volume Estimation

Finally, the volume estimation takes into account both the cooling system and the passive filter components. The following methodology is used to estimate the volume of each component:

- The inductor volume (V_{Ind}) information is provided in the datasheet (MAGNETICS, 2020) and requires the selected core and the fill factor adopted in design, as described in Section 5.1.2.
- Capacitor: The cylinder volume formula $V_{Cap} = \pi r_C^2 h_C$ is used to calculate the capacitor volume. Capacitors height (h_C) and radius (r_C) are provided in datasheet.
- The cooling system volume is estimated using the CSPI, as described in Section 5.2.4.

Therefore, the overall volume of the designed system is given by:

$$V_{total} = V_{Cap} + V_{Ind} + V_{CS}. \tag{5.15}$$

It is worth noting that this study does not consider aspects such as the volume of the PCB, connections, and the control part. Consequently, the analysis of the total volume only reflects a comparison of the objects under study, namely passive filter elements, the cooling system, and capacitors of the dc link. Moreover, power density can be obtained as:

$$PowerDensity = \frac{P_{max}}{V_{total}}. \tag{5.16}$$

5.3 Optimization methodology

An efficiency-power density Pareto optimization scheme has been proposed for the MI, as depicted in Fig. 54. The system specifications, such as the rated power, rated grid frequency, grid voltage, and dc-link voltage, are predetermined parameters. The photovoltaic inverter parameters used throughout this thesis are the same ones listed in Table 3. The design variables, such as switching frequency, LCL filter parameters, inductors, etc., are multiple parameters that can be identified. These variables were addressed in Section 5.1 and are appropriately referenced in Fig. 54. The electric power circuit modeling discussed in Section 3.2 provides the voltage/current information to the inductors and capacitors loss model. Furthermore, a lookup table is assembled using the software PLECS to evaluate the semiconductor losses. The volume and losses estimation are used to establish the Pareto design space, in this case study, there are n solutions, where n is the acceptable number of filter parameters.

Source: Own authorship.

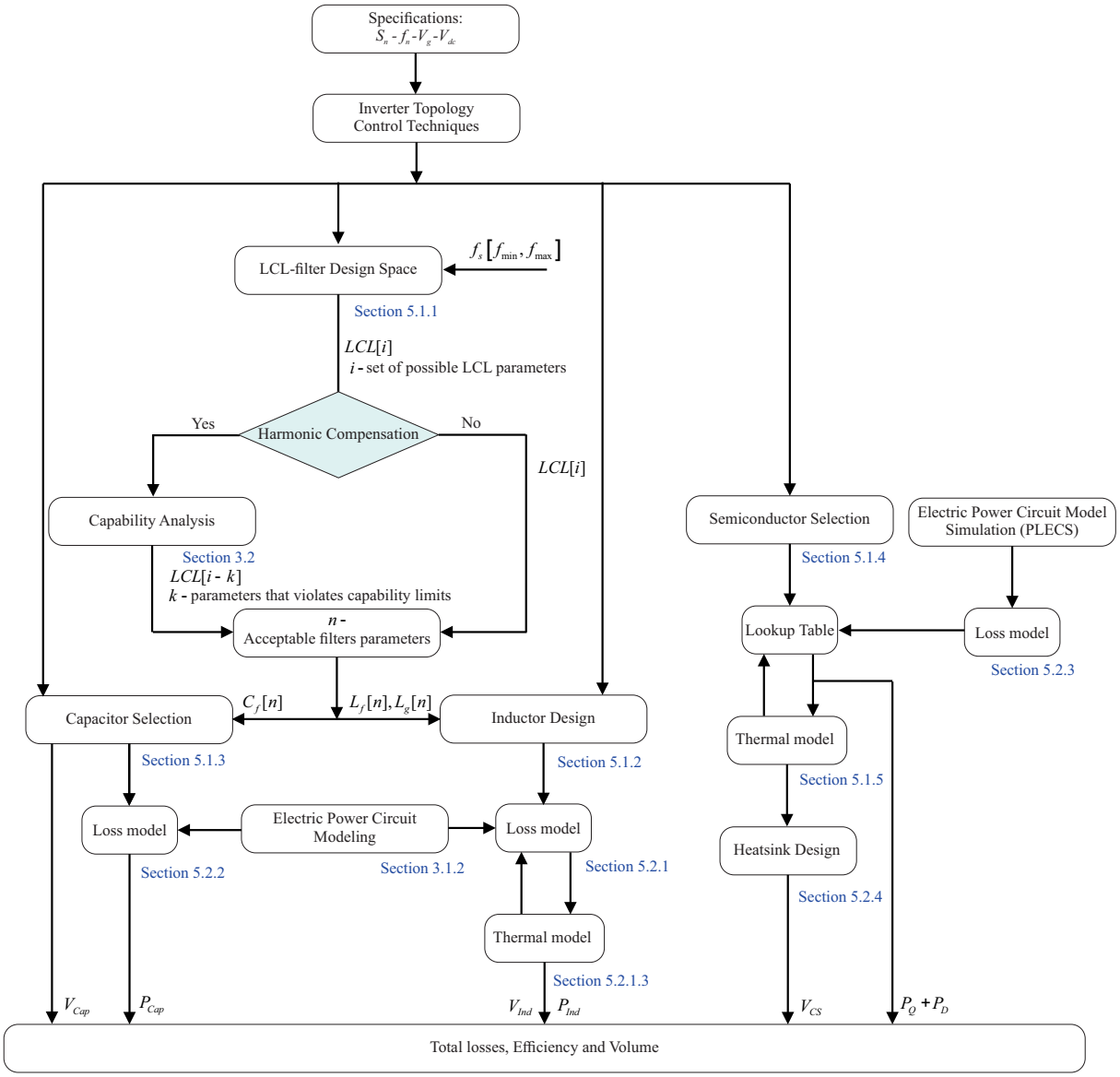

Figure 54 – Complete methodology to assess volume and losses block diagram.

The Pareto analysis is based on a graphical representation of solutions. The aim is to find a solution in the design space that satisfies efficiency and power density objectives. Generally, in most systems, there is no simultaneous optimal solution for all objective functions. Hence, there is a set of possible solutions, each of which is referred to as Pareto optimal and is characterized by not being able to improve one variable without worsening the other. The set of Pareto optimal solutions is known as the Pareto Front, which is graphically represented.

5.4 Simulation results

One of the objectives of this work is to compare the HCS in terms of filter parameter design and system losses. Two scenarios are compared: normal operation, where only 0.9 pu of

active power injection is considered, and multifunctional operation, where a condition of 0.9 pu of active power being injected into the grid and the harmonic current profile defined in Eq. 5.17 being compensated is considered.

$$i_{Sh}(t) = \frac{I_m}{5}\cos(5\omega_f t + \delta_{I5}) + \frac{I_m}{7}\cos(7\omega_f t + \delta_{I7}) + \frac{I_m}{11}\cos(11\omega_f t + \delta_{I11}) + \frac{I_m}{13}\cos(13\omega_f t + \delta_{I13}) \tag{5.17}$$

The harmonic profile consists of four harmonic orders, with the higher the harmonic order, the lower the harmonic current amplitude. As mentioned in Chapter 3, the limitations of inverter current and the limits imposed by the dc-link voltage must be taken into account. The first step is to apply the capability restriction in the multifunctional operation case. As mentioned in Chapter 3, the analysis of multiple harmonic orders is performed sequentially. Initially, the analysis is done for the 5^{th} harmonic, and if it can be compensated, the margin is secured, and the analysis moves on to the next harmonic. This process is repeated for each subsequent harmonic in turn.

Fig. 55 present two examples, one where the selected filter parameters allow for full support of the harmonic current profile (for 9.6 kHz design frequency and $r_q = 1.3$) and the other that restricts the support of the harmonic profile (for 7 kHz design frequency and $r_q = 1.6$).

Source: Own authorship.

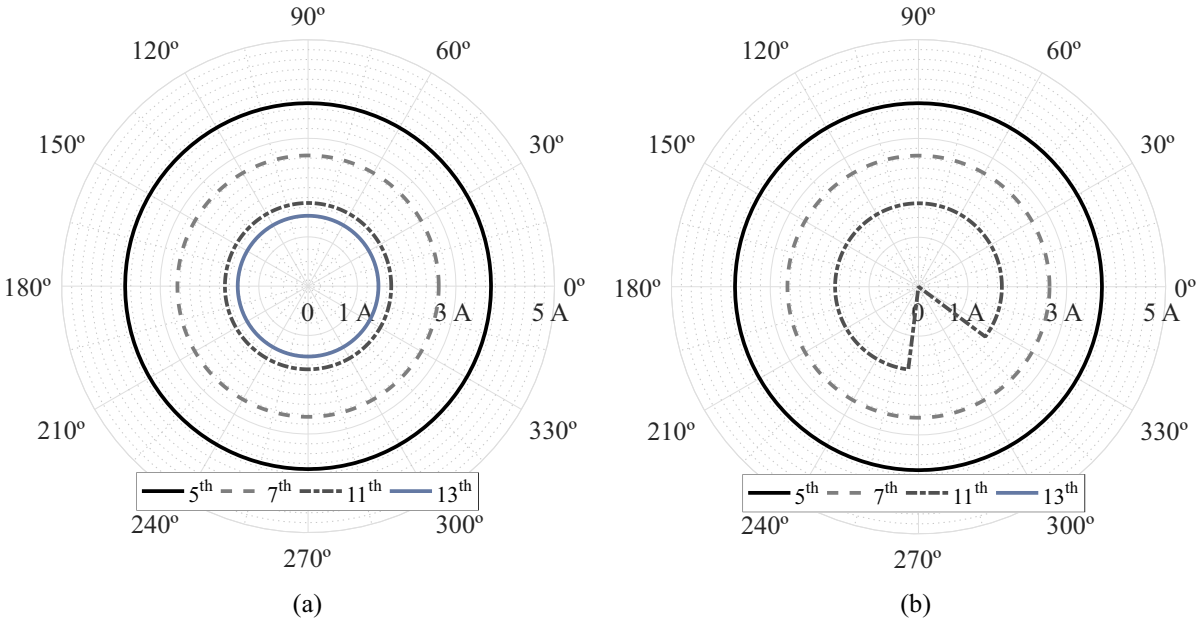

Figure 55 – Capability curves constraint examples: (a) $L_f = 0.45$ mH, $L_g = 0.45$ mH, and $C_f = 14.32$ μF; (b) $L_f = 0.63$ mH, $L_g = 0.63$ mH, $C_f = 17.37$ μF.

Fig. 55 - (b) shows that the 5^{th} and 7^{th} harmonic orders can be compensated, while the 11^{th} harmonic current can only be partially compensated. Also, in this scenario, it is not

possible to compensate the 13^{th} harmonic order current. The inverter capability constraint reduces the filter parameter possibilities by approximately 12.5%. The filter parameters designed for frequencies below 10 kHz are most affected by the capability constraint due to higher inductance values.

Additionally, this section presents the efficiency, loss distribution, and power density calculated for different switching frequencies for the normal operation and multifunctional operation cases. As mentioned in Section 5.1.1, there are several possible filter values for each frequency. Additionally, each inductor in this combination can be implemented with different characteristics due to the available number of cores and types of magnetic materials. Figs. 56 and 57 show the mean value of loss distribution, and Figs. 58 and 59 show the total losses, and power density, respectively, for each frequency. These results are based on all the different LCL filter configuration solutions used for that particular frequency.

Source: Own authorship.

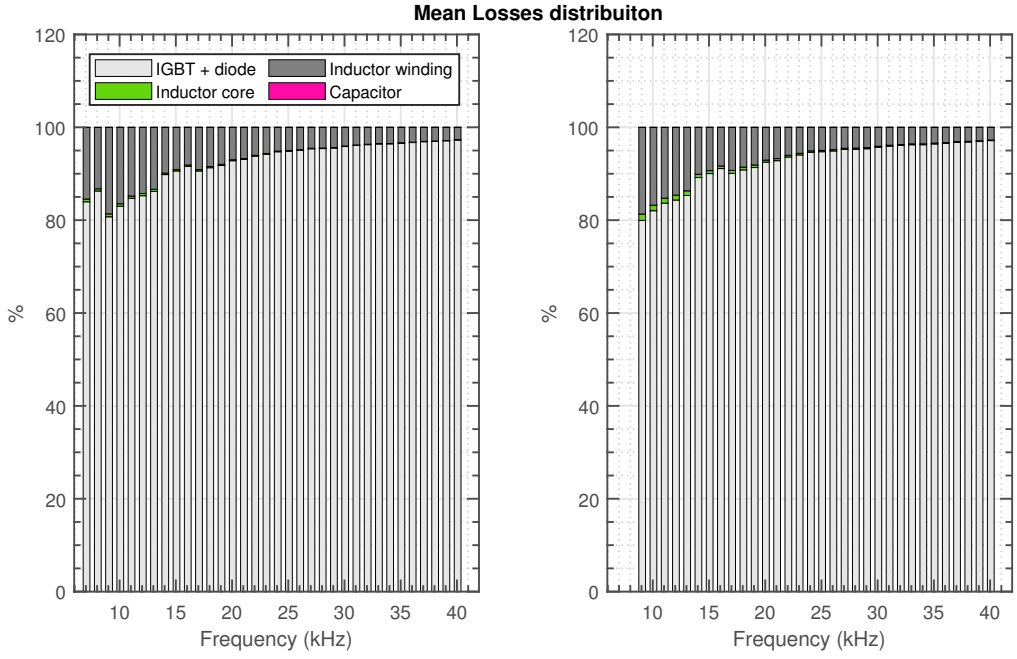

Figure 56 – Mean losses distribution: (a) without HCS; (b) with HCS.

It can be observed in Figs. 56-(b), 57, 58-(b), and 59-(b) that for multifunctional operation, the results are shown for frequencies approximately above 9 kHz. This is due to the fact that for lower frequencies, the inductors have higher inductances, which violate our capability constraint, as exemplified previously in Fig. 55-(b).

Fig. 56 presents the results obtained for inductor winding, inductor core, capacitor and semiconductor device mean losses, in percentage therms in relation to total losses, for different switching frequencies. Both normal and multifunctional operations reveal that the ratio of losses in semiconductors is directly proportional to the rise in switching frequency, primarily resulting

Source: Own authorship.

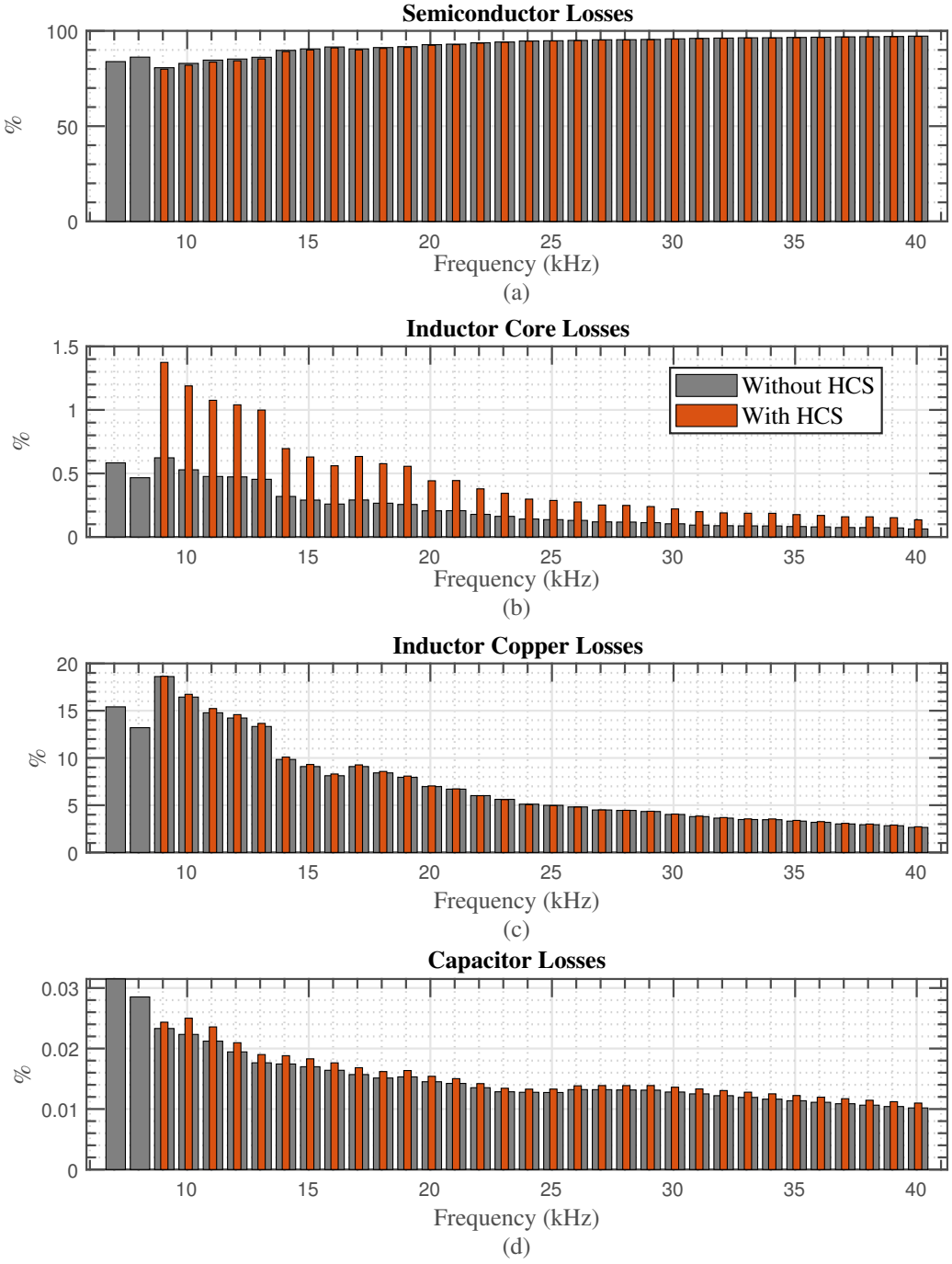

Figure 57 – Mean losses distribution: (a) Semiconductor; (b) Inductor Core; (c) Copper Losses; and (d) Capacitor Losses.

from switching losses. Figure 57 displays the losses separately, allowing for a more detailed

Source: Own authorship.

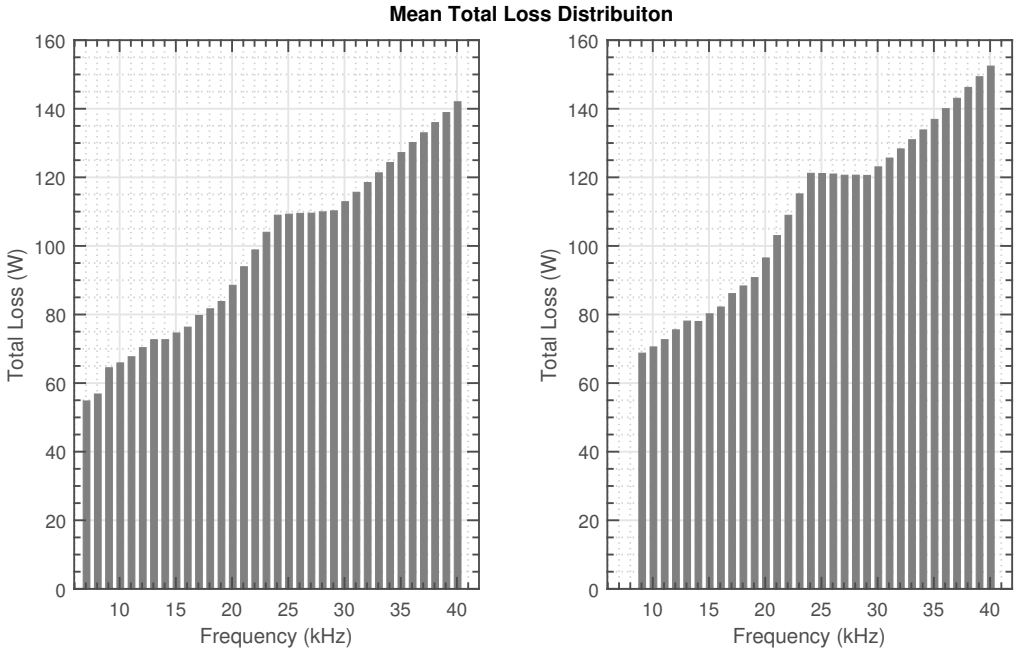

Figure 58 – Mean total losses distribution: (a) without HCS; (b) with HCS.

Source: Own authorship.

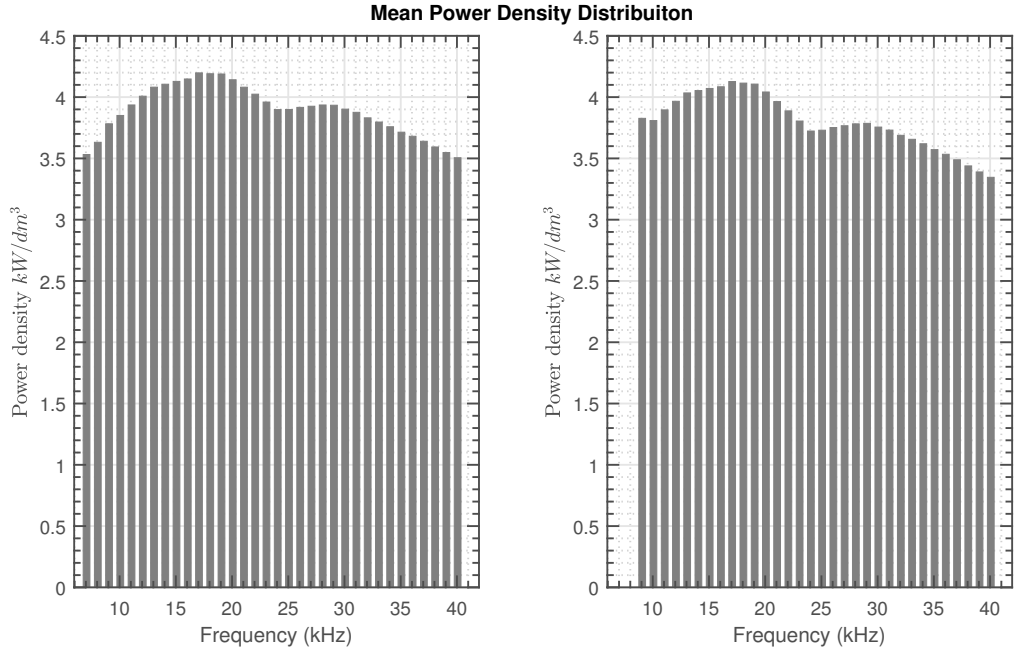

Figure 59 – Mean power density distribution: (a) without HCS; (b) with HCS.

examination of the differences between normal and multifunctional operation in terms of loss distribution.

Conversely, losses in the LCL filter elements exhibit a slight decrease due to the lower

inductance and capacitance values at higher frequencies resulting from an increase in switching frequency. At the same time, it should be emphasized that the losses in the capacitor are insignificant in comparison to the losses incurred by other components. Fig. 58 shows the total mean absolute values of system losses as a function of frequency. Upon analyzing Figs. 56 and 58, it becomes apparent that the behavior of losses, both with and without harmonic current support (HCS), is closely correlated with the switching frequency and losses in semiconductor devices. Additionally, it is observed that during multifunctional operation, the mean losses tend to be higher compared to operation without HCS.

Finally, Fig. 59 shows the average power density for each frequency. It is interesting to note the behavior of the power density distribution by frequency. Initially, for lower frequencies, there is an increase in power density, which can be explained by the relationship between the decrease in the volume of passive elements in contrast to the increase in the volume of the cooling system. For higher frequencies, however, this ratio is already offset, and the increase in the volume of the cooling system is much greater than the decrease in the volume of passive elements in the filter.

Although it does not influence the optimization process, which is the main focus of this chapter, analyzing these figures is important to understand the real behavior of the system under the imposed degrees of freedom (such as switching frequency, LCL filter, inductor design, and type of operation).

The Pareto Front is the set of optimal solutions that cannot be improved in one objective without worsening at least one other objective. The Pareto Front can be visualized as a plot, with each point representing a particular solution that is optimal in some sense. Fig. 60 presents the Pareto Front plotted on a scatter plot (in red) with all the possible LCL filter solutions. The points on the Pareto Front are highlighted in red. Additionally, a decision-making function developed allows the user to select their preferred combination of objectives for selecting the best point from the Pareto Front. The function relies on a weighted average approach and presents three alternatives: choosing the highest weighted value in terms of objective power density, selecting the highest weighted value in terms of objective efficiency, or opting for equal weights that maximize both power density and efficiency (referred to as Cases A, B, and C, respectively). The function was successfully applied to the Pareto Front generated in a previous step. The results obtained using the decision-making function show that the optimal solution depends on the weights assigned to each objective. By changing the weights, it is possible to select a different point from the Pareto Front that best meets their specific needs and preferences.

Table 11 presents the values of the Pareto Front for the three objectives, A, B and C, and the resulting optimal solution selected by the decision-making function. The table provides a clear overview of the range of Pareto-optimal solutions and how the optimal solution changes depending on the weight assigned to each objective. The table can be a useful tool for decision-makers to explore the trade-offs among different objectives and select the optimal solution that

Source: Own authorship.

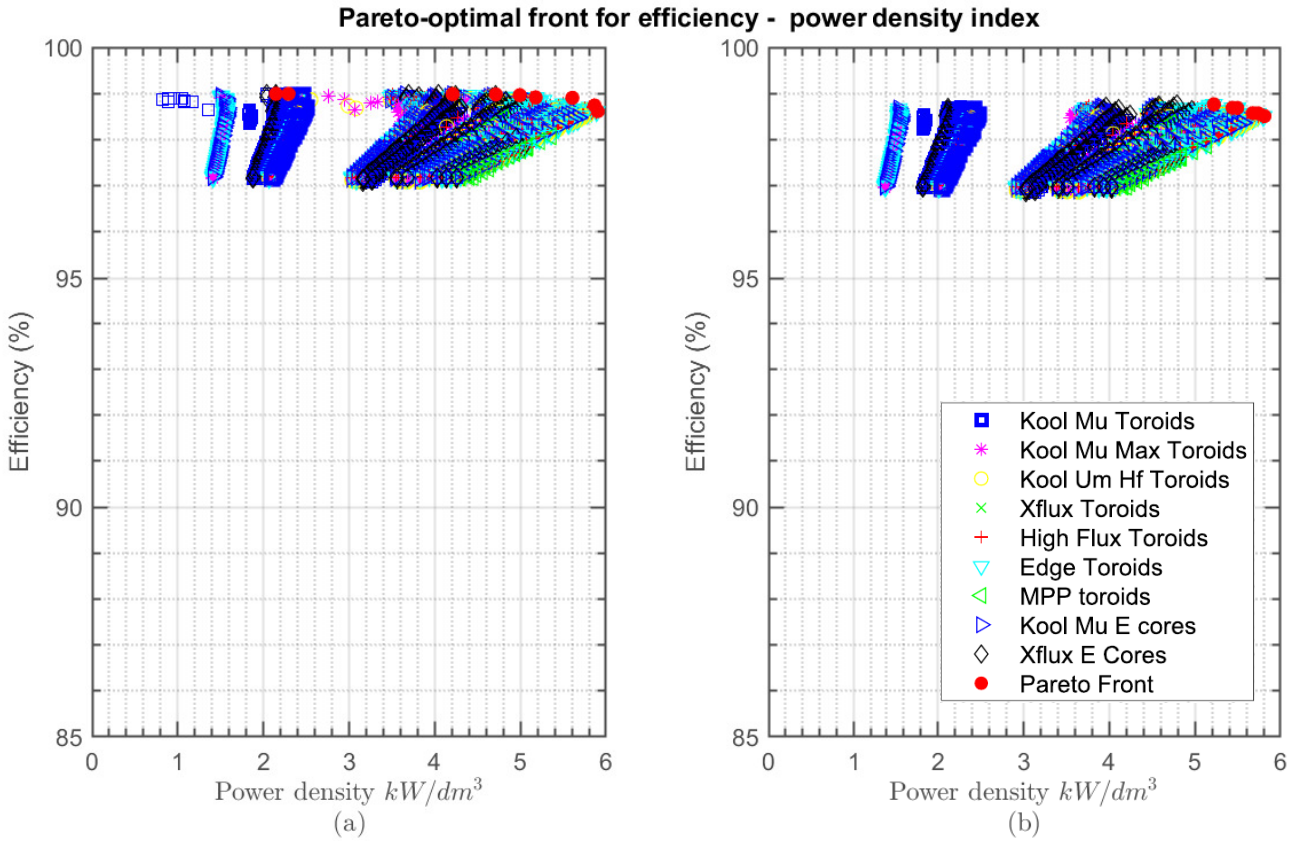

Figure 60 – Pareto Front solution: (a) without HC; and (b) with HC.

best meets their specific needs and preferences. Additionally, Table 12 presents the constructive characteristics of the inductors that were selected based on the Pareto Front and decision making-algorithm.

5.5 Discussion

The filter optimization allows designers to balance multiple performance metrics, including efficiency, grid integration and volume. As shown in the previous analysis, the LCL filter plays a significant role in HCS. It is important to note that projects that do not consider multifunctional operation may face physical and/or control limitations.

Upon analyzing the scenario, it becomes apparent that the operating conditions yield comparable efficiency and power density values, this can be accomplished by simply modifying the material utilized to manufacture the magnetic cores of the filter inductors. An interesting result obtained for case A reveals that the same configuration of LCL filter can be used for both normal operation and multifunctional operation. Additionally, it is worth noting that the difference in efficiency in this comparative case A is attributed to the increased losses in the passive elements of the LCL filter and the dc link due to HCS. Also, the decrease in power

Table 11 – Optimal filter parameters. (A - highest weighted value in terms of objective power density; B - highest weighted value in terms of objective efficiency; and C - opting for equal weights.)

	A	B	C
Normal operation			
Inductance	0.31 mH	0.54 mH	0.70 mH
Capacitance	19.6 μF	29.64 μF	29.6 μF
Frequency	13.60 kHz	8.06 kHz	7.06 kHz
Power density	5.90 kW/dm^3	5.60 kW/dm^3	2.14 kW/dm^3
Efficiency	98.61%	98.90%	99.01%
Multifunctional operation			
Inductance	0.31 mH	0.42 mH	0.44 mH
Capacitance	19.6 μF	28.2 μF	28.2 μF
Frequency	13.60 kHz	9.06 kHz	9.06 kHz
Power density	5.81 kW/dm^3	5.49 kW/dm^3	5.22 dm^3/kW
Efficiency	98.50%	98.68%	98.76%

Table 12 – Optimal filter parameters. (A - highest weighted value in terms of objective power density; B - highest weighted value in terms of objective efficiency; and C - opting for equal weights.)

		A	B	C
Normal operation				
Inductor	Material	XFlux Toroids	Xflux Toroids	Kool Mu E cores
	Part number	78094	78110	114040
	Area	134	144	1220
	Volume	15600	20700	262000
	Number of turns	44	48	72
Multifunctional operation				
Inductor	Material	Xflux Toroids	High Flux Toroids	High Flux Toroids
	Part number	78094	58110	58195
	Area	134	144	221
	Volume	15600	20700	28600
	Number of turns	44	62	229

density during HCS is a result of the increased heat sink requirements, as harmonic support also leads to higher switching and conduction losses. Consequently, a larger heat sink is necessary to maintain the same thermal stress on the semiconductor elements.

Moreover, the transition to scenario C leads to an efficiency enhancement of approximately 0.25-0.4%, depending on the type of operation, at the expense of considerably smaller power density values. Although it may appear unconventional at first, opting for a slightly more efficient solution can yield substantial cost savings over the lifetime of the system, particularly when additional installation space is available. It is important to acknowledge that the findings presented in this study are representative of the specific conditions and limitations outlined in the text. By following the same procedures and guidelines used in this study, it is feasible to apply the methodology to other systems with varying conditions and/or restrictions.

5.6 Chapter conclusions

The optimization data presented offers an interesting insight: without undergoing an optimization process, technically acceptable design conditions may result in losses in both efficiency and power density. In the studied case, these losses can reach up to 2-3% in efficiency and 5 kW/dm^3 in power density.

Concerning the switching frequency, it is evident that when prioritizing power density, a higher switching frequency is typically employed. This frequency represents the turning point where the volume of passive components in the filter decreases, while the volume of the heatsink increases due to elevated switching losses. For normal operation, the optimization results indicate that conditions A and B are more viable. Condition C exhibits a significant decline in power density for a marginal 0.11% gain in efficiency. On the other hand, in multifunctional operation, a balance is observed among the three presented conditions. Among them, condition B, which values a compromise between optimization parameters, appears more suitable, yielding an efficiency increase of 0.18% and a decrease of 0.32 kW/dm^3.

Furthermore, the findings suggest that it is possible to design a photovoltaic (PV) system capable of providing HCS without significantly compromising its overall performance. The proposed methodology can serve as a valuable tool to guide engineers and researchers in effectively integrating HCS into PV systems, while still maintaining their desired performance levels.

6 Conclusions and Future Research

6.1 Conclusions

This thesis fulfilled its primary objective of examining the influence of HCS on the performance of grid-tied PV systems. It accomplished this by analyzing the impact of HCS on system operation, including operating limits, losses, and deviations from normal operation. The study provides valuable insights and guidelines for evaluating and enhancing the operational status of multifunctional PV systems. In Chapter 2, which focuses on MI modeling, control, and design, a comprehensive review of renewable generation systems with HCS capability is presented. This exploration serves as the foundation for comprehending the key principles and methodologies involved in achieving HCS in PV systems.

The objective of defining MI capability curves, which serve as safety boundaries for equipment operation it is presented in Chapters 3 and 4. It is accomplished by developing an algorithm that creates MI capability curves based on inverter limits. The algorithm's effectiveness was validated through simulations in PLECS software and experiments on a test bench, providing a practical tool for assessing system operating limits. Furthermore, the analysis of nonlinearities in inductors has highlighted the detrimental impact of inductor saturation on the performance and stability of PV systems during HCS. The proposed PMR control approach has effectively mitigated the effects of inductor saturation, ensuring compliance with technical standards regarding THD limits.

In summary, the overall results of the capability curves analysis highlight two key points. First, in order to achieve HCS, it is necessary to ensure a sufficient dc-link voltage. Second, the LCL filter inductors play a crucial role in determining the amount of voltage required on the dc link. Therefore, careful consideration and appropriate design of the LCL filter inductors are essential in determining the available dc-link voltage. Moreover, these indicators pave the way for evaluating various LCL filter designs. It is important to note that a higher voltage on the dc link leads to increased losses. Different LCL filter designs result in varying values of passive elements, which directly impact the definition of losses and system volume. Therefore, exploring and analyzing different LCL filter designs becomes crucial in optimizing the trade-off between losses and system size.

Finally, in Chapter 5, a comparative analysis between a system designed for HCS and a system solely focused on active power injection into the grid was conducted. This analysis provided valuable conclusions on the benefits and trade-offs of integrating HCS capabilities into grid-connected PV systems. Regarding MI filter design and analysis, the thesis proposed and compared passive filter designs considering criteria such as losses and power density. Pareto

optimization analyses is employed to identify optimal filter configurations, enabling designers to make informed decisions in selecting filters that enhance HCS while balancing performance metrics. Preliminary observations indicate that design conditions that are technically acceptable but lack optimization may result in efficiency and power density losses. These findings highlight the importance of filter optimization to attain the desired performance metrics for grid integration.

In a particular scenario analyzed in the study (case A), by maintaining the passive filter conditions and switching frequency constant, the multifunctional operation shows a slight decrease of 0.11% in efficiency and a reduction of $0.09\ kW/dm^3$ in power density. However, transitioning to scenario C yields an efficiency improvement ranging from approximately 0.25% to 0.4%, depending on the specific type of operation. It should be noted that this efficiency enhancement comes at the cost of significantly lower power density values. The optimization of the LCL filter has demonstrated that it is possible to achieve enhanced capability for HCS without compromising system efficiency. The trade-off analysis has shown that a careful balance between efficiency and power density needs to be considered in the design process.

The outcomes of this research have practical implications for engineers and researchers involved in the design and integration of HCS capabilities into PV systems. The presented methodologies and guidelines can facilitate the development of efficient, reliable, and harmonically compliant PV systems that contribute to the stability and sustainability of the electrical grid. As the field of renewable energy continues to evolve, future research can build upon this work by exploring alternative system configurations, control strategies, and optimization techniques, further expanding the knowledge and applications of HCS in PV systems.

6.2 Future research

Although numerous aspects have been investigated and documented in this present PhD. thesis, there are still ample scope for further improvement. The following studies could be addressed in future research:

- The design of a controller that considers the voltage capability constraints of the dc-link and inverter current.
- Experimental validation of the capability algorithm with nonlinear inductor behavior with the PMR with adjustable gain proposed.
- A comparative analysis of the outcomes obtained from optimizing the LCL filter components with another methodology existing in the literature.
- Experimental power losses validation: a topic do address is the losses calculation methodology and the optimization process experimental validation. Thus, it is proposed a test

bench assembly to perform the comparisons between a filter designed for active power injection and another optimized for multifunctional operation.

- A study to assess the limitations associated with control and modulation during HCS.

Considering these and various other prospects for future research, the author sincerely hopes that this research project will be pursued beyond the scope of the present thesis.

References

ABRANTES, Rafael Castro e. **Desenvolvimento de ferramentas para o cálculo de perdas em conversores estáticos: controle de conversores estáticos com a plataforma dSPACE**. 2016. PhD thesis – Universidade Federal de Minas Gerais. Cit. on pp. 98, 105.

ABU-RUB, Haitham; MALINOWSKI, Mariusz; AL-HADDAD, Kamal. AC–DC–AC Converters for Distributed Power Generation Systems. In: POWER Electronics for Renewable Energy Systems, Transportation and Industrial Applications. [S.l.: s.n.], 2014. P. 319–364. DOI: 10.1002/9781118755525.ch11. Cit. on p. 96.

ADIB, A.; LAMB, J.; MIRAFZAL, B. Ancillary Services via VSIs in Microgrids With Maximum DC-Bus Voltage Utilization. **IEEE Transactions on Industry Applications**, v. 55, n. 1, p. 648–658, Jan. 2019. DOI: 10.1109/TIA.2018.2865483. Cit. on p. 53.

AKAGI, H. Modern active filters and traditional passive filters. **Bulletin of The Polish Academy of Sciences-technical Sciences**, v. 54, p. 255–269, 2006. Cit. on p. 25.

ALAMRI, Basem; ALHARBI, Yasser Mohammed. A Framework for Optimum Determination of LCL-Filter Parameters for N-Level Voltage Source Inverters Using Heuristic Approach. **IEEE Access**, v. 8, p. 209212–209223, 2020. DOI: 10.1109/ACCESS.2020.3038583. Cit. on p. 46.

ALI, Z. et al. Multi-functional distributed generation control scheme for improving the grid power quality. **IET Power Electronics**, v. 12, n. 1, p. 30–43, 2019. DOI: 10.1049/iet-pel.2018.5177. Cit. on pp. 33, 40.

ALONSO, A. M. et al. Optimized Exploitation of Ancillary Services: Compensation of Reactive, Unbalance and Harmonic Currents Based on Particle Swarm Optimization. **IEEE Latin America Transactions**, v. 19, n. 02, p. 314–325, 2021. DOI: 10.1109/TLA.2021.9443074. Cit. on pp. 27, 28.

ALONSO, Augusto Matheus dos Santos et al. A selective harmonic compensation and power control approach exploiting distributed electronic converters in microgrids. **International Journal of Electrical Power and Energy Systems**, v. 115, p. 105452, 2020. ISSN 0142-0615. DOI: https://doi.org/10.1016/j.ijepes.2019.105452. Cit. on pp. 27, 36, 38.

ANDRESEN, Markus; LISERRE, Marco. Impact of active thermal management on power electronics design. **Microelectronics Reliability**, v. 54, Aug. 2014. DOI: 10.1016/j.microrel.2014.07.069. Cit. on p. 51.

ANEEL. **Procedimentos de Distribuicao de Energia Eletrica no sistema eletrico nacional (PRODIST): Modulo 8 - Qualidade da Energia Eletrica**. [S.l.], 2011. P. 1–88. Cit. on p. 23.

ANTUNES, Felipe; XAVIER, Lucas S., et al. Comparison of harmonic detection methods applied in a photovoltaic inverter during harmonic current compensation. In: 2017 Brazilian Power Electronics Conference (COBEP). [S.l.: s.n.], 2017. P. 1–6. DOI: 10.1109/COBEP.2017.8257375. Cit. on p. 44.

ANTUNES, H. M. A.; PIRES, Igor A.; SILVA, S. M. Evaluation of Series and Parallel Hybrid Filters Applied to Hot Strip Mills With Cycloconverters. **IEEE Transactions on Industry Applications**, v. 55, n. 6, p. 6643–6651, 2019. DOI: 10.1109/TIA.2019.2932966. Cit. on p. 25.

ANTUNES; SILVA, S. M., et al. A new multifunctional converter based on a series compensator applied to AC microgrids. **International Journal of Electrical Power and Energy Systems**, v. 102, p. 160–170, 2018. ISSN 0142-0615. DOI: https://doi.org/10.1016/j.ijepes.2018.04.013. Cit. on pp. 34, 36, 38, 39.

ANURAG, A.; YANG, Y.; BLAABJERG, F. Thermal Performance and Reliability Analysis of Single-Phase PV Inverters With Reactive Power Injection Outside Feed-In Operating Hours. **IEEE Journal of Emerging and Selected Topics in Power Electronics**, v. 3, n. 4, p. 870–880, Dec. 2015. DOI: 10.1109/JESTPE.2015.2428432. Cit. on p. 28.

ASHRAF, Muhammad Noman; KHAN, Reyyan Ahmad; CHOI, Woojin. A Novel Selective Harmonic Compensation Method for Single-Phase Grid-Connected Inverters. **IEEE Transactions on Industrial Electronics**, v. 68, n. 6, p. 4848–4858, 2021. DOI: 10.1109/TIE.2020.2989723. Cit. on p. 28.

ASIMINOAEI, L.; BLAABJERG, F.; HANSEN, S. Evaluation of harmonic detection methods for active power filter applications. In: TWENTIETH Annual IEEE Applied Power Electronics Conference and Exposition, 2005. APEC 2005. [S.l.: s.n.], 2005. v. 1, 635–641 vol. 1. DOI: 10.1109/APEC.2005.1453014. Cit. on p. 43.

ASIMINOAEL, Lucian; BLAABJERG, Frede; HANSEN, Steffan. Detection is key - Harmonic detection methods for active power filter applications. **IEEE Industry Applications Magazine**, v. 13, n. 4, p. 22–33, 2007. DOI: 10.1109/MIA.2007.4283506.

AZRI, Maaspaliza; ABD RAHIM, Nasrudin. Design analysis of low-pass passive filter in single-phase grid-connected transformerless inverter, June 2011. DOI: 10.1109/CET.2011.6041489. Cit. on p. 45.

BACKLUND, B. et al. Topologies, voltage ratings and state of the art high power semiconductor devices for medium voltage wind energy conversion. In: 2009 IEEE Power Electronics and Machines in Wind Applications. [S.l.: s.n.], June 2009. P. 1–6. DOI: 10.1109/PEMWA.2009.5208365. Cit. on p. 64.

BAHMANI, M. Amin; THIRINGER, Torbjörn; ORTEGA, Hector. An Accurate Pseudoempirical Model of Winding Loss Calculation in HF Foil and Round Conductors in Switchmode Magnetics. **IEEE Transactions on Power Electronics**, v. 29, n. 8, p. 4231–4246, 2014. DOI: 10.1109/TPEL.2013.2292593. Cit. on pp. 101, 102, 145.

BALACHANDRAN, Rahul; KUMARI, A. Thermal analysis for optimized selection of cooling techniques for SiC devices in high frequency switching applications. **IOP Conference Series: Materials Science and Engineering**, v. 577, p. 012143, Dec. 2019. DOI: 10.1088/1757-899X/577/1/012143. Cit. on p. 98.

BARTOLI, M. et al. Modelling Winding Losses in High-Frequency Power inductors. **J. Circuits Syst. Comput.**, v. 5, p. 607–626, 1995. Cit. on pp. 101–103, 145, 146.

BASTIDAS-RODRIGUEZ, Juan; RAMOS-PAJA, Carlos. Types of inverters and topologies for microgrid applications. **UIS Inenierías**, v. 16, p. 7–14, Jan. 2017. DOI: 10.18273/revuin.v16n1-2017001. Cit. on p. 37.

BERES, R. N. et al. A Review of Passive Power Filters for Three-Phase Grid-Connected Voltage-Source Converters. **IEEE Journal of Emerging and Selected Topics in Power Electronics**, v. 4, n. 1, p. 54–69, 2016. DOI: 10.1109/JESTPE.2015.2507203. Cit. on pp. 45, 51.

BERTOTTI, G. General properties of power losses in soft ferromagnetic materials. **IEEE Transactions on Magnetics**, v. 24, n. 1, p. 621–630, 1988. DOI: 10.1109/20.43994.

BIERHOFF, M. H.; FUCHS, F. W. Semiconductor losses in voltage source and current source IGBT converters based on analytical derivation. In: IEEE 35th Annu. Power Electron. Specialists Conf. [S.l.: s.n.], June 2004. v. 4, 2836–2842 vol.4. DOI: 10.1109/PESC.2004.1355283. Cit. on p. 64.

BIGHASH, Esmaeil Zangeneh et al. Adaptive-Harmonic Compensation in Residential Distribution Grid by Roof-Top PV Systems. **IEEE Journal of Emerging and Selected Topics in Power Electronics**, v. 6, n. 4, p. 2098–2108, 2018. DOI: 10.1109/JESTPE.2018.2792303. Cit. on p. 27.

BLAABJERG, F.; NEACSU, D.O.; PEDERSEN, J.K. Adaptive SVM to compensate DC-link voltage ripple for four-switch three-phase voltage-source inverters. **IEEE Transactions on Power Electronics**, v. 14, n. 4, p. 743–752, 1999. DOI: 10.1109/63.774214. Cit. on p. 35.

BORTIS, D.; NEUMAYR, D.; KOLAR, J. W. Pareto optimization and comparative evaluation of inverter concepts considered for the GOOGLE Little Box Challenge. In: 2016 IEEE 17th Workshop on Control and Modeling for Power Electronics (COMPEL). [S.l.: s.n.], 2016. P. 1–5. DOI: 10.1109/COMPEL.2016.7556767. Cit. on p. 93.

BOUKEZATA, B. et al. Predictive current control in multifunctional grid connected inverter interfaced by PV system. **Solar Energy**, v. 139, p. 130–141, 2016. ISSN 0038-092X. DOI: https://doi.org/10.1016/j.solener.2016.09.029. Cit. on p. 40.

BRAHAM, Ahmed et al. Recent Developments in Fault Detection and Power Loss Estimation of Electrolytic Capacitors. **IEEE Transactions on Power Electronics**, v. 25, n. 1, p. 33–43, 2010. DOI: 10.1109/TPEL.2009.2026749. Cit. on p. 104.

BRASIL. **Lei n.14300, de 6 de janeiro de 2022. Institui o marco legal da microgeração e minigeração distribuída, o Sistema de Compensação de Energia Elétrica (SCEE) e o Programa de Energia Renovável Social (PERS).** [S.l.], 2022. Cit. on p. 26.

BROCKMEYER, A.; SCHULTING, L. Modelling of dynamic losses in magnetic material. In: 1993 Fifth European Conference on Power Electronics and Applications. [S.l.: s.n.], 1993. 112–117 vol.3.

BUSO, Simone; CALDOGNETTO, Tommaso; BRANDAO, Danilo Iglesias. Dead-Beat Current Controller for Voltage-Source Converters With Improved Large-Signal Response. **IEEE Transactions on Industry Applications**, v. 52, n. 2, p. 1588–1596, 2016. DOI: 10.1109/TIA.2015.2488644. Cit. on p. 39.

BUSO, Simone; CALDOGNETTO, Tommaso; LIU, Qing. Analysis and Experimental Characterization of a Large-Bandwidth Triple-Loop Controller for Grid-Tied Inverters. **IEEE Transactions on Power Electronics**, v. 34, n. 2, p. 1936–1949, 2019. DOI: 10.1109/TPEL.2018.2835158. Cit. on p. 39.

BUYUK, Mehmet et al. Topologies, generalized designs, passive and active damping methods of switching ripple filters for voltage source inverter: A comprehensive review. **Renewable and Sustainable Energy Reviews**, v. 62, p. 46–69, 2016. ISSN 1364-0321. DOI: https://doi.org/10.1016/j.rser.2016.04.006. Cit. on pp. 45, 46, 51.

CALLEGARI, J.M.S.; CUPERTINO, A.F.; FERREIRA, V.N.; BRITO, E.M.S., et al. Adaptive dc-link voltage control strategy to increase PV inverter lifetime. **Microelectronics Reliability**, v. 100-101, p. 113439, 2019. 30th European Symposium on Reliability of Electron Devices, Failure Physics and Analysis. ISSN 0026-2714. DOI: https://doi.org/10.1016/j.microrel.2019.113439. Available from: <https://www.sciencedirect.com/science/article/pii/S0026271419305426>. Cit. on p. 64.

CALLEGARI, J.M.S.; SILVA, M.P., et al. Lifetime evaluation of three-phase multifunctional PV inverters with reactive power compensation. **Electric Power Systems Research**, v. 175, n. 1, Jan. 2019. ISSN 0378-7796. DOI: 10.1016/j.epsr.2019.105873. Cit. on pp. 27–29.

CALLEGARI, João Marcus Soares; CUPERTINO, Allan Fagner; FERREIRA, Victor de Nazareth; PEREIRA, Heverton Augusto. Minimum DC-Link Voltage Control for Efficiency and Reliability Improvement in PV Inverters. **IEEE Transactions on Power Electronics**, v. 36, n. 5, p. 5512–5520, 2021. DOI: 10.1109/TPEL.2020.3032040. Cit. on p. 64.

CAMPANHOL, Leonardo Bruno Garcia et al. Single-Stage Three-Phase Grid-Tied PV System With Universal Filtering Capability Applied to DG Systems and AC Microgrids. **IEEE Transactions on Power Electronics**, v. 32, n. 12, p. 9131–9142, 2017. DOI: 10.1109/TPEL.2017.2659381. Cit. on p. 28.

CHEN, Dongdong et al. A harmonics detection method based on improved comb filter of sliding discrete Fourier for grid-tied inverter. **Energy Reports**, v. 6, p. 1303–1311, 2020. 2020 The 7th International Conference on Power and Energy Systems Engineering. ISSN 2352-4847. DOI: https://doi.org/10.1016/j.egyr.2020.11.029. Cit. on p. 42.

COSTA, Israel D. L. et al. Analysis of Stationary- and Synchronous-Reference Frames for Three-Phase Three-Wire Grid-Connected Converter AC Current Regulators. **Energies**, v. 14, n. 24, 2021. ISSN 1996-1073. DOI: 10.3390/en14248348. Available from: <https://www.mdpi.com/1996-1073/14/24/8348>. Cit. on pp. 40, 42.

COTA, Anna Paula Leite. **Desenvolvimento de Ferramentas Computacionais para a Análise de Perdas em Conversores Estáticos: Aplicação ao Cálculo de Rendimento de UPS's Trifásicas de Dupla Conversão**. 2016. PhD thesis – Universidade Federal de Minas Gerais. Cit. on pp. 94, 98, 100, 105, 142.

DAS, J. C. Passive filters - potentialities and limitations. **IEEE Transactions on Industry Applications**, v. 40, n. 1, p. 232–241, 2004. Cit. on p. 25.

DASGUPTA, Souvik et al. Application of Four-Switch-Based Three-Phase Grid-Connected Inverter to Connect Renewable Energy Source to a Generalized Unbalanced Microgrid System. **IEEE Transactions on Industrial Electronics**, v. 60, n. 3, p. 1204–1215, 2013. DOI: 10.1109/TIE.2012.2202350. Cit. on p. 35.

DASH, Ritesh; SWAIN, Sarat Chandra. Effective Power quality improvement using Dynamic Activate compensation system with Renewable grid interfaced sources. **Ain Shams Engineering Journal**, v. 9, n. 4, p. 2897–2905, 2018. ISSN 2090-4479. DOI: https://doi.org/10.1016/j.asej.2017.09.007. Cit. on pp. 35, 39.

DE ANDRADE, Eduardo G. et al. Power losses in photovoltaic inverter components due to reactive power injection. In: 2016 12th IEEE International Conference on Industry Applications (INDUSCON). [S.l.: s.n.], 2016. P. 1–7. DOI: 10.1109/INDUSCON.2016.7874587. Cit. on p. 105.

DE BARROS, R.C. et al. Lifetime evaluation of a multifunctional PV single-phase inverter during harmonic current compensation. **Microelectronics Reliability**, v. 88-90, p. 1071–1076, 2018. 29th European Symposium on Reliability of Electron Devices, Failure Physics and Analysis (ESREF 2018). ISSN 0026-2714. DOI: https://doi.org/10.1016/j.microrel.2018.07.009. Cit. on pp. 29, 52, 93, 105.

DE JESUS, V. M. R. et al. Comparison of MPPT Strategies in Three-Phase Photovoltaic Inverters Applied for Harmonic Compensation. **IEEE Transactions on Industry Applications**, v. 55, n. 5, p. 5141–5152, Sept. 2019. DOI: 10.1109/TIA.2019.2927924. Cit. on pp. 28, 59, 96.

_____. Operation Limits of Grid-Tied Photovoltaic Inverters With Harmonic Current Compensation Based on Capability Curves. **IEEE Transactions on Energy Conversion**, v. 36, n. 3, p. 2088–2098, 2021. DOI: 10.1109/TEC.2021.3050312. Cit. on p. 28.

DIVYA, K.; RAJ, T. Gowtham; MANIRAJ, P. Reduction of harmonics in distributed generation system using L-Z source inverter. In: 2017 IEEE International Conference on Electrical, Instrumentation and Communication Engineering (ICEICE). [S.l.: s.n.], 2017. P. 1–5. DOI: 10.1109/ICEICE.2017.8191865. Cit. on p. 36.

DOWELL, P. L. Effects of eddy currents in transformer windings. In.

DROFENIK, Uwe; KOLAR, Johann W. Analyzing the Theoretical Limits of Forced Air-Cooling by Employing Advanced Composite Materials with Thermal Conductivities gt; 400W/mK. In: 4TH International Conference on Integrated Power Systems. [S.l.: s.n.], 2006. P. 1–6. Cit. on pp. 93, 105.

DROFENIK, Uwe; LAIMER, Gerold; KOLAR, Johann. Theoretical converter power density limits for forced convection cooling, Jan. 2005. Cit. on p. 105.

ESPI, José M. et al. An Adaptive Robust Predictive Current Control for Three-Phase Grid-Connected Inverters. **IEEE Transactions on Industrial Electronics**, v. 58, n. 8, p. 3537–3546, 2011. DOI: 10.1109/TIE.2010.2089945. Cit. on p. 39.

FERREIRA, J. Analytical computation of AC resistance of round and rectangular litz wire windings. In. Cit. on pp. 101, 102, 145.

FLORESCU, A. et al. The advantages, limitations and disadvantages of Z-source inverter. In: CAS 2010 Proceedings (International Semiconductor Conference). [S.l.: s.n.], 2010. v. 02, p. 483–486. DOI: 10.1109/SMICND.2010.5650503. Cit. on p. 37.

FUJITA, Hideaki. Core-loss analysis in ac inductors for a single-phase pulse-width modulated solar power conditioner. In: 2011 IEEE Energy Conversion Congress and Exposition. [S.l.: s.n.], 2011. P. 2050–2057. DOI: 10.1109/ECCE.2011.6064039. Cit. on p. 101.

GAJANAYAKE, C. J.; VILATHGAMUWA, D. M.; LOH, P. C.; BLAABJERG, F., et al. A Z-source Inverter Based Flexible DG System with P+resonance and Repetitive Controllers for Power Quality Improvement of a Weak Grid. In: 2007 IEEE Power Electronics Specialists Conference. [S.l.: s.n.], 2007. P. 2457–2463. DOI: 10.1109/PESC.2007.4342398. Cit. on p. 38.

GAJANAYAKE, C. J.; VILATHGAMUWA, D. M.; LOH, P. C.; TEODORESCU, R., et al. Z-Source-Inverter-Based Flexible Distributed Generation System Solution for Grid Power Quality Improvement. **IEEE Transactions on Energy Conversion**, v. 24, n. 3, p. 695–704, Sept. 2009. DOI: 10.1109/TEC.2009.2025318. Cit. on p. 38.

GENG, Yiwen et al. An Overlap-Time Compensation Method for Current-Source Space-Vector PWM Inverters. **IEEE Transactions on Power Electronics**, v. 33, n. 4, p. 3192–3203, 2018. DOI: 10.1109/TPEL.2017.2707299. Cit. on p. 37.

GEURY, T.; PINTO, S.; GYSELINCK, J. Current source inverter-based photovoltaic system with enhanced active filtering functionalities. **IET Power Electronics**, v. 8, n. 12, p. 2483–2491, 2015. DOI: 10.1049/iet-pel.2014.0814. Cit. on p. 37.

GOMES, Camilo C.; CUPERTINO, Allan F.; PEREIRA, Heverton A. Damping techniques for grid-connected voltage source converters based on LCL filter: An overview. **Renewable and Sustainable Energy Reviews**, v. 81, p. 116–135, 2018. ISSN 1364-0321. DOI: https://doi.org/10.1016/j.rser.2017.07.050. Cit. on pp. 45, 46, 51, 55.

GONZALEZ, Damian A.; MCCALL, John C. Design of Filters to Reduce Harmonic Distortion in Industrial Power Systems. **IEEE Transactions on Industry Applications**, IA-23, n. 3, p. 504–511, 1987. DOI: 10.1109/TIA.1987.4504938. Cit. on p. 25.

HAMROUNI, Nejib; YOUNSI, Sami; JRAIDI, Moncef. A Flexible Active and Reactive Power Control Strategy of a LV Grid Connected PV System. **Energy Procedia**, v. 162, p. 325–338, 2019. Emerging and Renewable Energy: Generation and Automation. ISSN 1876-6102. DOI: https://doi.org/10.1016/j.egypro.2019.04.034. Cit. on p. 39.

HANIF, M.; BASU, M.; GAUGHAN, K. Understanding the operation of a Z-source inverter for photovoltaic application with a design example. **IET Power Electronics**, v. 4, n. 3, p. 278–287, Mar. 2011. DOI: 10.1049/iet-pel.2009.0176. Cit. on p. 37.

HUI, S.Y.R.; ZHU, J. Magnetic hysteresis modeling and simulation using the Preisach theory and TLM technique. In: PROCEEDINGS of 1994 Power Electronics Specialist Conference - PESC'94. [S.l.: s.n.], 1994. v. 2, 837–842 vol.2. DOI: 10.1109/PESC.1994.373776. Cit. on p. 102.

IEC. **IEC Standard 61000: Electromagnetic compatibility (EMC) - Part 3-2: Limits - Limits for harmonic current emissions**. [S.l.], 2014. P. 1–29. DOI: 10.1109/IEEESTD.2014.6826459. Cit. on p. 24.

IEEE. **IEEE Recommended Practice and Requirements for Harmonic Control in Electric Power Systems: IEEE Std 519-2014 (Revision of IEEE Std 519-1992)**. [S.l.], 2014. P. 1–29. DOI: 10.1109/IEEESTD.2014.6826459. Cit. on pp. 23–25.

_____. **IEEE Std 1531-2020: IEEE Guide for the Application and Specification of Harmonic Filters - Redline**. [S.l.], 2021. P. 1–127. Cit. on p. 25.

INFINEON. **Infineon IGBT modules**. [S.l.: s.n.], 2020. Available from: <https://www.infineon.com/cms/en/product/power/igbt/igbt-modules/fs15r12vt3/>. Visited on: 1 Feb. 2021. Cit. on pp. 51, 99, 105, 106.

JALILI, Kamran; BERNET, Steffen. Design of LCL Filters of Active-Front-End Two-Level Voltage-Source Converters. **IEEE Transactions on Industrial Electronics**, v. 56, n. 5, p. 1674–1689, 2009. DOI: 10.1109/TIE.2008.2011251. Cit. on p. 140.

JANPONG, Sarawut; AREERAK, Kongpol; AREERAK, Kongpan. Harmonic Detection for Shunt Active Power Filter Using ADALINE Neural Network. **Energies**, v. 14, n. 14, 2021. ISSN 1996-1073. DOI: 10.3390/en14144351. Cit. on pp. 42, 44.

JILES, D.C.; ATHERTON, D.L. Theory of ferromagnetic hysteresis. **Journal of Magnetism and Magnetic Materials**, v. 61, n. 1, p. 48–60, 1986. ISSN 0304-8853. DOI: https://doi.org/10.1016/0304-8853(86)90066-1. Cit. on p. 102.

K., Raggl et al. Comprehensive Design and Optimization of a High-Power-Density Single-Phase Boost PFC. **IEEE Transactions on Industrial Electronics**, v. 56, n. 7, p. 2574–2587, 2009. DOI: 10.1109/TIE.2009.2020074. Cit. on p. 93.

KAPELLER, H.; PLABNEGGER, B.; GRAGGER, J. V. Iron-Loss Modeling Based on a Loss-Separation Approach in Modelica. **IEEE Transactions on Magnetics**, v. 54, n. 3, p. 1–4, 2018. DOI: 10.1109/TMAG.2017.2758961. Cit. on p. 102.

KAZMIERKOWSKI, M.P.; MALESANI, L. Current control techniques for three-phase voltage-source PWM converters: a survey. **IEEE Transactions on Industrial Electronics**, v. 45, n. 5, p. 691–703, 1998. DOI: 10.1109/41.720325. Cit. on p. 38.

KIM, Sun-Pil et al. Imbalance Compensation of the Grid Current Using Effective and Reactive Power for Split DC-Link Capacitor 3-Leg Inverter. **IEEE Access**, v. 9, p. 81189–81201, 2021. DOI: 10.1109/ACCESS.2021.3085585. Cit. on p. 35.

KJAER, S.B.; PEDERSEN, J.K.; BLAABJERG, F. A review of single-phase grid-connected inverters for photovoltaic modules. **IEEE Transactions on Industry Applications**, v. 41, n. 5, p. 1292–1306, 2005. DOI: 10.1109/TIA.2005.853371. Cit. on p. 32.

KOLANTLA, Dharani et al. Critical review on various inverter topologies for PV system architectures. **IET Renewable Power Generation**, v. 14, Oct. 2020. DOI: 10.1049/iet-rpg.2020.0317. Cit. on p. 32.

KOLAR, J. W.; BIELA, J.; MINIBOCK, J. Exploring the pareto front of multi-objective single-phase PFC rectifier design optimization - 99.2% efficiency vs. 7kW/din³ power density. In: 2009 IEEE 6th International Power Electronics and Motion Control Conference. [S.l.: s.n.], 2009. P. 1–21. DOI: 10.1109/IPEMC.2009.5289336. Cit. on pp. 93, 97, 100, 104.

KOLAR, J. W.; BIELA, J.; WAFFLER, S., et al. Performance trends and limitations of power electronic systems. In: 2010 6th International Conference on Integrated Power Electronics Systems. [S.l.: s.n.], 2010. P. 1–20.

KOUCHAKI, Alireza; NYMAND, Morten. Analytical Design of Passive LCL Filter for Three-Phase Two-Level Power Factor Correction Rectifiers. **IEEE Transactions on Power Electronics**, v. 33, n. 4, p. 3012–3022, 2018. DOI: 10.1109/TPEL.2017.2705288. Cit. on p. 65.

KOUTROULIS, E.; BLAABJERG, F. Design optimization of grid-connected PV inverters. In: 2011 Twenty-Sixth Annual IEEE Applied Power Electronics Conference and Exposition (APEC). [S.l.: s.n.], 2011. P. 691–698. DOI: 10.1109/APEC.2011.5744671. Cit. on p. 93.

KUNZI, R. Thermal Design of Power Electronic Circuits. **CAS - CERN Accelerator School: Power Converters**, p. 311–327, July 2016. DOI: 10.5170/CERN-2015-003.311. Cit. on p. 98.

LE LESLE, J. et al. Multi-objective optimisation of a bidirectional single-phase grid connected AC/DC converter (PFC) with two different modulation principles. In: 2017 IEEE Energy Conversion Congress and Exposition (ECCE). [S.l.: s.n.], 2017. P. 5298–5305. DOI: 10.1109/ECCE.2017.8096889. Cit. on p. 93.

LI, Fei et al. A control strategy for multi-functional converter to improve grid power quality. In: IECON 2011 - 37th Annual Conference of the IEEE Industrial Electronics Society. [S.l.: s.n.], Nov. 2011. P. 790–795. DOI: 10.1109/IECON.2011.6119411. Cit. on p. 40.

LI, Jieli; ABDALLAH, T.; SULLIVAN, C.R. Improved calculation of core loss with nonsinusoidal waveforms. In: CONFERENCE Record of the 2001 IEEE Industry Applications Conference. 36th IAS Annual Meeting (Cat. No.01CH37248). [S.l.: s.n.], 2001. v. 4, 2203–2210 vol.4. DOI: 10.1109/IAS.2001.955931. Cit. on p. 102.

LI, X.; WANG, Y.; XU, W. A New Filtering Scheme for HVDC Terminals Based on Damped High-Pass Filter. **IEEE Transactions on Power Delivery**, v. 34, n. 5, p. 2050–2057, 2019. DOI: 10.1109/TPWRD.2019.2895084. Cit. on p. 25.

LI, Xiangshun et al. Modified Synchronous Reference Frame Method for Active Power Filter under Asymmetric and Distorted Supply Voltages Condition. In: 2015 International Conference on Industrial Informatics - Computing Technology, Intelligent Technology, Industrial Information Integration. [S.l.: s.n.], 2015. P. 1–5. DOI: 10.1109/ICIICII.2015.88. Cit. on p. 42.

LISERRE, M.; BLAABJERG, F.; HANSEN, S. Design and control of an LCL-filter based three-phase active rectifier. In: CONFERENCE Record of the 2001 IEEE Industry Applications Conference. 36th IAS Annual Meeting (Cat. No.01CH37248). [S.l.: s.n.], 2001. v. 1, 299–307 vol.1. DOI: 10.1109/IAS.2001.955428. Cit. on pp. 55, 67.

LISERRE, M.; BLAABJERG, F.; HANSEN, S. Design and control of an LCL-filter-based three-phase active rectifier. **IEEE Transactions on Industry Applications**, v. 41, n. 5, p. 1281–1291, 2005. DOI: 10.1109/TIA.2005.853373. Cit. on p. 80.

LISERRE, M.; TEODORESCU, R.; BLAABJERG, F. Stability of photovoltaic and wind turbine grid-connected inverters for a large set of grid impedance values. **IEEE Transactions on Power Electronics**, v. 21, n. 1, p. 263–272, 2006. Cit. on p. 51.

LISERRE, Marco; BLAABJERG, Frede; DELL AQUILA, Antonio. Step-by-step design procedure for a grid-connected three-phase PWM voltage source converter. **International Journal of Electronics**, Taylor and Francis, v. 91, n. 8, p. 445–460, 2004. DOI: 10.1080/00207210412331306186. Cit. on pp. 64, 65.

LIU, Pengcheng; WANG, Zheng, et al. Improved Harmonic Profile for High-Power PWM Current-Source Converters With Modified Space-Vector Modulation Schemes. **IEEE Transactions on Power Electronics**, v. 36, n. 10, p. 11234–11244, 2021. DOI: 10.1109/TPEL.2021.3070885. Cit. on p. 36.

LIU, Qing; CALDOGNETTO, Tommaso; BUSO, Simone. Review and Comparison of Grid-Tied Inverter Controllers in Microgrids. **IEEE Transactions on Power Electronics**, v. 35, n. 7, p. 7624–7639, 2020. DOI: 10.1109/TPEL.2019.2957975. Cit. on p. 38.

LUMBRERAS, D. et al. Trends in Power Quality, Harmonic Mitigation and Standards for Light and Heavy Industries: A Review. **Energies**, v. 13, p. 5792, Nov. 2020. DOI: 10.3390/en13215792. Cit. on p. 23.

LV, Qin et al. A Review of Research on Power System Harmonic Detection and Its Suppression Methods. In: 2020 IEEE 4th Information Technology, Networking, Electronic and Automation Control Conference (ITNEC). [S.l.: s.n.], 2020. v. 1, p. 1495–1500. DOI: 10.1109/ITNEC48623.2020.9084832. Cit. on p. 44.

MA, Y.; ELLINGER, T.; PETZOLDT, J. Implementation of harmonic control for a 3-phase 4-wire inverter with harmonic-loaded neutral. In: PROCEEDINGS of the 2011 14th European Conference on Power Electronics and Applications. [S.l.: s.n.], Aug. 2011. P. 1–10. Cit. on p. 33.

MAGNETICS. **Magnetics Power Core Catalog**. [S.l.: s.n.], 2020. Visited on: 20 Apr. 2020. Cit. on pp. 94, 101, 103, 104, 107.

MASTROMAURO, Rosa A.; LISERRE, Marco; DELL'AQUILA, Antonio. Study of the Effects of Inductor Nonlinear Behavior on the Performance of Current Controllers for Single-Phase PV Grid Converters. **IEEE Transactions on Industrial Electronics**, v. 55, n. 5, p. 2043–2052, 2008. DOI: 10.1109/TIE.2008.917117. Cit. on pp. 74–76, 80.

MATSUMORI, Hiroaki et al. Evaluation of Iron Loss of AC Filter Inductor Used in Three-Phase PWM Inverters Based on an Iron Loss Analyzer. **IEEE Transactions on Power Electronics**, v. 31, n. 4, p. 3080–3095, 2016. DOI: 10.1109/TPEL.2015.2453055. Cit. on pp. 101, 103.

MISHRA, Manash Kumar; LAL, Vivek Nandan. A Multiobjective Control Strategy for Harmonic Current Mitigation With Enhanced LVRT Operation of a Grid-Tied PV System Without PLL Under Abnormal Grid Conditions. **IEEE Journal of Emerging and Selected Topics in Power Electronics**, v. 11, n. 2, p. 2164–2177, 2023. DOI: 10.1109/JESTPE.2022.3218888. Cit. on pp. 28, 39.

MITSUBISHI ELECTRIC. **IGBT modules application note**. [S.l.: s.n.], 2020. Available from: <https://www.mitsubishielectric.com/semiconductors/files/manuals/igbt_t_t1_note_e.pdf>. Visited on: 1 June 2021. Cit. on p. 98.

MIVEH, Mohammad Reza et al. Control techniques for three-phase four-leg voltage source inverters in autonomous microgrids: A review. **Renewable and Sustainable Energy Reviews**, v. 54, p. 1592–1610, 2016. ISSN 1364-0321. DOI: https://doi.org/10.1016/j.rser.2015.10.079. Available from: <https://www.sciencedirect.com/science/article/pii/S1364032115011582>. Cit. on p. 39.

MOHAMMADI, Fazel et al. Robust Control Strategies for Microgrids: A Review. **IEEE Systems Journal**, v. 16, n. 2, p. 2401–2412, 2022. DOI: 10.1109/JSYST.2021.3077213. Cit. on p. 39.

MORENO, Vctor M. et al. A Comparative Analysis of Real-Time Algorithms for Power Signal Decomposition in Multiple Synchronous Reference Frames. **IEEE Transactions on Power Electronics**, v. 22, n. 4, p. 1280–1289, 2007. DOI: 10.1109/TPEL.2007.900484.

MORTEZAEI, A. et al. Multifunctional control strategy for asymmetrical cascaded H-Bridge Inverter in microgrid applications. In: 2015 IEEE Industry Applications Society Annual Meeting. [S.l.: s.n.], Oct. 2015. P. 1–8. DOI: 10.1109/IAS.2015.7356820. Cit. on pp. 34, 44.

MOUSAVI, S. Y. M. et al. Coordinated control of multifunctional inverters for voltage support and harmonic compensation in a grid-connected microgrid. **Electric Power Systems Research**, v. 155, p. 254–264, 2018. ISSN 0378-7796. DOI: https://doi.org/10.1016/j.epsr.2017.10.016. Cit. on pp. 35, 40.

MUNIR, S.; LI, Y. W. Residential Distribution System Harmonic Compensation Using PV Interfacing Inverter. **IEEE Trans. on Smart Grid**, v. 4, n. 2, p. 816–827, June 2013. ISSN 1949-3053. DOI: 10.1109/TSG.2013.2238262. Cit. on p. 27.

NADERI, Yahya et al. An optimized direct control method applied to multilevel inverter for microgrid power quality enhancement. **International Journal of Electrical Power and Energy Systems**, v. 107, p. 496–506, 2019. ISSN 0142-0615. DOI: https://doi.org/10.1016/j.ijepes.2018.12.007. Cit. on p. 38.

NEMA, Savita; NEMA, Rajesh; AGNIHOTRI, Gayatri. Inverter topologies and control structure in photovoltaic applications: A review. **Journal of Renewable and Sustainable Energy**, v. 3, Jan. 2011. DOI: 10.1063/1.3505096. Cit. on p. 32.

NGUYEN, Tuyen; LEE, Hong-Hee; NGUYEN, Hoang. Adaptive Carrier-based PWM for a Four-Switch Three-Phase Inverter under DC-link Voltage Ripple Conditions. **Journal of Electrical Engineering and Technology**, v. 5, June 2010. DOI: 10.5370/JEET.2010.5.2.290. Cit. on p. 35.

NOVAK, Mateja; SANGWONGWANICH, Ariya; BLAABJERG, F. Monte Carlo-Based Reliability Estimation Methods for Power Devices in Power Electronics Systems. **IEEE Open Journal of Power Electronics**, PP, p. 1–1, Sept. 2021. DOI: 10.1109/OJPEL.2021.3116070. Cit. on p. 51.

PADUNGSIN, Maneerat; NARONGRIT, Tosaporn; AREERAK, Kongpol. The Comparison Study of Harmonic Detection Algorithms for Single-Phase Power Systems. In: 2018 5th International Conference on Electric Power and Energy Conversion Systems (EPECS). [S.l.: s.n.], 2018. P. 1–6. DOI: 10.1109/EPECS.2018.8443548.

PAUKNER, F. L. et al. Inductive filter design for three-phase grid connected power converters. In: 2015 IEEE 13th Brazilian Power Electronics Conference and 1st Southern Power Electronics Conference (COBEP/SPEC). [S.l.: s.n.], 2015. P. 1–5. DOI: 10.1109/COBEP.2015.7420189. Cit. on pp. 45, 93.

PENA-ALZOLA, Rafael; LISERRE, Marco; BLAABJERG, Frede; ORDONEZ, Martin, et al. LCL-Filter Design for Robust Active Damping in Grid-Connected Converters. **IEEE Transactions on Industrial Informatics**, v. 10, n. 4, p. 2192–2203, 2014. DOI: 10.1109/TII.2014.2361604. Cit. on pp. 45, 46, 48, 51, 139.

PENA-ALZOLA, Rafael; LISERRE, Marco; BLAABJERG, Frede; SEBASTIAN, Rafael, et al. Analysis of the Passive Damping Losses in LCL-Filter-Based Grid Converters. **IEEE Transactions on Power Electronics**, v. 28, n. 6, p. 2642–2646, 2013. DOI: 10.1109/TPEL.2012.2222931. Cit. on pp. 46, 67, 94, 140.

PEREIRA, H. A. et al. Flexible harmonic current compensation strategy applied in single and three-phase photovoltaic inverters. **International Journal of Electrical Power and Energy Systems**, v. 104, p. 358–369, 2019. ISSN 0142-0615. DOI: https://doi.org/10.1016/j.ijepes.2018.07.017. Cit. on pp. 33, 34, 39, 40, 43.

PICARD, C.; SGRO, D.; GIOFFRE, G. A new active filtering technique for grid-connected inverters. In: INTERNATIONAL Symposium on Power Electronics Power Electronics, Electrical Drives, Automation and Motion. [S.l.: s.n.], 2012. P. 900–905. DOI: 10.1109/SPEEDAM.2012.6264553. Cit. on pp. 34, 36.

POPOVIC, Zoya B. **Introductory electromagnetics / Zoya Popovic, Branko D. Popovic.** Upper Saddle River, N.J: Prentice Hall, 2000. ISBN 0201326787. Cit. on p. 101.

RAY, Pragnyashree; RAY, Pravat Kumar; DASH, Santanu Kumar. Power Quality Enhancement and Power Flow Analysis of a PV Integrated UPQC System in a Distribution Network. **IEEE Transactions on Industry Applications**, v. 58, n. 1, p. 201–211, 2022. DOI: 10.1109/TIA.2021.3131404. Cit. on pp. 23, 25, 27.

REATTI, A.; KAZIMIERCZUK, M.K. Comparison of various methods for calculating the AC resistance of inductors. **IEEE Transactions on Magnetics**, v. 38, n. 3, p. 1512–1518, 2002. DOI: 10.1109/20.999124. Cit. on pp. 101, 146, 147.

REINERT, J.; BROCKMEYER, A.; DE DONCKER, R.W.A.A. Calculation of losses in ferro- and ferrimagnetic materials based on the modified Steinmetz equation. **IEEE Transactions on Industry Applications**, v. 37, n. 4, p. 1055–1061, 2001. DOI: 10.1109/28.936396. Cit. on p. 102.

SAEED, Nimrah; IBRAR, Anas; SAEED, Aimen. A Review on Industrial Applications of Z-Source Inverter. **Journal of Power and Energy Engineering**, v. 05, p. 14–31, Jan. 2017. DOI: 10.4236/jpee.2017.59002. Cit. on pp. 36, 37.

SAFA, Ahmed et al. A robust control algorithm for a multifunctional grid tied inverter to enhance the power quality of a microgrid under unbalanced conditions. **International Journal of Electrical Power and Energy Systems**, v. 100, p. 253–264, 2018. ISSN 0142-0615. DOI: https://doi.org/10.1016/j.ijepes.2018.02.042. Cit. on p. 38.

SALEM, W.A.A. et al. Grid connected photovoltaic system impression on power quality of low voltage distribution system. Ed. by James Lam. **Cogent Engineering**, Cogent OA, v. 9, n. 1, p. 2044576, 2022. DOI: 10.1080/23311916.2022.2044576. eprint: https://doi.org/10.1080/23311916.2022.2044576. Available from: <https://doi.org/10.1080/23311916.2022.2044576>. Cit. on p. 23.

SANTANA, Renato Atila Silva. **Projeto e Análise de Rendimento de um UPS Monofásica de Três Braços e Construção de um Calorímetro Fechado de Dupla Caixa**. 2018. PhD thesis – Universidade Federal de Minas Gerais. Cit. on pp. 98, 105.

SHAFIULLAH, Md; AHMED, Shakir D.; AL-SULAIMAN, Fahad A. Grid Integration Challenges and Solution Strategies for Solar PV Systems: A Review. **IEEE Access**, v. 10, p. 52233–52257, 2022. DOI: 10.1109/ACCESS.2022.3174555. Cit. on p. 27.

SHAH, P. et al. GI-Based Control Scheme for Single-Stage Grid Interfaced SECS for Power Quality Improvement. **IEEE Transactions on Industry Applications**, v. 55, n. 1, p. 869–881, Jan. 2019. DOI: 10.1109/TIA.2018.2866375. Cit. on p. 39.

SHIMIZU, T. et al. Loss evaluation of AC filter inductor core on a PWM converter. In: 8TH International Conference on Power Electronics - ECCE Asia. [S.l.: s.n.], 2011. P. 1047–1052. DOI: 10.1109/ICPE.2011.5944704. Cit. on p. 101.

SILVA JUNIOR, Dalmo C. et al. Control of a multi-functional inverter in an AC microgrid - Real-time simulation with control hardware in the loop. **Electric Power Systems Research**, v. 172, p. 201–212, 2019. ISSN 0378-7796. DOI: https://doi.org/10.1016/j.epsr.2019.03.016. Cit. on p. 28.

SILVEIRA BRITO, Erick Matheus da. **Lifetime Evaluation of Photovoltaic Inverters with Capability of Reactive Power Support**. 2021. PhD thesis – Universidade Federal de Minas Gerais, Belo Horizonte, Brasil. Available from: <https://www.ppgee.ufmg.br/defesas/1712D.PDF>. Cit. on p. 104.

SINGH, Bhim; CHANDRA, Ambrish; AL-HADDADL, Kamal. Shunt Active Power Filters. In: POWER Quality Problems and Mitagation Techniques. [S.l.: s.n.], 2015. P. 397–451. DOI: 10.1002/9781118922064.ch9. Cit. on p. 96.

SINGH, M.; CHANDRA, A. Application of Adaptive Network-Based Fuzzy Inference System for Sensorless Control of PMSG-Based Wind Turbine With Nonlinear-Load-Compensation Capabilities. **IEEE Transactions on Power Electronics**, v. 26, n. 1, p. 165–175, Jan. 2011. DOI: 10.1109/TPEL.2010.2054113. Cit. on p. 39.

SINGH, M.; KHADKIKAR, V., et al. Grid Interconnection of Renewable Energy Sources at the Distribution Level With Power-Quality Improvement Features. **IEEE Transactions on Power Delivery**, v. 26, n. 1, p. 307–315, Jan. 2011. DOI: 10.1109/TPWRD.2010.2081384. Cit. on p. 40.

SOARES, Leonardo Tameirao Ferreira. **Contribuicao ao Controle de um Conversor Reversivel Aplicado a um Aerogerador Sincrono a Imas Permanentes**. 2016. PhD thesis – Universidade Federal de Minas Gerais. Cit. on p. 142.

SOLATIALKARAN, Davood; KHAJEH, Kiarash Gharani; ZARE, Firuz. A Novel Filter Design Method for Grid-Tied Inverters. **IEEE Transactions on Power Electronics**, v. 36, n. 5, p. 5473–5485, 2021. DOI: 10.1109/TPEL.2020.3029827. Cit. on pp. 35, 44–46.

SOLOMON, O.M. The use of DFT windows in signal-to-noise ratio and harmonic distortion computations. **IEEE Transactions on Instrumentation and Measurement**, v. 43, n. 2, p. 194–199, 1994. DOI: 10.1109/19.293419. Cit. on p. 42.

SRINIVAS, V. L. et al. Partially Decoupled Adaptive Filter Based Multifunctional Three-Phase GPV System. **IEEE Transactions on Sustainable Energy**, v. 9, n. 1, p. 311–320, Jan. 2018. DOI: 10.1109/TSTE.2017.2731793. Cit. on pp. 39, 40.

STEINMETZ, Chas.P. On the law of hysteresis. **Proceedings of the IEEE**, v. 72, n. 2, p. 197–221, 1984. DOI: 10.1109/PROC.1984.12842. Cit. on p. 102.

SUJITJORN, S.; AREERAK, K.-L.; KULWORAWANICHPONG, T. The DQ Axis With Fourier (DQF) Method for Harmonic Identification. **IEEE Transactions on Power Delivery**, v. 22, n. 1, p. 737–739, 2007. DOI: 10.1109/TPWRD.2006.882465. Cit. on pp. 42–44.

SULLIVAN, Charlie. **Core Loss Calculator**. [S.l.: s.n.], 2006. Available from: <https://engineering.dartmouth.edu/inductor/coreloss.shtml>. Visited on: 1 Nov. 2020. Cit. on p. 103.

SUN, G. et al. Multi-functional grid-connected inverter with enhanced disturbance rejection capability. **The Journal of Engineering**, v. 2019, n. 17, p. 3587–3591, 2019. DOI: 10.1049/joe.2018.8147. Cit. on p. 39.

TAKEDA, M. et al. Harmonic current and reactive power compensation with an active filter. In: PESC '88 Record., 19th Annual IEEE Power Electronics Specialists Conference. [S.l.: s.n.], 1988. 1174–1179 vol.2. DOI: 10.1109/PESC.1988.18259. Cit. on p. 43.

TEKE, A.; LATRAN, M. Review of Multifunctional Inverter Topologies and Control Schemes Used in Distributed Generation Systems. **Journal of Power Electronics**, v. 14, p. 324–340, 2014. Cit. on pp. 32, 34, 35.

TENTI, Paolo; MATTAVELLI, Paolo; MORALES PAREDES, Helmo K. Conservative Power Theory, sequence components and accountability in smart grids. In: 2010 International School on Nonsinusoidal Currents and Compensation. [S.l.: s.n.], 2010. P. 37–45. DOI: 10.1109/ISNCC.2010.5524473. Cit. on pp. 42, 44.

TIMBUS, Adrian et al. Evaluation of Current Controllers for Distributed Power Generation Systems. **IEEE Transactions on Power Electronics**, v. 24, n. 3, p. 654–664, 2009. DOI: 10.1109/TPEL.2009.2012527. Cit. on p. 42.

TWINING, Erika; HOLMES, D.G. Grid current regulation of a three-phase voltage source inverter with an LCL input filter. **IEEE Transactions on Power Electronics**, v. 18, n. 3, p. 888–895, 2003. DOI: 10.1109/TPEL.2003.810838. Cit. on p. 46.

VENKATACHALAM, K. et al. Accurate prediction of ferrite core loss with nonsinusoidal waveforms using only Steinmetz parameters. In: 2002 IEEE Workshop on Computers in Power Electronics, 2002. Proceedings. [S.l.: s.n.], 2002. P. 36–41. DOI: 10.1109/CIPE.2002.1196712. Cit. on pp. 102, 103.

VILKN, Pedro Humberto Jacinto. **Desenvolvimento de Metodologia para Projeto de Indutores Utilizados em UPS de Alto Rendimento**. 2018. PhD thesis – Universidade Federal de Minas Gerais. Cit. on pp. 74, 75, 142.

VILLAR, I. et al. Global Loss Evaluation Methods for Nonsinusoidally Fed Medium-Frequency Power Transformers. **IEEE Transactions on Industrial Electronics**, v. 56, n. 10, p. 4132–4140, 2009. DOI: 10.1109/TIE.2009.2021174. Cit. on pp. 101, 102.

WANG, F.; DUARTE, J. L.; HENDRIX, M. A. M. Pliant Active and Reactive Power Control for Grid-Interactive Converters Under Unbalanced Voltage Dips. **IEEE Transactions on Power Electronics**, v. 26, n. 5, p. 1511–1521, May 2011. DOI: 10.1109/TPEL.2010.2052289. Cit. on p. 33.

WANG, Hengyi; LIU, Steven. Adaptive Kalman filter for harmonic detection in active power filter application. In: 2015 IEEE Electrical Power and Energy Conference (EPEC). [S.l.: s.n.], 2015. P. 227–232. DOI: 10.1109/EPEC.2015.7379954. Cit. on p. 42.

WATANABE, E. H.; AKAGI, H.; AREDES, M. Instantaneous p-q power Theory for compensating nonsinusoidal systems. In: 2008 International School on Nonsinusoidal Currents and Compensation. [S.l.: s.n.], June 2008. P. 1–10. DOI: 10.1109/ISNCC.2008.4627480. Cit. on pp. 42, 50.

WOJDA, Rafal P.; KAZIMIERCZUK, Marian K. Analytical Optimization of Solid-Round-Wire Windings. **IEEE Transactions on Industrial Electronics**, v. 60, n. 3, p. 1033–1041, 2013. DOI: 10.1109/TIE.2012.2189543. Cit. on p. 101.

WU, T. et al. PV Power Injection and Active Power Filtering With Amplitude-Clamping and Amplitude-Scaling Algorithms. **IEEE Transactions on Industry Applications**, v. 43, n. 3, p. 731–741, May 2007. DOI: 10.1109/TIA.2007.895764. Cit. on p. 34.

WU, Weimin et al. A Robust Passive Damping Method for LLCL-Filter-Based Grid-Tied Inverters to Minimize the Effect of Grid Harmonic Voltages. **IEEE Transactions on Power Electronics**, v. 29, n. 7, p. 3279–3289, 2014. DOI: 10.1109/TPEL.2013.2279191. Cit. on pp. 45, 46.

XAVIER, L. S.; CUPERTINO, A. F.; DE RESENDE, J. T., et al. Adaptive current control strategy for harmonic compensation in single-phase solar inverters. **Electric Power Systems Research**, v. 142, p. 84–95, 2017. ISSN 0378-7796. DOI: https://doi.org/10.1016/j.epsr.2016.08.040. Cit. on p. 38.

XAVIER, L. S.; CUPERTINO, A. F.; PEREIRA, H. A., et al. Partial Harmonic Current Compensation for Multifunctional Photovoltaic Inverters. **IEEE Transactions on Power Electronics**, v. 34, n. 12, p. 11868–11879, 2019. DOI: 10.1109/TPEL.2019.2909394. Cit. on p. 28.

YANG, W. Y. et al. **Applied Numerical Methods using MATLAB, 1st ed.** [S.l.]: Wiley-Inter-science, 2005. Cit. on p. 55.

YAZDANI, Amirnaser; IRAVANI, Reza. Grid-Imposed Frequency VSC System: Control in -Frame. In: VOLTAGE-SOURCED Converters in Power Systems: Modeling, Control, and Applications. [S.l.: s.n.], 2010. P. 160–203. DOI: 10.1002/9780470551578.ch7. Cit. on p. 48.

YAZDANI, Davood; BAKHSHAI, Alireza, et al. A Real-Time Three-Phase Selective-Harmonic-Extraction Approach for Grid-Connected Converters. **IEEE Transactions on Industrial Electronics**, v. 56, n. 10, p. 4097–4106, 2009. DOI: 10.1109/TIE.2009.2024658. Cit. on p. 42.

YEPES, Alejandro G. et al. Analysis and Design of Resonant Current Controllers for Voltage-Source Converters by Means of Nyquist Diagrams and Sensitivity Function. **IEEE Transactions on Industrial Electronics**, v. 58, n. 11, p. 5231–5250, 2011. DOI: 10.1109/TIE.2011.2126535. Cit. on pp. 40, 49, 50, 78, 81.

YUNTING, Liu et al. Aging Effect Analysis of PV Inverter Semiconductors for Ancillary Services Support. **IEEE Open Journal of Industry Applications**, v. 1, p. 157–170, 2020. DOI: 10.1109/OJIA.2020.3028647. Cit. on p. 29.

ZAREI, Seyed Fariborz; MOKHTARI, Hossein; BLAABJERG, Frede. Fault Detection and Protection Strategy for Islanded Inverter-Based Microgrids. **IEEE Journal of Emerging and Selected Topics in Power Electronics**, v. 9, n. 1, p. 472–484, 2021. DOI: 10.1109/JESTPE.2019.2962245. Cit. on p. 79.

ZEB, Kamran et al. A comprehensive review on inverter topologies and control strategies for grid connected photovoltaic system. **Renewable and Sustainable Energy Reviews**, v. 94, p. 1120–1141, 2018. ISSN 1364-0321. DOI: https://doi.org/10.1016/j.rser.2018.06.053. Cit. on pp. 39, 40.

ZENG, Z.; LI, X.; SHAO, W. Multi-functional grid-connected inverter: upgrading distributed generator with ancillary services. **IET Renewable Power Generation**, v. 12, n. 7, p. 797–805, 2018. DOI: 10.1049/iet-rpg.2017.0609. Cit. on p. 28.

ZHANG, Chi et al. Resonance damping techniques for grid-connected voltage source converters with LCL filters - A review. In: 2014 IEEE International Energy Conference (ENERGYCON). [S.l.: s.n.], 2014. P. 169–176. DOI: 10.1109/ENERGYCON.2014.6850424. Cit. on p. 46.

ZHOU, Zhongfu; HOLLAND, P.M.; IGIC, Petar. Compact thermal model of a three-phase IGBT inverter power module. In: p. 167–170. ISBN 978-1-4244-1881-7. DOI: 10.1109/ICMEL.2008.4559249. Cit. on p. 98.

Appendix

APPENDIX A – Implemented Inductor Model Parameters

This appendix provides the essential information required for the implementation of the nonlinear model of the inductor, which was implemented in Chapter 4.

Table 13 – Chapter 4 implemented inductor characteristics.

a	0.0382812795454997
b	0.0179973286225475
c	0.000701216650615925
d	0.0706331225497646
e	0.000450176707480978
x	1.630
Path Length	243 mm
Number of Turns	129
Area	358 mm²
dc Resistance	37.7 mΩ

Throughout the curve fitting equation give in Eq. A.1 and the parameters presented in Table 15, it is possible to determine the flux density (B) versus magnetic field strength (H) to assemble the required lookup table:

$$B = \left(\frac{a + bH + cH^2}{1 + dH + eH^2}\right)^x. \tag{A.1}$$

APPENDIX B – LCL Filter Design for Normal Operation

This LCL filter design strategy is carried as proposed in (PENA-ALZOLA; LISERRE; BLAABJERG; ORDONEZ, et al., 2014).

The total inductance per unit can be calculated as:

$$l_T = r_f \frac{f_n}{f_s} \frac{1 + r_l}{\sqrt{r_l r_q}}, \tag{B.1}$$

where r_q is the ratio between the LCL filter inductance and capacitance ($r_q = C_f/l_T$), r_l is the ratio between the grid and converter inductance ($r_l = L_f/L_g$) and $r_f = f_{sw}/f_{res}$ is the ratio between the switching frequency f_s and the resonance frequency f_{res}.

Current total harmonic distortion (THD_i) can be estimated to assess the LCL filter attenuation and is given by:

$$\tilde{i}_g^{up} = \frac{\pi V_{dc}}{12 Z_b} \frac{\sqrt{r_q}}{r_f^3} \frac{\sqrt{r_l}}{(1 + r_l)} \frac{1}{(1 - 6/m_f)^2 - 1/r_f^2} \sqrt{(f_m)}, \tag{B.2}$$

f_m is given by:

$$f(m) = \frac{3}{2} m^2 - \frac{4\sqrt{3}}{\pi} m^3 + \frac{9}{8} \left(\frac{3}{2} - \frac{9}{8} \frac{\sqrt{3}}{\pi} m^4\right), \tag{B.3}$$

and m is the fundamental component modulation index,

$$m = \frac{2\sqrt{2}}{V_{dc}} \sqrt{\left(\frac{V_n}{\sqrt{3}}\right)^2 + (2\pi f_n L_T I_n)^2}. \tag{B.4}$$

Finally, THD_i can be estimated as:

$$THD = \frac{\tilde{i}_g^{up}}{I_m} * 100 \tag{B.5}$$

When designing an LCL filter, some parameters limit must be introduced in order to achieve better performance:

- the capacitor value is limited by the maximum reactive power circulating in the system (generally should be less than 5%);
- the total harmonic current distortion (THD) must be smaller than 5%;
- the total inductance value must be limited in order to reduce the drop voltage during operation;
- the resonant frequency must be within a range that does not influence the lowest and highest frequencies, i.e., above ten times the grid frequency and below half the switching frequency. ($10f < f_{res} < 0.5f_s$)

The first guideline for limiting filter parameters is the total reactive power. In this project, a minimum allowable power factor of 0.5% was adopted. Thus, $FP_{min} = 0.995$. Following, the second guideline concerns THD. A 3% THD was used, since the models used in the simulation neglect some aspects such as key dead time and grid distortion.

The filters total inductance must satisfy three restrictions to respect the voltage drop limits and the voltage oscillation:

- the inductance must be smaller than 0.1 pu;
- the inductance must be smaller than a purely inductive filter;
- Minimum inductance to limit the first inductor current ripple between 30% and 50%.

The restrictions presented are translated into the following equations:

$$L_{max,\delta_V} = \frac{L_b}{10}, \tag{B.6}$$

where L_b is the system base inductance.

Also, the total filter inductance should be smaller than purely inductive filter. Thus, it was considered the L filter design proposed by Pena-Alzola, Liserre, Blaabjerg, Sebastian, et al. (2013) given by:

$$L_{max,L} = \frac{100}{6\sqrt{3}} \frac{1}{\sqrt{48}} \frac{V_{dc}}{f_s I_n} \sqrt{f(m)}. \tag{B.7}$$

Additionally, minimum inductance to limit the inverter-side inductor current ripple between 30% and 50% should be provided. To satisfy this requirement authors in Jalili and Bernet (2009) proposed the following approach:

$$L_{f,min} = \frac{V_g/\sqrt{3}}{2\sqrt{6}f_s\delta_{if}}, \tag{B.8}$$

δ_{if} is the current ripple in Ampere.

APPENDIX C – Inductor Design

C.1 Design overview

Among the available cores, select all those that meet the maximum energy criterion given by:

$$E_{max} = \frac{LI_{max}^2}{2}. \tag{C.1}$$

A total of 206 different core are available to select, with the maximum energy varying from 0.0001 to 5600 J. All inductors that meet the minimum energy criteria are analyzed. Afterwards, if no core is selected, meaning the maximum energy criterion was not satisfied, a series inductor is added and the algorithm returns to eq. C.1.

The design methodology of the inductors is based on the work carried out in Soares (2016), Cota (2016) and Vilkn (2018). Given the core selection all material data are also obtained from information loaded from data sheet. Throughout the curve fitting equation give in Eq. C.2 it is possible to determine the flux density (B):

$$B = (\frac{a + bH + cH^2}{1 + dH + eH^2})^x. \tag{C.2}$$

To determine the turn number (N) the approach is based on the $B \times N$ curve, where the solution is the following equations curve intersection:

$$N = \frac{LI_{max}}{B_{max}A_e} \tag{C.3}$$

$$B \approx \frac{\mu NI}{l_e} \rightarrow N \approx \frac{B_{max}l_e}{\mu I_{max}} \tag{C.4}$$

In eq. C.3, the maximum flux density (B_{max}) is assigned to the vector between 0 and 2 T and where A_e is the selected core area. Moreover, eq. C.3 is based on the magnetic field produced by a N turn coil using the Ampere law, where l_e is the core effective length. The permeability μ can be derived, for each magnetic field strength H, from the $B_{max} \times H$ characteristic. It is considered that the solution for B_{max} should not exceed 70% of the flux density leading to core saturation. If this criterion is not met, a series inductor is added and the algorithm returns to Eq. C.1.

The conductor diameter must be defined so that the skin effect can be neglected for current harmonics around the switching frequency. It is adopted that the conductor diameter must not exceed twice the cooper wire depth of penetration δ_p at this frequency. The depth of penetration is given by:

$$\delta_p = \sqrt{\frac{\rho}{\pi \mu_{cu} f_s}}. \tag{C.5}$$

Furthermore, the chosen conductor must comply with the maximum current density (j_{max}). Therefore, parallel conductors could be necessary. The number of parallel conductors can be determined as:

$$n_p = \frac{4 I_{max}}{\pi j_{max} d^2}. \tag{C.6}$$

Now it is possible to determine the conductors occupancy area and the the selected core fill factor. Fill factor is the ratio of total conductor cross section to the area of the core window. The conductors area is give by:

$$A_c = n_p N d. \tag{C.7}$$

Hence, the fill factor (FF) can be obtained as:

$$FF = A_c / A_n. \tag{C.8}$$

where A_h is the core area. According to the manufacturer toroidal core winding factors can vary from 20-60%, where typical value in many applications being 35-40%. In this work a fill factor of 40% is considered. If the design exceed this value the algorithm will return to the beginning and select a core with higher maximum energy. Although, if there is no other core to select a series inductor will be allocated.

C.2 Selected Inductors

The tables below present the construction parameters of the inductors selected by the optimization algorithm.

Table 14 – Chapter 5 selected inductors characteristics for normal and multifunctional operation.

Normal operation			
Core Part Number	78094	78110	114040
Material	XFlux Toroid	XFlux Toroid	Kook Mu E-cores
Inductance (mH)	0.31	0.54	0.7
Volume (mm³)	15600	20700	262000
Area (mm²)	134	144	1220
Path Length (mm)	116	143	215
Number of Turns	44	48	72
Number of Parallel Conductors	5	4	4
dc Resistance (mΩ)	9.54	8.78	7.97
k	542.7	542.7	34.20
α	1.194	1.194	1.541
β	2.015	2.015	1.988
Multifunctional operation			
Core Part Number	78094	58110	58195
Material	XFlux Toroid	High Flux Toroid	High Flux Toroid
Inductance (mH)	0.31	0.42	0.44
Volume (mm³)	15600	20700	28600
Area (mm²)	134	144	229
Path Length (mm)	116	143	125
Number of Turns	44	62	32
Number of Parallel Conductors	5	4	4
dc Resistance (mΩ)	9.54	14.01	8.01
k	542.7	246.5	181.1
α	1.194	1.311	1.378
β	2.015	2.218	2.218

APPENDIX D – AC Winding Resistance Calculation

The ac winding resistance calculation methodology is based on the techniques proposed in Bahmani, Thiringer, and Ortega (2014), Bartoli et al. (1995) and Ferreira (1992). This method is often referred as Ferreira's expression given as:

$$R_w = N_l R_{skin} + R_{prox}(N_l \frac{4N_l(N_l^2 - 1)}{3}), \tag{D.1}$$

where, N_l is the number of layers. R_{skin}, and R_{prox} are given by:

$$R_{skin} = R_{dcm} \frac{\gamma}{2} \frac{ber_2\gamma ber'\gamma + bei_2\gamma bei'\gamma}{ber^2\gamma + bei^2\gamma} \tag{D.2}$$

and

$$R_{prox} = -R_{dcm} \frac{\gamma}{2} 2\pi\eta^2 \frac{ber_2\gamma ber'\gamma + bei_2\gamma bei'\gamma}{ber^2\gamma + bei^2\gamma}. \tag{D.3}$$

The Kelvin functions ber and bei are the real and imaginary parts of Bessel functions of the first kind, respectively. R_{dcm} is the winding dc resistance in each layer. Also,

$$\gamma = \frac{d}{\delta\sqrt{2}} \tag{D.4}$$

and

$$\eta = \frac{d}{t}\sqrt{\frac{\pi}{4}} \tag{D.5}$$

where d is the round conductor wire diameter, t is the distance between two adjacent conductors and ρ is the skin depth defined as:

$$\delta = \sqrt{\frac{\rho_{cu}}{\pi f \mu_{cu}\mu_0}} \tag{D.6}$$

where ρ_{cu} is the copper resistivity, μ_{cu} is the copper relative magnetic permeability and μ_0 is the vacuum permeability.

Fig. 61 presents possible models for ac winding resistance. Where L is the nominal inductance, R_c is the magnetic core resistance, R_w and C are the inductor self-capacitance.

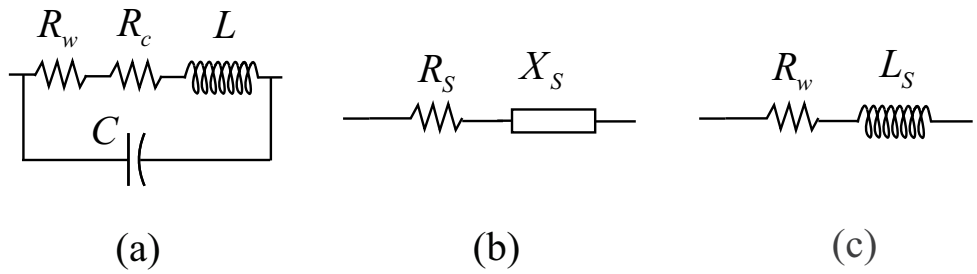

Figure 61 – Inductor winding model: (a) lumped circuit; (b) equivalent series circuit; and (c) equivalent series circuit when $R_c << R_w$ at low frequency.

Fig. 61 - (a) lumped circuit impedance is described as:

$$X_S = \frac{(R_w + R_c) + j\omega L(1 - \omega^2 LC - C(R_w + R_c)^2/L)}{(1 - \omega^2 LC)^2 + \omega^2 C^2 (R_w + R_c)^2}. \tag{D.7}$$

In Fig. 61 - (b) R_S and X_S are the real and imaginary parts of Eq. D.7. For powder cores, core resistance are much lower than winding resistances and may be neglected (REATTI; KAZIMIERCZUK, 2002; BARTOLI et al., 1995). Also, for frequencies much lower than the first self-resonant frequency (usually in MHz order), the equivalent series reactance has an inductive characteristic and can be expressed as an equivalent series inductance as depicted in 61 - (c). Fig. D.1 presents an ac winding inductor example. It is possible to note that it is extremely important to model high-frequency characteristics for the correct evaluation of power losses in inductors. Fig. 62 presents an ac winding resistance result example.

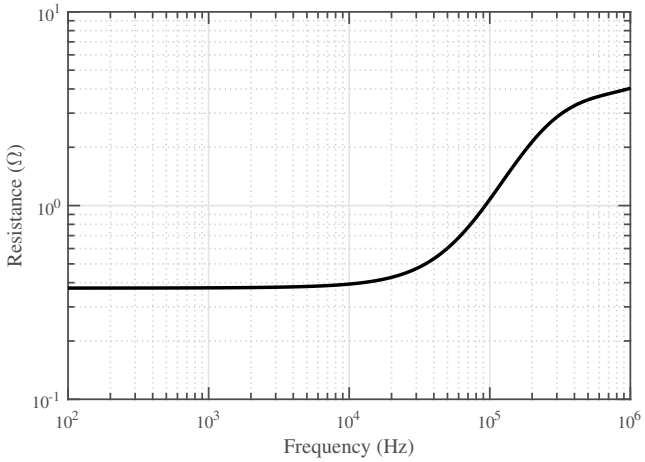

Figure 62 – ac resistance calculation example, extracted from (REATTI; KAZIMIERCZUK, 2002). With, $N_l = 2$, $R_{dc} = 0.4242$, $d = 0.45$, $t = 0.65$

APPENDIX E – Optimal Inductors characteristics

This appendix provides the essential information required for the implementation of the non-linear model of the inductor, which was implemented in Chapter 4.

Table 15 – Chapter 4 implemented inductor characteristics.

a	0.0382812795454997
b	0.0179973286225475
c	0.000701216650615925
d	0.0706331225497646
e	0.000450176707480978
x	1.630
Path Length	243 mm
Number of Turns	129
Area	358 mm²
dc Resistance	37.7 mΩ